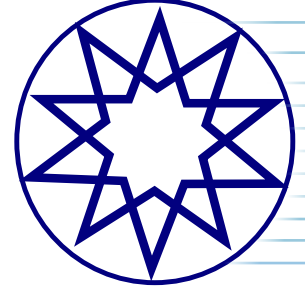


ISSN: 2792-0771

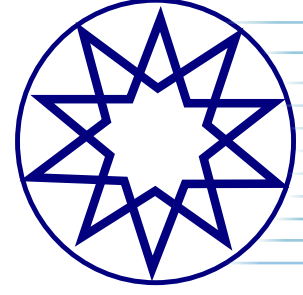


Seatific

Volume 3
Number 1
Year 2023

YTÜ
PRESS

seatific.yildiz.edu.tr



Chief Executive

Huseyin Yilmaz, Yildiz Technical University, İstanbul, Türkiye
hyilmaz@yildiz.edu.tr

Editor-in-Chief

Bahri Sahin, Yildiz Technical University, İstanbul, Türkiye
sahinb@yildiz.edu.tr

Co-Editors-in-Chief

Ahmet Dursun Alkan, Yildiz Technical University, İstanbul, Türkiye
alkanad@yildiz.edu.tr

Veysi Bashan, Bursa Technical University, Bursa, Türkiye
veysi.bashan@btu.edu.tr

Seyfettin Bayraktar, Yildiz Technical University, İstanbul, Türkiye
sbay@yildiz.edu.tr

Umit Gunes, Yildiz Technical University, İstanbul, Türkiye
ugunes@yildiz.edu.tr

Asım Sinan Karakurt, Yildiz Technical University, İstanbul, Türkiye
asinan@yildiz.edu.tr

Ibrahim Ozsari, Bursa Technical University, Bursa, Türkiye
ibrahim.ozsari@btu.edu.tr

Editorial Board

Maria Acanfora, University of Naples Federico II, Italy
maria.acanfora@unina.it

Abdulrahman Almerbati, King Fahd University of Petroleum and Minerals, Saudi Arabia
almerbati@kfupm.edu.sa

Flavio Balsamo, University of Naples Federico II, Italy
flbalsam@unina.it

Tanmay Basak, Indian Institute of Technology Madras India
tanmay@iitm.ac.in

Tunde Bello-Ochende, University of Cape Town, South Africa
tunde.bello-ochende@uct.ac.za

Adrian Bejan, Duke University, USA
abejan@duke.edu

Ali Cemal Benim, Fachschule Dusseldorf, Germany
alicemal@prof-benim.com

Sander M. Calisal, The University of British Columbia, Canada
sander.calisal@gmail.com

Erdal Cetkin, Izmir Institute of Technology, Türkiye
erdal cetkin@iyte.edu.tr

Raju Datla, Stevens Institute of Technology, USA
rdatla@stevens.edu

Yigit Kemal Demirel, University of Strathclyde, UK
yigit.demirel@strath.ac.uk

Cagan Diyaroglu, Sabanci University, Türkiye
cagan.diyaroglu@sabanciuniv.edu

Marcelo Risso Errera, Federal University of Parana, Brazil
errera@ufpr.br

Mo'men Mohamed Gaafary, Port Said University, Egypt
mo2mengaafary@yahoo.com

Antonio F. Miguel, University of Evora, Portugal
afm@uevora.pt

Mashud Karim, Bangladesh University of Engineering and Technology, Bangladesh
mmkarim@name.buet.ac.bd

Mehmet Kanoglu, Alanya Alaaddin Keykubat University, Türkiye
mehmet.kanoglu@alanya.edu.tr

Toru Katayama, Osaka Prefecture University, Japan
katayama@marine.osakafu-u.ac.jp

Farrukh Khalid, Istinye University, Türkiye
farrukh.khalid@istinye.edu.tr

Gorkem Kokkulunk, Yildiz Technical University, Türkiye
gorkemk@yildiz.edu.tr

Fatih Cuneyd Korkmaz, Yildiz Technical University, Türkiye
fkorkmaz@yildiz.edu.tr

Heba Leheta, Alexandria University, Egypt
heba.leheta@alexu.edu.eg

Sylvie Lorente, Villanova University, USA
sylvie.lorente@villanova.edu

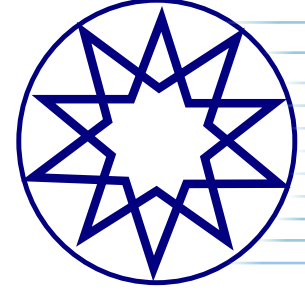
Claudio Lugni, National Research Council, Italy
claudio.lugni@cnr.it

Prasanta Kumar Sahoo, Florida Institute of Technology, USA
psahoo65@outlook.com

Radoslav Nabergoj, NASDIS PDS, Slovenia
radoslav.nabergoj@nasdispds.com

Seatific

Volume 3 Number 1 Year 2023



Editorial Board

Alparslan Oztekin, *Lehigh University, USA*
alo2@lehigh.edu

Luiz Alberto Oliveira Rocha, *Federal University of Rio Grande do Sul, Brazil*
laorochoa@gmail.com

Carlos Guedes Soares, *University of Lisbon, Portugal*
c.guedes.soares@centec.tecnico.ulisboa.pt

Tahsin Tezdogan, *University of Strathclyde, UK*
tahsin.tezdogan@strath.ac.uk

Giorgio Trincas, *University of Trieste, Italy*
trincas@units.it

Osman Turan, *University of Strathclyde, UK*
o.turan@strath.ac.uk

Nikola Vladimir, *University of Zagreb Croatia, nikola.vladimir@fsb.hr*

Burak Yildiz, *Yildiz Technical University, Türkiye*
buraky@yildiz.edu.tr

Zhiming Yuan, *Strathclyde University, UK*
zhiming.yuan@strath.ac.uk

Yalcin Yuksel, *Yildiz Technical University, Türkiye*
yuksele@yildiz.edu.tr

Kalman Ziha, *University of Zagreb, Croatia*
kalman.ziha@fsb.hr

* Sorted by the Last Name

Language Editing

Proofo Editing, *info@proofo.net*

Journal Contacts

Editor-in-Chief: Bahri Şahin, *Yıldız Technical University, İstanbul, Türkiye*
sahinb@yildiz.edu.tr

Editor: Ümit Güneş, *Yıldız Technical University, İstanbul, Türkiye*
ugunes@yildiz.edu.tr

Technical Contact: Ümit Güneş, *Yıldız Technical University, İstanbul, Türkiye*
ugunes@yildiz.edu.tr

Owner on behalf of the Yıldız Technical University: Prof. Dr. Tamer Yılmaz

Journal Description: The journal is supported by Yıldız Technical University officially, and is a blind peer-reviewed free open-access journal, published two times a year.

Publisher: Yıldız Technical University - YTU Press

Language of Publication: English

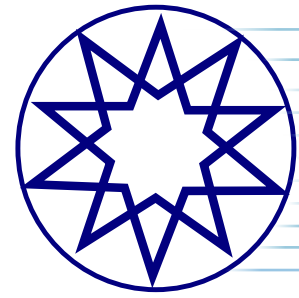
Frequency: Two issues

Publication Type: Online e-version

Press Date: December 2022

Seatific

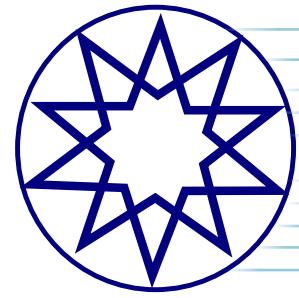
Volume 3 Number 1 Year 2023



Aim & Scope

Seatific Journal aims to present academic data to all stakeholders in the field, taking into account current developments in all types of areas related to shipping and marine sciences such as environmental impacts, energy transition, and artificial intelligence. Seatific Journal strongly aims to only publish innovative and novel studies that will contribute significantly to advancements in the fields of marine engineering, marine science, and technology.

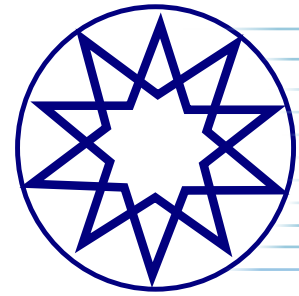
Aquaculture and Fishing
Construction
Coastal Development
Design
Electrical Equipment
Emissions
Energy
Hydrodynamics
Social Aspects
Logistics
Machinery and Control
Marine Engines
Marine Environment
Materials
Navigation
Noise
Manoeuvrability
Off-Shore
Port Operations
Propulsion
Protection of the Environment
Renewable Energy
Safety
Seakeeping
Ship Resistance
Shipyards
Stability
Structures



Contents

Research Articles

The taper ratio influence on the performance of 3-D cavitating hydrofoils moving under a free surface	1
Şakir Bal	
Optimizing the power of a variable-temperature heat reservoir Brayton cycle for a nuclear power plant in space	9
Tan Wang, Lingen Chen, Yanlin Ge, Shuangshuang Shi, Huijun Feng	
Low-computational adaptive MPC algorithmization strategy for overshoots and undershoots in instantaneous water heater stability	19
Ismael Ehtiwesh	
Thermodynamic aspects of gas generator for application in military aircraft: Some considerations	25
Bhupesh A Parate	
First and second law assessment of a solar tower power plant for electrical power production and error analysis	33
Mohd Parvez, Syed Mohammed Mahmood, Osama Khan	



Author Guidelines

- Seatific Journal is a double-blind, peer-reviewed biannually academic journal publishing articles in both English and Turkish.
- Author(s) should remove all author(s)' names and any personal information that can be used to identify the author(s).
- All articles submitted to Seatific Journal will be uploaded to iThenticate to check the similarity rate of the paper. The Seatific Journal Desk immediately rejects any articles with a similarity rate greater than 10%.
- All submitted articles to Seatific Journal are uploaded to iThenticate to check the similarity ratio of the paper. If the similarity is more than 10%, the article is directly rejected by the Seatific Journal Desk.
- In order to gain acceptance, all articles submitted to Seatific Journal for evaluation are required to have never previously been published.
- Submissions are first reviewed by the editorial board. If an article satisfies the necessary conditions for style and content, reviewers will then proceed to evaluate its suitability for publication.
- Articles under the categories listed below are acceptable for publication:

Research Articles reflecting original experimental and/or theoretical research. A coherent treatment emphasizing new insight is expected rather than a simple accumulation of data.

Review Articles including authoritative reviews of recent advances in the basic and applied sciences with emphasis on the fundamental aspects of the subject. Manuscripts are generally longer than those found in other categories, but contributions dealing in part with original research are not excluded. Contributors who are invited by the editors or who may submit outline proposals directly are offered a small royalty upon the publication of the article.

- All articles undergo evaluation by two anonymous reviewers. If necessary, the article may be sent to a third reviewer for further assessment. The publication of an article depends upon the approval of these reviewers. Author(s) must provide the necessary corrections demanded by the reviewers.
- In general, any submitted work should provide the following formatting conditions.

No page limit or required format is needed for initial submission. A template will be sent to the author(s) of accepted articles. This can also be downloaded from the link below.

Articles should be written in MS Word in Times New Roman script with 12-pt font size, spacing of 1.5 lines, 2.5 cm margins, and left-aligned.

Tables, figures, pictures, and graphs should fit within a journal page (A4). If needed, these may be written with smaller font sizes and single-spaced.

Tables and graphs should be numbered consecutively as they appear in the text. Place footnotes for tables below the table body and indicate them with superscript lowercase letters. Avoid vertical text layout. Be sparing in the use of tables, and ensure that the data presented in tables do not duplicate results described elsewhere in the article.

- Author(s) and article information should be filled out completely on the form in the system. The article should not contain any information about the author(s).
- The study must include an abstract between 150-200 words in length and 5-8 keywords.
- Author(s) should reference and explain every figure, table, and equation used in the article.
- Corresponding author(s) should also fill out the author contributions form.
- Articles should be submitted using the online submission system to initiate the editing process. An automatic confirmation e-mail will be sent after submission. If you do not receive this e-mail, please contact us via e-mail at seatific@yildiz.edu.tr
- Seatific Journal uses APA 7th Edition style formatting for references and citations. The text rules and formats specified by the Publication Manual of the American Psychological Association (APA), Seventh Edition are to be followed both for text citations and the reference list. Here are some reference examples.

Book/eBook

- Reference Section: Bejan, A., Tsatsaronis, G., & Moran, M. J. (1996). Thermal design and optimization. Wiley.
- *In-Text:* (Bejan et al., 1996)

Edited Book

- Reference Section: Torino, G. C., Rivera, D. P., Capodilupo, C. M., Nadal, K. L., & Sue, D. W. (Eds.). (2019). Microaggression theory: Influence and implications. John Wiley & Sons. <https://doi.org/10.1002/9781119466642>
- *In-Text:* (Torino et al., 2019)

Journal Article

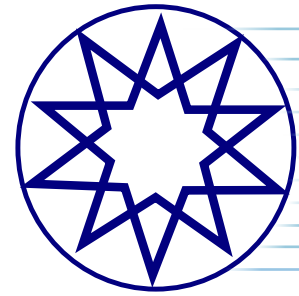
- Reference Section: Bejan, A., Gunes, U., & Sahin, B. (2019). The evolution of air and maritime transport. *Applied Physics Reviews*, 6(2), 021319. <https://doi.org/10.1063/1.5099626>
- *In-Text:* (Bejan et al., 2019)

Unpublished Dissertation or Thesis

- Reference Section: Dostal, V. (2004). A supercritical carbon dioxide cycle for next generation nuclear reactors [Unpublished doctoral dissertation]. Massachusetts Institute of Technology.
- *In-Text:* (Dostal, 2004)

Seatific

Volume 3 Number 1 Year 2023



Ethical Principles and Policies

Author Policy

Manuscript submission means the work has not been previously published (except in summary form, as part of a published conference or any academic thesis, or as an electronic preprint); it has not been evaluated anywhere else for publication; It also means that all authors or the responsible authorities of the work have given their consent to the publication of the work in question, without express or public declaration, and if accepted, its copyright in English or another language such that it cannot be published elsewhere, including electronically, without the permission of the owner.

All articles submitted to Seatific Journal will be uploaded to iThenticate to check the similarity rate of the paper. The Seatific Journal Desk immediately rejects any articles with a similarity rate greater than 10%.

Editor Policy

The Seatific Journal asks its editors to write a short commentary on their views that could potentially be seen as influencing their unbiased assessment. Such transparency is a requirement of an ethical obligation to authors and readers, as well as an equal response to the expression of opinion expected from authors, reviewers, and reviewers. The editorial staff is expected to distance themselves from decision-making arrangements that could potentially introduce a disagreement. Editors' duties:

- Publishing Decision
- Impartiality
- Security
- Disagreements and Statement
- Collaboration to take part in research

Review Policy

Reviewers of Seatific Journal are chosen from among the experts on the subjects mentioned in the manuscripts. The reasons for their selection are due to their objectivity and scientific knowledge. All those who will make the assessments are informed about what Seatific Journal expects of them. Each of them is asked to fill in an evaluation form and, if necessary, to prepare a separate report. Persons who have a disagreement on the topic of a manuscript cannot evaluate it (for example, someone who has contributed to or collaborated with one of the authors, or who is unable to provide an objective opinion on the work; also an employee or competitor of an institution whose work is being reviewed, such as people with special political and ideological views). These people should contact the editorial board and state a possible difference of opinion/conflict of interest before the manuscript is submitted to the referee committee.

- Reviews are expected to be professional, honest, courteous, punctual, and constructive. The essential elements required for a high-quality assessment are:

- Reviewers should identify the weaknesses and strengths of the work organization and methodology and comment on them.
- Reviewers should accurately and constructively criticize the author's ability to handle data (taking into account that data may be limited).
- Reviewers should identify the strengths and weaknesses of the work as a written communication tool, regardless of its composition, methodology, results, and handling.
- Reviewers should express their thoughts on whether the study has content that may raise ethical concerns or whether it has low scientific standards.
- Reviewers should provide helpful advice to the authors so that the work can be improved.
- Reviewers' criticism should be constructive and professional towards the author.
- The review should provide the editor with the correct perspective and content so that he or she can decide on acceptance (and/or revision) of the work (and/or revision).
- Reviewers are expected to identify unused works and to use citations to indicate which elements of the work have been cited previously. Reviewers should also report striking similarities between the reviewed text and any work published in another journal or submitted to Seatific Journal.
- Reviewers are sensitively expected not to contact the author directly. In many cases, the opinion of two experts will be sought; however, the views of these experts may not be the same as the final decision of the editor on the manuscript in question. Receiving advice from a reviewer, even partial, may give authors the wrong impression of the review process.

Data Access

All data on manuscripts must be available as supplementary files or stored in an external channel; they should also be made available upon request.

Changes in the Author Staff

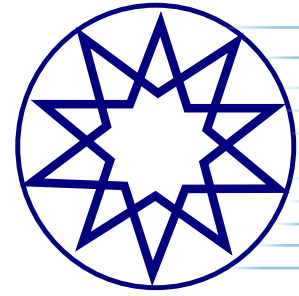
Seatific Journal acknowledges the reorganization and addition or deletion of author names prior to publishing an accepted work. Before publishing the accepted work, requests such as adding, removing, or rearranging the names of the authors should be forwarded to Seatific Journal's Secretary by the corresponding author. This request should include:

The reason for adding, removing, or rearranging the name in question and the written consent of all authors separately (by e-mail, fax, or letter) stating that they agree with this addition, removal, or rearrangement. It should also include the approval of the author who is being added or removed in such cases.

Requests not originally sent by the corresponding author will be sent by Seatific Journal's Secretary directly to the author,

Seatific

Volume 3 Number 1 Year 2023



Ethical Principles and and Policies

who must follow the procedure outlined above. The following should be noted: (1) Seatific Journal's Secretary will notify the journal's editorial board of such requests, and (2) publication of accepted work in the press will be frozen until consensus is reached on the authoring staff. After the work is published, requests to add, remove, or rearrange author names will no longer be considered.

Copyright

Authors are required to include a copyright acknowledgment letter with the manuscripts they submit to Seatific Journal. An example of this approval is below.

"The attached manuscript(s), whose author(s) and title(s) are clearly stated below, have been submitted for your consideration to be published in Seatific Journal. This manuscript/these manuscripts has/have not been published anywhere before or sent to another journal for evaluation. If any or all of the manuscripts are accepted for publication, we declare that we accept all subsequent reprint rights of each individual manuscript to belong solely and exclusively to Seatific Journal.

As the undersigned author(s), I/we accept the conditions in the Authors' Guide and expressly confirm that the paper/articles below have been written in accordance with the ethical rules set forth in this guide. In addition, all the manuscripts in question are original works, have been submitted with the documents of original copyrights, the author(s) has/have transferred all correction and control rights to Seatific Journal, and all rights including proprietary copyrights are retained if the work(s) is/are accepted. I also accept that I have transferred these rights to Seatific Journal."

Ethics & Policies

In papers to be published in journals, the manuscript should state whether ethics committee permission and/or legal/special permission is required. If it is necessary to obtain these permissions, it should be clearly presented from which institution, on what date, and with what decision or issue number.

Price Policy

Seatific Journal does not demand any article processing or submission charges from authors.

Developing the Evaluation Process

Seatific Journal's editors routinely review manuscripts for quality. Evaluation-attributed grading and other evaluator performance characteristics are periodically reviewed to ensure optimal efficiency for Seatific Journal. Performance measures such as review completion time should be used to review changes during processes that will contribute to the journal's efficiency. Individual performances are kept confidential. Editors who do not contribute to the quality of Seatific Journal may be removed from the editorial board.

Privacy

Information and ideas gained as a referee during the evaluation process are kept confidential and may not be used advantageously in any way. As the application is a privileged notification, it is to be kept strictly confidential.

- The application cannot be taken or copied by the evaluators. In addition, reviewers cannot share the work with their colleagues without the written permission of the editor.
- Reviewers and editors cannot make professional or personal use of the data, interpretations, or topics in the work (unless directly related to the evaluation) or write editorials or commentaries on the work before its publication unless they have the implicit permission of the authors.
- In case of any difference of opinion/conflict of interest, the evaluators should notify the editorial board.
- Evaluators should notify Seatific Journal if they are unable to review any work, or if they can only do so with some delay.
- Evaluators should objectively evaluate the quality of the work in question; make clear, unbiased, and constructive criticisms; and avoid personal criticism of the authors. There is no harm in letting the authors know/see the comments made by the referees. Therefore, the opinions of the referees should be clearly stated and supported so that the authors can understand the basis of the comments and evaluations.
- Reviewers can easily report any violation to the editor if they suspect any and, at the same time, they should strictly not share the status with other parties unless they have been informed by Seatific Journal to do so.



Research Article

The taper ratio influence on the performance of 3-D cavitating hydrofoils moving under a free surface

Şakir BAL*^{ID}

Department of Naval Architecture and Marine Engineering, İstanbul Technical University, İstanbul, Türkiye

ARTICLE INFO

Article history

Received: April 1, 2023

Revised: May 29, 2023

Accepted: June 8, 2023

Key words:

Cavitating hydrofoil; cavity drag; free surface; lift; taper ratio; wave drag

ABSTRACT

This article numerically investigates the taper ratio influence on the performance of three-dimensional (3-D) cavitating hydrofoils moving steadily under a free water surface. The paper modifies and expands upon a previously developed iterative boundary element method (IBEM) to solve this problem. The fluid is assumed to be inviscid and incompressible and to have irrotational flow. All variables and equations have been made non-dimensional to achieve a consistent numerical scheme and very quick convergence. The IBEM iteratively solves the hydrofoil problem and free surface problem separately through the effects they have on each other via their potential values. Both the 3-D hydrofoil surface and the free surface have been modeled using a constant strength source and constant strength doublet panels. The method's results were first validated against those regarding a tapered wing. Later, the model was applied to a tapered hydrofoil to investigate the effects of taper ratio on cavitating hydrofoil performance. The taper ratio has been found to cause a decrease in the drag coefficient on a cavitating hydrofoil, thereby causing an increase in the lift-drag ratio in an unbounded flow domain. The taper ratio also causes a slight improvement in the lift-drag ratio of the cavitating hydrofoil when moving under a free surface.

Cite this article as: Bal Ş. The taper ratio influence on the performance of 3-D cavitating hydrofoils moving under a free surface. *Seatific* 2023;3:1:1–8.

1. INTRODUCTION

Calculating the hydrodynamic performance of hydrofoils has practical importance, particularly for high-speed foil-assisted racing and sport boats (Pernod et al., 2023). The lift forces these hydrofoils produce can fully or partially support the weight of a marine vessel. However, cavitation can occur on these hydrofoils due to the high-speed flow and small submergence depths hydrofoils have below the free water surface. The taper ratio can also act as a significant geometric parameter on the hydrodynamic performance of these supporting appendages in terms of lift and drag forces and cavitation pattern on the hydrofoil surface. This study numerically investigates the effects of

the taper ratio on cavitating three-dimensional (3-D) hydrofoils moving at constant speed under a free surface using the previously developed iterative boundary element method (IBEM).

Many studies in the past have investigated 3-D hydrofoils moving under (or even piercing) a free water surface with or without cavitation (Bal et al. 2001; Lee & Kerwin, 2003; Bal, 2007; Chen, 2012; Sun & Wu, 2022). Bal et al.'s (2001) study developed an iterative panel method based on Green's theorem to solve the 3-D cavitating hydrofoil problem, applying a low-order panel method with free surface conditions. Lee and Kerwin's (2003) study utilized a high-order panel method based on B-spline fitting for the two-

*Corresponding author.

*E-mail address: sbal@itu.edu.tr



dimensional (2-D) fully submerged hydrofoil problem, but they included no free surface effects in their calculations. Still, the method was very successful at achieving lift forces. Bal (2007) applied a numerical scheme to solve the surface piercing hydrofoil problem that included the cavitation phenomenon in the calculations. That study also considered the effects from angle of attack. Meanwhile, Chen (2012) developed a novel vortex panel method for the potential flow around a 2-D hydrofoil partially submerged under a free water surface using an energy dissipation approach, with dissipative Green functions being employed in the proposed technique. Energy dissipation over a free surface has also been stated to cancel out the singularities of frequency domain integration in the Green functions. Sun and Wu (2022) presented another higher order panel method to solve the inviscid flow around a lifting body. Furthermore, different applications on 2-D bodies moving under free surface can also be found in Uslu and Bal (2008). Pernod et al. (2023) numerically investigated a 2-D submerged hydrofoil moving closely beneath a free water surface using the computational fluid dynamics (CFD) approach. They compared the results from experiments with those from other numerical methods and obtained good satisfaction between the CFD results and the experiments. Celik et al. (2014) also developed a new method for predicting cavity length on two-dimensional and three-dimensional hydrofoils using a potential-based boundary element method. For a given cavitation number, the cavity length on the surface of the two-dimensional hydrofoil was determined by considering the minimum error criterion among different cavity lengths, with the pressure recovery and termination wall models being employed as the cavity termination condition on each section. The agreement the results from this new model had with others was very satisfactory.

Meanwhile, tapered wings are well-known for generating low induced drag, thereby causing an increase in the ratio of the lift-to-drag coefficients (Anderson, 2016; Katz & Plotkin, 2001). Many experimental and numerical studies are found in the past to have occurred on the effects of the taper ratio of wings. This is a very old topic that had interested researchers. For instance, Wetzel (1955) experimentally studied the effects of the taper ratio on the lift, drag, and moment coefficients and showed the taper ratio to have a significant effect on the variation drag coefficient and lift coefficient at a particular Reynolds number. Another experimental analysis in a low-speed wind tunnel was performed to investigate the effects of the taper ratio on the aerodynamic performance of delta wings (Zhang et al., 2009). Their study included an analysis of delta wing models having taper ratios between 0-0.79 and varying with different aspect ratios. Their analysis results showed that wings with taper ratios less than 0.3 have constant lift coefficients, as well as delta wings with a taper ratio between 0.3-0.68 to have increased stall angle and maximum lift as the taper ratio increased. Guzelbey et al.'s (2019) comprehensive study was performed to investigate the effects of the taper ratio of wings on aerodynamic

performance. However, all their studies on the taper ratio effect were done for air wings, not for hydrofoils. They did not consider how very critical the cavitation phenomenon can be for 3-D hydrofoils moving under a free water surface. This current paper modifies the previously developed numerical method (IBEM; Bal & Kinnas, 2002) for cavitating or non-cavitating hydrofoils operating under a free surface and extends it to 3-D hydrofoils with taper ratios. IBEM utilizes Green's theorem (Green's second identity) and defines an integral equation that is based on this theorem. The integral equation is divided into two parts: (i) the hydrofoil part, including its wake and cavity surface, and (ii) the free surface part. These two parts of problem are solved separately. The effects each part has on the other are included iteratively via their potential values. The results from the present IBEM have been validated with experiments and extensively compared with those from other numerical methods for different previous cases (Bal et al., 2001; Bal & Kinnas, 2002, 2003). Another validation study that had not been done before has been added to the paper here. The method is then applied to a 3-D tapered hydrofoil. The effects from the taper ratio have been investigated regarding the lift and drag coefficients, as well as on the cavitation pattern and free surface deformations.

The following sections first summarize the mathematical model of the problem for the completeness of the paper and then introduces a short form for the numerical procedure. Afterward, the sections show the numerical results for a tapered hydrofoil and discuss the effects the taper ratio has on the results with and without cavitation. The paper then concludes with some remarks.

2. MATHEMATICAL MODEL

A cavitating hydrofoil below a free surface is subjected to a uniform inflow U as shown in Figure 1. The x -axis is positive in the direction of uniform inflow, the z -axis is positive upwards, and the y -axis completes the right-handed coordinate system. The origin is located on the intersection point of the mid-span and mid-chord lengths. The undisturbed free surface is located at $z = h$. The fluid is inviscid and incompressible, and the flow field is irrotational and steady. All variables and equations are non-dimensional. U and c_m are employed for this, where c_m is the mean chord length equal to the average of the c_{root} and c_{tip} values. Figure 1 shows the c_{root} (root chord length) and c_{tip} (tip chord length). The mathematical model has been previously explained in detail (Bal et al., 2001; Bal & Kinnas, 2002) and will explained in brief here for the completeness of the paper.

The perturbation potential $\phi(x, z)$ and the total potential $\Phi(x, z)$ should satisfy Laplace's equation (equation of conservation of mass) in the fluid domain:

$$\nabla^2 \Phi = 0 \text{ and } \nabla^2 \phi = 0 \quad (1)$$

The perturbation potential ϕ should also satisfy the following boundary conditions:

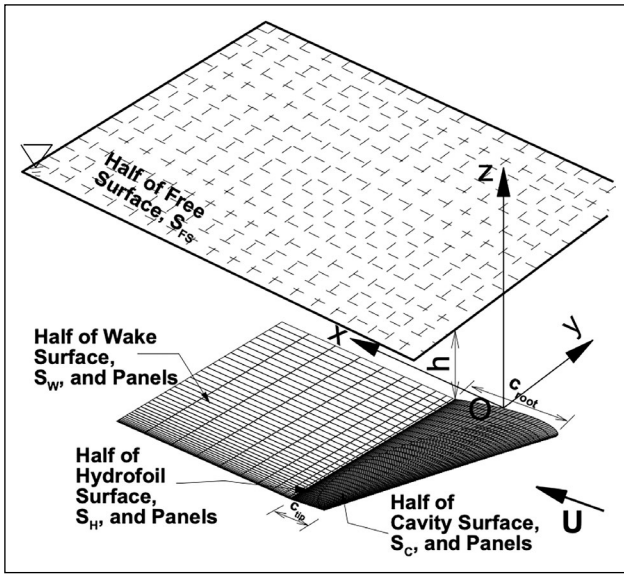


Figure 1. Coordinate system for the 3-D cavitating hydrofoil problem. Only half of the hydrofoil, its wake, and free surface are shown due to the property of symmetry.

1. Kinematic boundary condition on the hydrofoil surface: The total velocity normal to the hydrofoil surface should be zero:

$$\frac{\partial \phi}{\partial n} = -\frac{|\vec{n}|}{c_m} \text{ on } S_H \quad (2)$$

where \vec{n} is the unit normal vector on the hydrofoil surface and its direction is toward the water. S_H represents the hydrofoil surface.

2. Kutta and wake conditions: The Kutta condition forces a finite velocity at the trailing edge of the hydrofoil along its span-wise direction:

$$\nabla \phi = \text{finite}; \text{ at the trailing edge} \quad (3)$$

The force should be zero at the wake surface. The wake surface is assumed to be constant at $z=0$. The dipole strength at the trailing edge is transferred to the wake surface, thus ensuring the zero pressure jump on the wake surface. Eq. (3) can then be reduced to an iterative Morino's Kutta condition as shown in Kinnas and Hsin (1992) as:

$$\phi^+ - \phi^- = \Delta \phi_w \quad (4)$$

where ϕ^+ and ϕ^- are the potential values at the respective upper and lower sides of the hydrofoil trailing edge. Details on this condition can be found in Kinnas and Hsin (1992).

3. Dynamic boundary condition on the cavity surface: The pressure should be equal to p_c (vaporize pressure of water) on the cavity surface. Applying Bernoulli's equation, the total velocity q_c can be given as in Kinnas and Fine (1993):

$$q_c / U = \sqrt{1 + \sigma} \quad (5)$$

where σ is the cavitation number defined as:

$$\sigma = \frac{p - p_c}{\frac{1}{2} \rho U^2} \quad (6)$$

Here, p is the sum of the atmospheric pressure (p_{atm}) and the static pressure (ρgh) far upstream.

4. Cavity closure condition: The cavity is forced to close at its trailing edge (see Kinnas & Fine, 1993). In addition, the cavity detachment point is assumed to be the leading edge of the hydrofoil. This study applies the fixed cavity number solution, which assumes that the cavity number is known and that the cavitation length (cavity volume and cavity planform) must be determined using an iterative technique. Details again can be found in Kinnas and Fine (1993).

5. Linearized free surface condition: If the kinematic and dynamic free surface conditions are combined together and the higher-order terms are neglected, the following linearized free surface equation in non-dimensional form is obtainable as:

$$\frac{\partial^2 \phi}{\partial x^2} + Fr_c^{-2} \frac{\partial \phi}{\partial z} = 0 \text{ on } z=h \quad (7)$$

Here, Fr_c is the Froude number ($Fr_c = \frac{U}{\sqrt{g c_m}}$), which is based on the mean chord length, and g is the force of gravity. The corresponding wave elevation in linearized form is also obtainable as:

$$\zeta = -Fr_c^2 \frac{\partial \phi}{\partial x} \quad (8)$$

Note that ζ is the non-dimensional wave elevation.

6. Radiation condition: Upstream waves should not be on the free surface. This means that the first and second derivatives of the perturbation potential with respect to x are equal to zero for the upstream region on the free surface, which has been demonstrated in Bal and Kinnas (2002) as:

$$\frac{\partial^2 \phi}{\partial x^2} = \frac{\partial \phi}{\partial x} = 0 \text{ as } x \rightarrow -\infty \quad (9)$$

3. THE NUMERICAL APPROACH USING IBEM

According to Green's third identity, the perturbation potential on the hydrofoil surface, its wake, and the free surface can be given as follows:

$$2\pi\phi = \int_{S_H + S_{FS}} \left(\phi \frac{\partial G}{\partial n} - \frac{\partial \phi}{\partial n} G \right) dS + \int_{S_W} \Delta \phi_w \frac{\partial G}{\partial n^+} dS \quad (10)$$

where S_H , S_W and S_{FS} are the respective boundaries of the hydrofoil surface, the wake surface, and the free water surface. G is the Green function, and $G=1/r$, with r being the distance between the singularity point and field point. $\Delta \phi_w$ is the potential jump across the wake surface as given in Eq. (4), and n^+ is the unit vector normal to the wake surface pointing upwards. The present study has modified the iterative method presented mainly in Bal et al. (2001) and applied it to solve Eq. (10). The problem here is divided into two isolated parts: (1) the hydrofoil part, including its wake and cavity surface, and (2) the free surface part. After making some modifications and applying the kinematic boundary condition to the hydrofoil surface and the linearized free surface condition to the $z = h$ plane, Eq. (10) can be divided into two integral equations:

$$2\pi\phi_H = \int_{S_H} \left(\phi \frac{\partial G}{\partial n} + n_x G \right) dS + \int_{S_H} \Delta \phi_w \frac{\partial G}{\partial n^+} dS + 4\pi(\phi_{FS}) \quad (11)$$

$$2\pi\phi_{FS} = \int_{S_{FS}} \left(\phi \frac{\partial G}{\partial n} + Fr_c^2 \frac{\partial^2 \phi}{\partial x^2} G \right) dS + 4\pi(\phi_H) \quad (12)$$

Here, n_x is the x component of the normal vector on the hydrofoil surface. Integral Equations (11) and (12) can be solved iteratively using a low-order panel method. The potentials ϕ_H and ϕ_{FS} can be updated during the iterative process. The hydrofoil surface and free surface are discretized into small rectangular panels with constant strength source and dipole distributions. The discretized integral equations produce two matrix equations with unknown potentials and can be solved by any matrix solver. The iterative method presented here has two main advantages:

1. Solving for each sub-problem is easier to organize than solving the full problem, and
2. Each sub-problem requires less computational cost (time and memory) than the cost for solving the full problem. Therefore, the total computational time and memory using the iterative process is less than the cost of solving the full problem.

The details for this IBEM can be found in Kinnas and Bal (2002).

4. NUMERICAL RESULTS

The present IBEM has already been validated extensively by comparing the results with experimental data and other numerical methods, as given in Kinnas and Fine (1993) and Bal et al. (2001). Firstly, another validation study has been performed here. The results using the current IBEM have been validated with the experiments for a tapered wing in Cahill and Gottlieb (1950). The tapered wing conforms to the NACA 65A006 airfoil section (Abbott and Doenhoff, 1959). The dihedral angle and twist angle are both zero, while the taper ratio (c_{tip}/c_{root}) is 0.6. Other non-dimensional geometrical parameters are given in Table 1.

The total number of panels used on the hydrofoil surface is $80 \times 80 = 6,400$, with the number of panels in the x and y directions being 80 and 80. The full cosine spacing technique has been applied both in the chordwise and spanwise directions. No free surface effect or cavitation was considered for this particular case. Figure 2 shows the panels used on the full wing with an x-z view of the wing. Figure 3 also shows the lift coefficient and induced drag coefficient ($C_L = \frac{L}{\frac{1}{2}\rho AU^2}$, $C_{D_{ind}} = \frac{D_{ind}}{\frac{1}{2}\rho AU^2}$; L = lift, D_{ind} = induced

drag due to lift, and A = planform area of the wing) in an unbounded flow domain for this study as well as for the experiments taken from Cahill and Gottlieb (1950). A lift coefficient of -0.01 at a 0° angle of attack was measured in the experiments. The possible reason for this may be the very small error introduced while trying to fix the wing's angle of attack in the experiments. Therefore, the lift coefficients have been shifted by an amount of 0.01, which produces a zero-lift coefficient at $\alpha = 0^\circ$ (0° angle of attack), as also suggested in Cetinkaya and Unal (2020). The agreement is very satisfactory up to angle of attack of 8° , beyond which discrepancies occur between the two results (i.e., experiments and IBEM) due to possible flow separation and

Table 1. Geometric details of the wing used in the validation study

Nondimensional span (s)	2
Root (mid-section) chord (c_{root})	0.625
Tip-section chord (c_{tip})	0.375
Sweep Angle	0°
Aspect ratio ($AR = s^2/Ar$)	4

vortices. The present IBEM has not modeled these physical phenomena. Note also that an $\alpha = 12^\circ$ is the stall angle. The induced drag coefficient due to lift force has also been added to the same figure, with induced drag increasing more than the lift coefficient as angle of attack increases. In addition, the non-dimensional pressure distributions on the mid-strip and tip strip have been demonstrated in Figure 4 at $\alpha = 5^\circ$. Here, c represents the local chord lengths, namely the mid-strip (section) chord length and tip strip (section) chord length. This shows the loading on the tip section of the hydrofoil to be decreasing as expected.

After this validation, two hydrofoils, namely a rectangular hydrofoil (taper ratio [TR] = $c_{tip}/c_{root} = 1$) and a tapered hydrofoil (TR=3) have been selected to show the effects

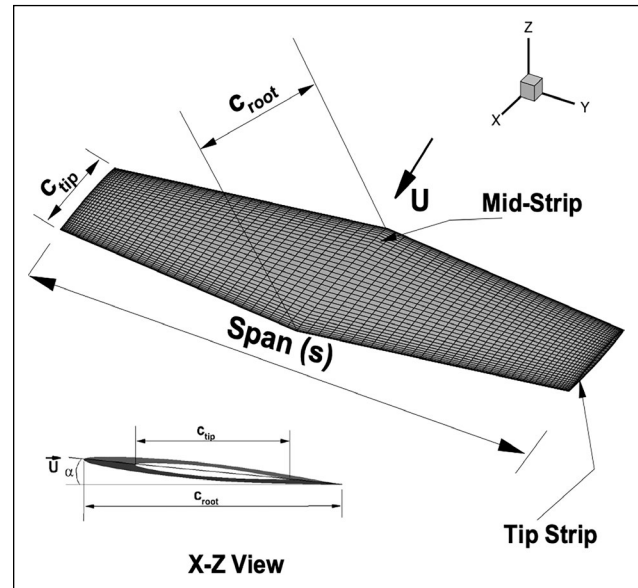


Figure 2. Parameters and panels on the tapered hydrofoil used for validation.

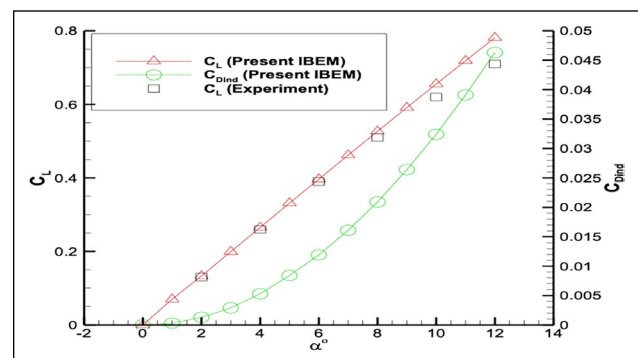


Figure 3. Comparison of lift coefficients with experiments.

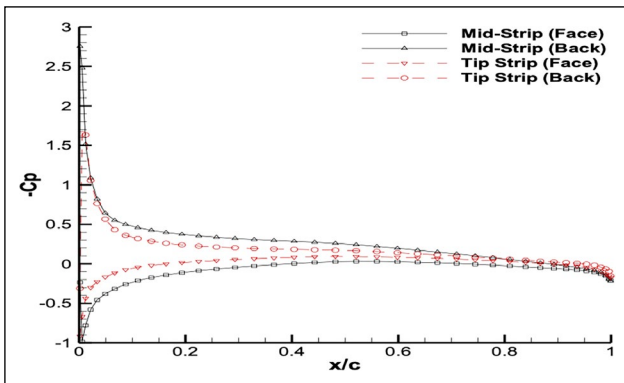


Figure 4. The non-dimensional pressure distribution on mid-section and tip section.

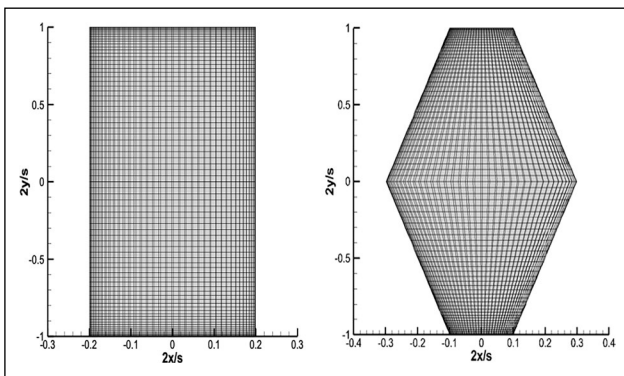


Figure 5. The rectangular (left) and tapered (right) hydrofoils with panels used in the calculations.

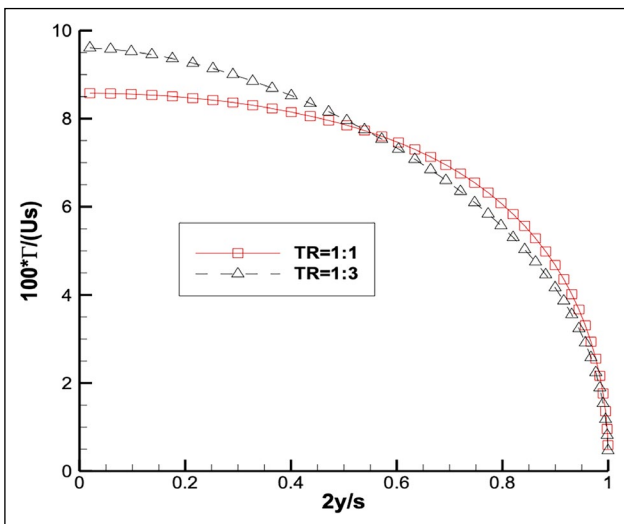


Figure 6. Non-dimensional circulation distribution of rectangular hydrofoil and tapered hydrofoil with no cavitation and no free surface effects. Only half of the distributions are shown due to symmetry.

the taper ratio has on the performance of the hydrofoil in an unbounded flow domain (no free surface effect). Both hydrofoils have the same aspect ratio of 5 ($AR=s^2/A$; A =planform area of the hydrofoil). The planform areas of both hydrofoils are kept constant. They have no sweep angle and no dihedral angle. Twist angle is also zero. Both

Table 2. Lift and drag coefficients of both hydrofoils in unbounded flow domain

No cavitation	Rectangular (TR=1:1)	Tapered (TR=1:3)
C_L	0.3508	0.3590
$C_{D_{ind}}$	0.0086	0.0087
$C_L/C_{D_{ind}}$	40.9	41.3

Table 3. Lift and drag coefficients of both cavitating hydrofoils in unbounded flow domain

With cavitation, $\sigma=0.7$	Rectangular (TR=1:1)	Tapered (TR=1:3)
C_L	0.3650	0.3634
$C_{D_{ind}} + C_{D_{cay}}$	0.0214	0.0184
$CL/C_{D_{ind}} + C_{D_{cay}}$	17.0	19.8

hydrofoils have the NACA 0012 sections. The angle of attack is fixed and taken as $\alpha=5^\circ$. The cavitation number is also fixed and equal to $\sigma=0.7$. The total number of panels on the hydrofoil surface is $80 \times 80=6,400$, with the number of panels in the x direction and y direction being chosen as 80 and 80. The full cosine spacing, both in the chord direction and span direction, have been utilized for all the following simulations. Figure 5 shows both the rectangular hydrofoil and tapered hydrofoil.

First, the non-dimensional circulation distribution along the span direction for both the rectangular and tapered non-cavitating hydrofoils are shown in Figure 6. TR=1:1 and TR=1:3 (TR meaning Taper Ratio) represent the rectangular hydrofoil and tapered hydrofoils, respectively. The loading on the tapered hydrofoil increases more compared to that of the rectangular hydrofoil. This is much clearer in Table 2, which shows the lift and induced drag coefficients for the non-cavitating hydrofoils. Note that the lift coefficient and thereby the ratio of the lift coefficient to the induced drag coefficient increase slightly for the tapered hydrofoil. Next, the lift and the drag (induced+cavity) coefficients for cavitating hydrofoil ($\sigma=0.7$) were calculated, with the results given in Table 3. Note that the lift coefficients are almost same, but the ratio of the lift coefficient to the drag (induced+cavity) coefficient has increased for the tapered hydrofoil. This is due to the decrease in the drag (induced+cavity) coefficient. The cavity shapes on both hydrofoils for this particular case are also shown in Figure 7. As can be seen in this figure, the cavitation formation has moved from middle region to the tip region. This is much clearer in Figure 8.

The free surface effects are then included into the calculations. The ratio of submergence depth of the hydrofoil below the free surface to the mean chord length is fixed and equal to $h/c_m=1.0$. The mean chord length is defined as $c_m=(c_{tip}+c_{root})/2$. The lift coefficients for both the cavitating rectangular and tapered hydrofoils at the

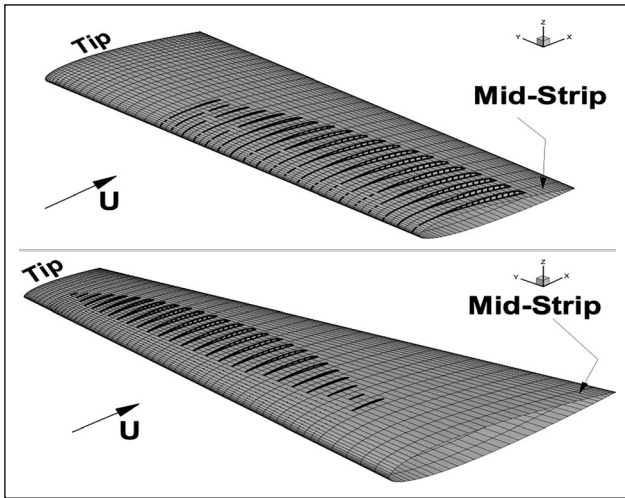


Figure 7. Cavity shapes for rectangular (up) and tapered (down) hydrofoils in unbounded flow domain. Only half of the distributions have shown due to symmetry, $\alpha=5^\circ$, $\sigma=0.7$.

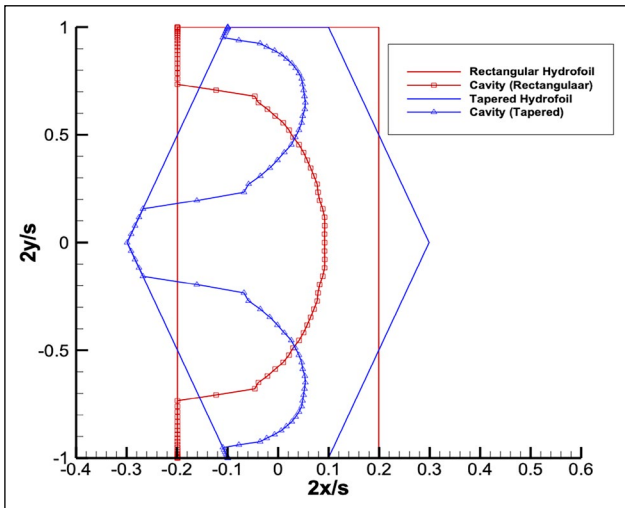


Figure 8. Cavity planforms for rectangular and tapered hydrofoils in unbounded flow domain, $\alpha=5^\circ$, $\sigma=0.7$.

mean chord - based Froude number ($Fr_c=0.8$) are given in Table 4. Free surface causes an increase in lift coefficient as well as in drag coefficient (total drag coefficient is now equal to induced+cavity+wave) compared to those in the unbounded flow domain (Table 3) for this particular case. Meanwhile, the lift-to-drag ratio of the tapered wing is slightly better than that of the rectangular hydrofoil.

The cavity shapes due to the free surface effect on both the rectangular and tapered hydrofoils are shown in Figures 9 and 10, respectively. As can be seen from these figures, the

Table 4. Lift and drag coefficients of both cavitating hydrofoils with free surface effect

With cavitation, $\sigma=0.7$, $Fr_c = 0.8$, $h/c_m = 1.0$	Rectangular (TR=1:1)	Tapered (TR=1:3)
C_L	0.4178	0.4294
$C_{D_{ind}} + C_{D_{cay}} + C_{D_{way}}$	0.0359	0.0350
$CL/(C_{D_{ind}} + C_{D_{cay}} + C_{D_{way}})$	11.6	12.3

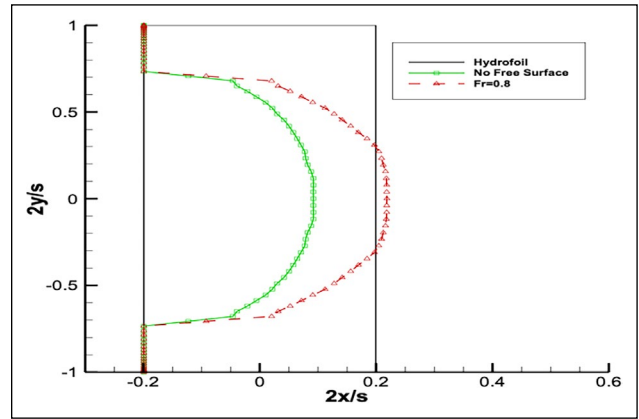


Figure 9. Cavity planforms for rectangular hydrofoil, $\alpha=5^\circ$, $\sigma=0.7$, $h/c_m=1.0$.

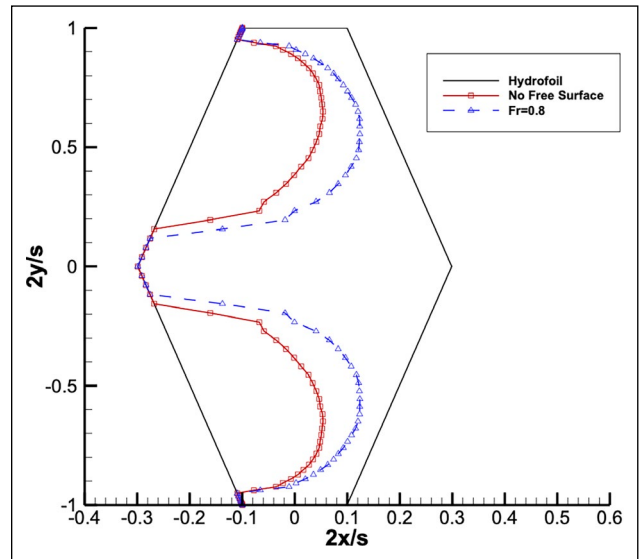


Figure 10. Cavity planforms for tapered hydrofoil, $\alpha=5^\circ$, $\sigma=0.7$, $h/c_m=1.0$.

free surface causes longer cavity lengths for this particular case. Free surface behaves like a solid wall for this particular case, (Bal & Kinnas, 2002).

Figure 11 demonstrates the wave deformations on the free surface for both hydrofoils, showing the Kelvin wave system to have occurred. This can also be seen very clearly in Figure 12, which shows the Kelvin wave contours on the free surface for both the cavitating rectangular and tapered hydrofoils at $\alpha=5^\circ$, $\sigma=0.7$, $h/c_m=1.0$, $Fr_c=0.8$.

4. CONCLUSION

A previously developed iterative numerical method has been made non-dimensional and extended to study the taper ratio effect on 3-D cavitating hydrofoils, with some extensive numerical results being presented. The iterative numerical method was first applied to a tapered rectangular hydrofoil for a validation study, and very good agreement has been found between the results from the present IBEM and those from the experiments. The numerical method was later applied to rectangular and tapered cavitating

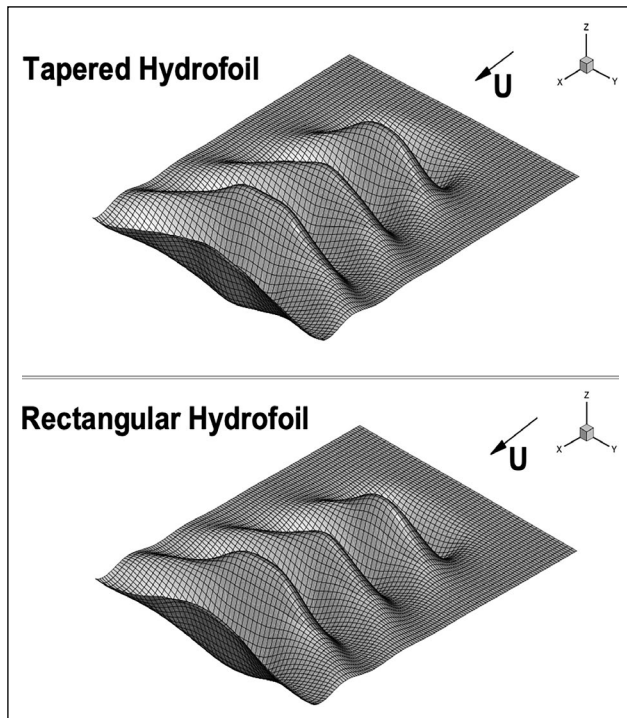


Figure 11. Wave deformation on free surface for both hydrofoils; $\alpha=5^\circ$, $\sigma=0.7$, $h/c_m=1.0$, $Fr_c=0.8$.

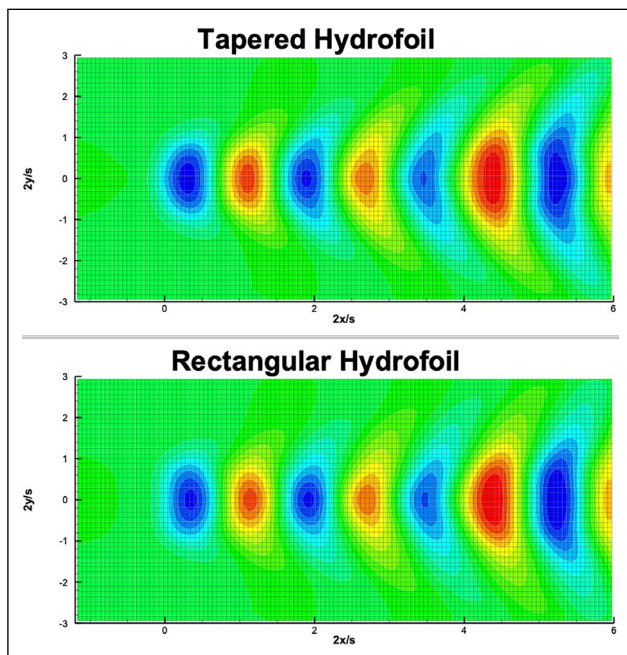


Figure 12. Kelvin wave contours on free surface for both hydrofoils; $\alpha=5^\circ$, $\sigma=0.7$, $h/c_m=1.0$, $Fr_c=0.8$.

hydrofoils to predict hydrodynamic performance, with the following conclusions having been found:

1. Cavitation causes an increase in loading on the hydrofoil due to a virtual camber effect.
2. Cavitation causes an increase in lift coefficient as well as in drag coefficient. But the lift-to-drag ratio decreases drastically due to the increase in drag coefficient being much higher.

3. The taper ratio causes a decrease in the drag coefficient on a cavitating hydrofoil, thereby causing an increase in lift-to-drag ratio.
4. The taper ratio causes a slight improvement to the lift-to-drag ratio for the cavitating hydrofoil moving under a free surface.

NOMENCLATURE

A	: Planform area
AR	: Aspect ratio
c_m	: Mean chord length
c_{tip}	: Chord length at tip
c_{root}	: Chord length at root (mid-section)
C_{Dcav}	: Cavity drag coefficient
C_{Dind}	: Induced drag coefficient due to lift
C_{Dtot}	: Total drag coefficient
$C_{D_{wav}}$: Wave drag coefficient
C_L	: Lift coefficient
C_p	: Pressure coefficient
D_{cav}	: Cavity drag
D_{ind}	: Induced drag
D_{tot}	: Total drag
D_{wav}	: Wave drag
Fr	: Chord-based Froude number, $Fr : U/(gcm)0.5$
g	: Gravitational acceleration
h	: Submerged depth of hydrofoil below free surface
IBEM:	Iterative Boundary Element Method
L	: Lift force
\vec{n}	: Unit normal vector directed from hydrofoil to water
p	: Pressure
p_c	: Cavity pressure
p_o	: Reference pressure
q_c	: Velocity on cavity surface
s	: Span
S_C	: Cavity surface
S_{FS}	: Free surface
S_H	: Hydrofoil surface
S_W	: Wake surface
t_{max}	: Maximum thickness
U	: Velocity of incoming flow
α	: Angle of attack
Φ	: Total potential
ϕ	: Perturbation potential
ρ	: Density of water
σ	: Cavitation number
ζ	: Wave elevation

DATA AVAILABILITY STATEMENT

The published publication includes all graphics and data collected or developed during the study.

CONFLICT OF INTEREST

The author declared no potential conflicts of interest with respect to the research, authorship, and/or publication of this article.

ETHICS

There are no ethical issues with the publication of this manuscript.

FINANCIAL DISCLOSURE

The authors declared that this study has received no financial support.

REFERENCES

- Abbott, I. H., & Doenhoff, A. V. (1959). *Theory of wing sections* (1st ed.). Dover Publications.
- Anderson, J. (2016). *Fundamentals of aerodynamics* (6th ed.). McGraw-Hill.
- Bal, S., Kinnas, S. A., & Lee, H. (2001). Numerical analysis of 2-D and 3-D cavitating hydrofoils under a free surface. *Journal of Ship Research*, 45(1), 34–49. [\[CrossRef\]](#)
- Bal, S., & Kinnas, S. A. (2002). A BEM for the prediction of free surface effect on cavitating hydrofoils. *Computational Mechanics*, 28, 260–270. [\[CrossRef\]](#)
- Bal, S., & Kinnas, S. A. (2003). A numerical wave tank model for cavitating hydrofoils. *Computational Mechanics*, 32(4-6), 259–268. [\[CrossRef\]](#)
- Bal, S. (2007). High-speed submerged and surface piercing cavitating hydrofoils, including tandem case. *Ocean Engineering*, 34, 1935–1946. [\[CrossRef\]](#)
- Cahill, J. F., & Gottlieb, S. M. (1950). *Low-speed aerodynamic characteristics of a series of swept wings having NACA 65A006 airfoil sections* (Report No. NACA RM L9J20). National Aeronautics and Space Administration.
- Celik, F., Arikan, Y. O., & Bal, S. (2014). Numerical simulation of two- and three-dimensional partially cavitating hydrofoils. *Ocean Engineering*, 78, 22–34. [\[CrossRef\]](#)
- Cetinkaya, A., & Unal, U. O. (2020). A computational study into the effect of winglets on the performance of fully submerged hydrofoils. *Applied Ocean Research*, 104, Article 102357. [\[CrossRef\]](#)
- Guzelbey, I. H., Eraslan, Y., & Dogru, M. H. (2019). Effects of taper ratio on aircraft wing aerodynamic parameters: A comparative study. *European Mechanical Science*, 3(1), 18–23. [\[CrossRef\]](#)
- Katz, J., & Plotkin, A. (2001). *Low speed aerodynamics: From wing theory to panel methods* (2nd ed.). McGraw-Hill. [\[CrossRef\]](#)
- Kinnas, S. A., & Fine, N. E. (1993). A numerical nonlinear analysis of the flow around two- and three-dimensional partially cavitating hydrofoils. *Journal of Fluid Mechanics*, 254, 151–181. [\[CrossRef\]](#)
- Kinnas, S. A., & Hsin, C. Y. (1992). A boundary element method for the analysis of the unsteady flow around extreme propeller geometries. *AIAA Journal*, 30, 688–696. [\[CrossRef\]](#)
- Lee, C. S., & Kerwin, J. E. (2003). A B-spline higher order panel method applied to two-dimensional lifting problem. *Journal of Ship Research*, 47(4), 290–298. [\[CrossRef\]](#)
- Pernod, L., Sacher, M., Wackers, J., Augier, B., & Bot, P. (2023). Free surface effects on two-dimensional hydrofoils by RANS-VOF simulations. *Journal of Sailing Technology*, 8(1), 24–33. [\[CrossRef\]](#)
- Sun, S. Y., & Wu, G. X. (2022). Inviscid flow passing a lifting body with a higher order boundary element method. *Engineering Analysis with Boundary Elements*, 136, 144–157. [\[CrossRef\]](#)
- Uslu, Y., & Bal, S. (2008). Numerical prediction of wave drag of 2-D and 3-D bodies under or on a free surface. *Turkish Journal of Engineering and Environmental Sciences*, 32, 177–188.
- Wetzel, B. E. (1955). Effect of taper ratio on lift, drag, and pitching moment characteristics of thin wings of aspect ratio 3 with 53.1° sweepback of leading edge at subsonic and supersonic speeds. NACA RM A54J20.
- Zhang, P. F., Wang, J. J., Liu, Y., & Wu, Z. (2009). Effect of taper ratio on aerodynamic performance of cropped non-slender delta wings. *Journal of Aircraft*, 46(1), 320–325. [\[CrossRef\]](#)



Research Article

Optimizing the power of a variable-temperature heat reservoir Brayton cycle for a nuclear power plant in space

Tan WANG^{1,2,3} , Lingen CHEN^{*1,2,3} , Yanlin GE^{1,2,3} , Shuangshuang SHI^{1,2,3} , Huijun FENG^{1,2,3}

¹Institute of Thermal Science and Power Engineering, Wuhan Institute of Technology, Wuhan, China

²Hubei Provincial Engineering Technology Research Center of Green Chemical Equipment, Wuhan, China

³School of Mechanical & Electrical Engineering, Wuhan Institute of Technology, Wuhan, China

ARTICLE INFO

Article history

Received: March 22, 2023

Revised: May 5, 2023

Accepted: May 8, 2023

Key words:

Endoreversible closed
 Brayton cycle; finite time
 thermodynamics; optimal
 performance; power
 optimization; space power
 plant; variable-temperature heat
 reservoir cycle

ABSTRACT

This study establishes a variable-temperature heat reservoir endoreversible simple closed Brayton cycle model for a nuclear power plant in space and derives its thermal efficiency (TEF) and power output (POW). The maximum POW (P_{\max}) for a fixed total heat transfer area of a radiator panel and two heat exchangers (HEXs) is obtained by optimizing the area distributions (f_{HP} , f_L , and f_R) among the two HEXs and radiator panel, the double maximum POW ($P_{\max,2}$) is obtained by optimizing the inlet temperature (T_{lin}) of the cooling fluid in the low temperature heat sink, and the triple maximum POW ($P_{\max,3}$) is further obtained by optimizing the thermal capacity rate matching (C_{Wf}/C_H) between the heat reservoir and working fluid. When f_{HP} , f_L , and f_R are optimized, P_{\max} increases by 4.33% compare to the initial POW (P); when T_{lin} is furtherly optimized, $P_{\max,2}$ increases by 6.33% compare to P and increases by 1.86% compared to P_{\max} , with $P_{\max,3}$ increasing by 11.76%, 7.13%, and 5.17% compared to P , P_{\max} , and $P_{\max,2}$, respectively.

Cite this article as: Wang T, Chen L, Ge Y, Shi S, Feng H. Optimizing the power of a variable-temperature heat reservoir Brayton cycle for a nuclear power plant in space. Seatific 2023;3:1:9–18.

1. INTRODUCTION

In the face of the requirements of deep space exploration missions, establishing a high-conversion efficiency, reliable, and compact space-based power plant (SPP) that can respond to challenges has become necessary in recent years. Three ways presently exist for an SPP to provide energy: chemical, solar, or nuclear energy. Among these options, nuclear energy appears as a possible alternative for generating large amounts of energy long term and reducing fuel mass. Furthermore, the SPP would require the maximum power-to-mass ratio for space propulsion purposes. Therefore, a practical energy conversion system must strike a compromise between high conversion efficiency and compactness. This relationship

must be balanced during the design process. The main components of SPP are divided into three parts: the reactor, the energy conversion device, and the radiator. The space energy conversion system can be separated into static (thermoelectric converter and thermionic conversion) and dynamic (Stirling, Brayton, and Rankine heat engines) components.

Due to the high power density, high conversion efficiency, stability, and reliability, the closed Brayton cycle and its combined cycles have been used in aircraft, the marine industry, power plants, and space-based power plants. Some scholars (Gonca & Sahin, 2016; Gonca, 2017a, 2017b, 2018; Gonca & Genc, 2019; Gonca & Başhan, 2019; Gonca & Guzel, 2022) have optimized gas turbine cycles

*Corresponding author.

*E-mail address: lingenchen@hotmail.com, 2506715339@qq.com



(Gonca & Sahin, 2016; Gonca, 2017a, 2018), gas-mercury cycles (Gonca, 2017b; Gonca & Genc, 2019) and gas-steam combined cycles (Gonca & Başhan, 2019; Gonca & Guzel, 2022) with exergetic (Gonca, 2017a, 2017b; Gonca & Guzel, 2022), exergo-economic (Gonca & Guzel, 2022) and thermo-ecological (Gonca & Sahin, 2016; Gonca, 2017a, 2017b, 2018; Gonca & Genc, 2019; Gonca & Başhan, 2019) performances as the optimization objectives and analyzed the effects of different working fluids, turbine operations, and design parameters on cycle performances.

In order to establish a high conversion efficiency, reliable, and compact SPP, some scholars have introduced classical thermodynamics theory into the performance optimization of the closed Brayton cycle for SPPs (El-Genk & Tournier, 2009; Liu et al., 2020; Wang et al., 2021a; Miao et al., 2022; Toro & Lior, 2017). El-Genk and Tournier (2009) established a closed Brayton cycle model for SPP with an inert gas and binary mixture as a coolant and analyzed the influence of the working fluid (WF) on plant performance and turbine size. Their results showed that a cycle with an indirect closed Brayton cycle has higher thermal efficiency (TEF) than one with a single compressor and that the cycle TEF is almost unaffected by the WF's molecular weight. Liu et al. (2020) took the mass of the HEXs of a closed Brayton cycle for an SPP as the optimization objective, minimizing the total mass of the plant by optimizing the key parameters of the system components with NSGA-II algorithm, thus obtaining a Pareto frontier of key parameters. Wang et al. (2021a) established a closed Brayton cycle model for an SPP with a gas-cooled reactor as the hot side of the heat reservoirs (HRs) and analyzed and optimized the cycle performances. Their results showed the highest temperature that the fuel can reach and how safe the device is under optimal operation. Miao et al. (2022) established a recompressed supercritical N_2O -He mixture closed Brayton cycle model for an SPP. They comprehensively studied and optimized important parameters of the plant such as split ratio and pressure ratio and obtained an optimal TEF and closed Brayton cycle rotating unit mass for the cycle. Additionally, Toro and Lior (2017) introduced classical thermodynamics theory into the performance optimization of Stirling cycles for SPPs and analyzed the effects of main cycle parameters on the relationship between TEF and POW for Stirling cycles operating with different WFs.

The theory of finite-time thermodynamics (FTT; Andresen, 1983; Bejan, 1996; Chen et al. 1999; Berry et al., 2020; Andresen & Salamon, 2022) is an innovation of classical thermodynamic theory. FTT can consider the effects of heat transfer loss and the limitations of time and heat exchanger (HEX) area between the heat reservoir (HR) and WF which are largely ignored in classical thermodynamics. Many researchers have introduced FTT into the performance optimizations of thermal cycles and processes, including the optimal performances of the Carnot cycles (Curzon & Ahlborn, 1975; Valencia-Ortega et al., 2021), Stirling engines (Xu et al., 2022), diesel engines (Wu, Feng et al., 2021; Ge et al., 2021), dual cycles (Ge et al., 2022), Kalina

cycles (Feng et al., 2020), dual-Miller cycles (Ebrahimi, 2021), organic Rankine cycles (Park & Kim, 2016; Wu, Ge et al., 2020; Feng et al., 2021), combined cycles (Gonca & Guzel, 2022; Wu et al., 2021), thermoelectric devices (Chen et al., 2020a; Chen et al., 2021a; Chen & Lorenzini, 2022a), thermal Brownian cycles (Qi et al., 2021a, 2021b; Chen et al., 2022; Qi et al., 2022a, 2022b), thermoradiative devices (Li & Chen, 2021; Zhang, Yang et al. 2021), blue engines (Lin et al., 2022), electron engines (Ding et al., 2021; Qui et al., 2021a), thermionic devices (Qiu et al., 2021b), methane reforming (Chen et al., 2022b), chemical engines (Chen & Xia, 2022a, 2023a), chemical pumps (Chen et al., 2023a, 2023b), Brayton cycles (Ibrahim et al., 1991; Ust et al., 2006; Chen et al. 2020b, 2020c; Qui et al., 2022; Jin et al., 2022), and refrigeration cycles (Chen & Lorenzini, 2022b), as well as the optimal configurations of refrigeration cycles (Badescu, 2021; Paul & Hoffman, 2022), heat-transfer systems (Badescu, 2022; Chen & Xia, 2022b), variable-temperature-reservoir heat engines (Li & Chen, 2022; Chen & Xia, 2022c), methanol synthesis (Li et al., 2022), variable-potential-reservoir chemical engines (Chen & Xia, 2022d, 2022e, 2023b, 2023c), and commercial engines (Chen, 2011; Chen & Xia, 2022f). Thermal cycles are divided into two types based on the nature of the cycle: steady flow cycles (Chen et al., 1996; Feidt, 2017) and reciprocating cycles (Curzon & Ahlborn, 1975; Muschik & Hoffman, 2020). For the steady-flow heat engine cycle, considering the variable-temperature HR can have the cycle more closely approach the working state of actual heat engines. Therefore, some scholars have studied the steady-flow cycle under the condition of variable-temperature HRs (Ust et al., 2006; Ibrahim & Bourisli, 2021).

Some scholars have introduced FTT into the performance optimization of Stirling and Carnot engine cycles for SPPs (de Moura et al., 2022a, 2022b; Wang et al., 2021b, 2022). De Moura et al. (2022a, 2022b) established a Stirling engine model for an SPP, obtained a compact system with optimal temperature conditions for TEF by optimizing the temperature of the HRs of the system, and analyzed different the effects of the Stirling engine structural parameters on final system performance. Wang et al. (2021b, 2022) respectively established endoreversible and irreversible Carnot cycle models for SPPs and obtained the plant double-maximum POW by optimizing the area distributions of the HEXs and temperature of the low temperature heat sink.

Some scholars (Zhang, Liu et al., 2021; Romano & Ribiero, 2021) introduced FTT into the performance optimizations of a closed Brayton cycle for SPPs. Zhang, Liu et al. (2021) established a supercritical CO_2 closed Brayton cycle model for an SPP using a sodium-cooled reactor as the hot side of the HR, derived the relationship between TEF and POW, and obtained optimal cycle characteristics and operating parameters. Romano and Ribeiro (2021) established a regenerative closed Brayton cycle model for an SPP, obtained the optimal inlet temperature for the cold side of the HEX and optimal heat source temperature by minimizing specific mass.

Existing FTT research on closed Brayton cycle models for SPPs have not optimized HEX area or HR temperature, nor have they yet obtained the optimal inlet temperature of a cooling fluid in a low temperature heat sink or optimize thermal capacity rate matching between the HR and WF. Applying FTT to SPPs is crucial for establishing a theoretical system, and based on Ust et al. (2006), this paper will establish a variable temperature HR endoreversible closed Brayton cycle model for an SPP. For a fixed total heat transfer area of the radiator panel and two HEXs, the maximum POW of the plant will be obtained by optimizing the area distributions among the radiator panel and two HEXs, the double-maximum POW will be obtained by optimizing the inlet temperature of the cooling fluid in the low temperature heat sink, and the triple-maximum POW will be obtained by optimizing thermal capacity rate matching between the HR and WF. The study will also investigate the impacts the cycle parameters have on the triple-maximum POW.

2. MODEL DESCRIPTION AND PERFORMANCE INDICATORS

Figure 1 shows the diagram of the established model. The model consists of two parts: the first part is the ordinary closed Brayton cycle, which includes a compressor, a turbine, and two HEXs between the HRs and WF. This part has isobaric heat absorption and heat release processes involving the temperature drops T_3-T_2 accompanying Q_H and T_4-T_1 accompanying Q_L (denoted respectively as the processes 2→3 and 4→1 in Fig. 1). This part also undergoes two isentropic processes (denoted as processes 1→2 and 3→4 in Fig. 1). The second part includes a radiator panel that dissipates heat into space. The HEXs between the HRs and WF are assumed to be counter-current. The inlet/outlet temperatures of the heating and cooling fluids are T_{Hin}/T_{Hout} and T_{Lin}/T_{Lout} , respectively.

The constant thermal capacity rate of the WF is C_{wf} , and the thermal capacity rates of the HRs are C_H and C_L . The heat conductance of the hot and cold sides of the HEX are U_H and U_L . $U_H=K_1F_H$ and $U_L=K_2F_L$, where K is the heat transfer coefficient and F is the HEX area.

According to the properties of the WF and HEX theory, the heat flux between the HRs and WF are respectively:

$$Q_H=C_{wf}(T_3-T_2)=C_{Hmin}E_{H1}(T_{Hin}-T_2) \quad (1)$$

$$Q_L=C_{wf}(T_4-T_1)=C_{Lmin}E_{L1}(T_4-T_{Lin}) \quad (2)$$

where the E s are the effectiveness values of the two HEXs:

$$E_{H1}=\frac{1-\exp[-N_{H1}(1-C_{Hmin}/C_{Hmax})]}{1-(C_{Hmin}/C_{Hmax})\exp[-N_{H1}(1-C_{Hmin}/C_{Hmax})]} \quad (3)$$

$$E_{L1}=\frac{1-\exp[-N_{L1}(1-C_{Lmin}/C_{Lmax})]}{1-(C_{Lmin}/C_{Lmax})\exp[-N_{L1}(1-C_{Lmin}/C_{Lmax})]} \quad (4)$$

$$N_{H1}=U_H/C_{Hmin}=K_1F_H/C_{Hmin}, N_{L1}=U_L/C_{Lmin}/C_{Lmax} \quad (5)$$

$$C_{Hmax}=\max\{C_H, C_{wf}\}, C_{Hmin}=\min\{C_H, C_{wf}\} \quad (6)$$

$$C_{Lmax}=\max\{C_L, C_{wf}\}, C_{Lmin}=\min\{C_L, C_{wf}\} \quad (7)$$

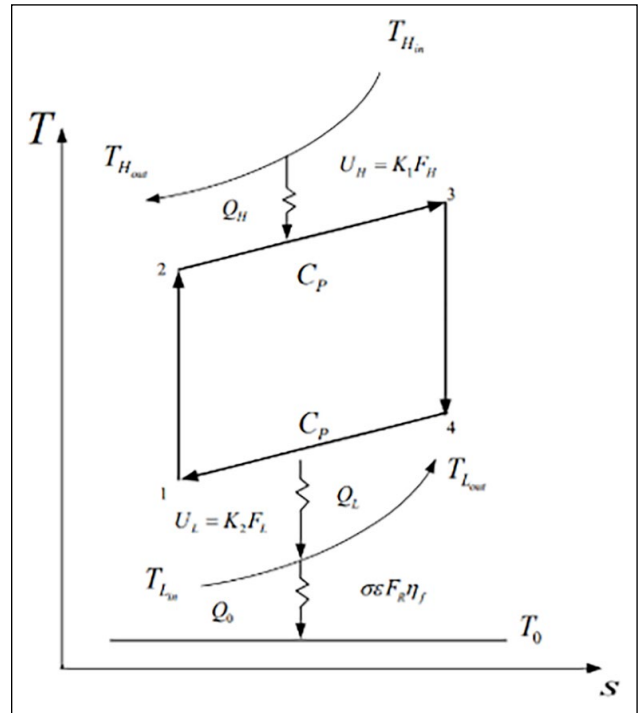


Figure 1. The T - s diagram of a variable temperature HR endoreversible closed Brayton cycle for an SPP.

HR: Heat reservoir; SPP: Space power plant.

where C_{Hmax} and C_{Hmin} are the respective maximum and minimum thermal capacity rates regarding C_{wf} and C_H , C_{Lmax} and C_{Lmin} are the respective maximum and minimum thermal capacity rates regarding C_{wf} and C_L , and N_{H1} and N_{L1} are the respective number of heat transfer units as defined based on the minimum thermal capacity.

According to the endoreversible condition, the relationship between the four temperatures of the cycle is $T_1 T_3 = T_2 T_4$. Defining the isentropic temperature ratio of the compressor as x gives:

$$x = \frac{T_2}{T_1} = \frac{T_3}{T_4} = \left(\frac{P_2}{P_1}\right)^{m/\gamma} = \pi^m \quad (8)$$

where π is the pressure ratio of the cycle, $m=(k-1)/k$, and k is the specific heat ratio.

The steady-state heat transfer from the radiator panel to the external environment is:

$$Q_0 = \sigma \epsilon F_R \eta_f (T_{Lin}^4 - T_0^4) \quad (9)$$

where η_f is fin efficiency, σ is the Boltzmann constant, T_0 is the temperature of the space environment, ϵ is emissivity, and F_R is the area of the radiator panel.

According to Ust et al. (2006), outlet temperatures T_2 and T_4 of the compressor and turbine for a conventional variable temperature HR endoreversible closed Brayton cycle model are obtained as:

$$T_2 = \frac{C_{Hmin} E_{H1} (C_{wf} - C_{Lmin} E_{L1}) T_{Hin} + x C_{wf} C_{Lmin} E_{L1} T_{Lin}}{C_{wf}^2 / C_{wf} - C_{Hmin} E_{H1} (C_{wf} - C_{Lmin} E_{L1})} \quad (10)$$

$$T_4 = \frac{x^{-1} C_{Hmin} E_{H1} C_{wf} T_{Hin} + C_{Lmin} E_{L1} (C_{wf} - C_{Hmin} E_{H1}) T_{Lin}}{C_{wf}^2 / C_{wf} - C_{Hmin} E_{H1} (C_{wf} - C_{Lmin} E_{L1})} \quad (11)$$

From the first law of thermodynamics, one can obtain:

$$Q_L = Q_0 \quad (12)$$

$$C_{L\min} E_{L1} (T_4 - T_{Lin}) = \sigma \varepsilon F_R \eta_f (T_{Lin}^4 - T_0^4) \quad (13)$$

From Eqs. 11 and 13, one gets:

$$T_4 = \frac{\sigma \varepsilon F_R \eta_f (T_{Lin}^4 - T_0^4)}{C_{L\min} E_{L1}} \quad (14)$$

$$\frac{\sigma \varepsilon F_R \eta_f (T_{Lin}^4 - T_0^4)}{(C_{L\min} E_{L1})} + T_{Lin} = \frac{x^{-1} C_{H\min} E_{H1} C_{wf} T_{Hin} + C_{L\min} E_{L1} (C_{wf} - C_{H\min} E_{H1}) T_{Lin}}{C_{wf}^2 / C_{wf} - C_{H\min} E_{H1} (C_{wf} - C_{L\min} E_{L1})} \quad (15)$$

From Eq. 15, one then gets:

$$x = \pi^m = (C_{H\min} E_{H1} C_{wf} T_{Hin}) / \{ [(C_{wf}^2 - (C_{wf} - C_{H\min} E_{H1}) (C_{wf} - C_{L\min} E_{L1})) (C_{wf} - C_{L\min} E_{L1})] \} \left[\left(\frac{\sigma \varepsilon F_R \eta_f (T_{Lin}^4 - T_0^4)}{(C_{L\min} E_{L1})} + T_{Lin} \right) - C_{L\min} E_{L1} (C_{wf} - C_{H\min} E_{H1}) T_{Lin} \right] \quad (16)$$

From Eqs. 10 and 16, one gets:

$$T_2 = \{ [(C_{wf}^2 - (C_{H\min} E_{H1} (C_{wf} - C_{L\min} E_{L1})) T_{Hin} C_{wf}^2 - (C_{wf} - C_{H\min} E_{H1})) + (C_{H\min} E_{H1} C_{wf} T_{Hin} + C_{L\min} E_{L1} (C_{wf} - C_{H\min} E_{H1}) T_{Lin}) C_{wf} C_{L\min} E_{L1} T_{Lin}] \} / \{ [(C_{wf} - C_{H\min} E_{H1}) (C_{wf} - C_{L\min} E_{L1}) (C_{wf} - C_{L\min} E_{L1}) \left(\frac{\sigma \varepsilon F_R \eta_f (T_{Lin}^4 - T_0^4)}{(C_{L\min} E_{L1})} + T_{Lin} \right)] \} \quad (17)$$

From Eqs. 1, 2, 14, and 17, one then gets:

$$Q_H = \{ [(C_{H\min} E_{H1} T_{Hin} - ((C_{wf}^2 - (C_{H\min} E_{H1} (C_{wf} - C_{L\min} E_{L1})) T_{Hin} C_{wf}^2 - (C_{wf} - C_{H\min} E_{H1})) + (C_{H\min} E_{H1} C_{wf} T_{Hin} + C_{L\min} E_{L1} (C_{wf} - C_{H\min} E_{H1}) T_{Lin}) C_{wf} C_{L\min} E_{L1} T_{Lin})] \} / \{ [(C_{wf} - C_{H\min} E_{H1}) (C_{wf} - C_{L\min} E_{L1}) (C_{wf} - C_{L\min} E_{L1}) \left(\frac{\sigma \varepsilon F_R \eta_f (T_{Lin}^4 - T_0^4)}{(C_{L\min} E_{L1})} + T_{Lin} \right)] \} \quad (18)$$

$$Q_L = C_{L\min} E_{L1} \frac{\sigma \varepsilon F_R \eta_f (T_{Lin}^4 - T_0^4)}{C_{L\min} E_{L1}} \quad (19)$$

Thus, the POW and TEF of the plant are respectively:

$$P = Q_H - Q_L = \{ [(C_{H\min} E_{H1} T_{Hin} - ((C_{wf}^2 - (C_{H\min} E_{H1} (C_{wf} - C_{L\min} E_{L1})) T_{Hin} C_{wf}^2 - (C_{wf} - C_{H\min} E_{H1})) + (C_{H\min} E_{H1} C_{wf} T_{Hin} + C_{L\min} E_{L1} (C_{wf} - C_{H\min} E_{H1}) T_{Lin}) C_{wf} C_{L\min} E_{L1} T_{Lin})] \} / \{ [(C_{wf} - C_{H\min} E_{H1}) (C_{wf} - C_{L\min} E_{L1}) (C_{wf} - C_{L\min} E_{L1}) \left(\frac{\sigma \varepsilon F_R \eta_f (T_{Lin}^4 - T_0^4)}{(C_{L\min} E_{L1})} + T_{Lin} \right)] \} - (C_{L\min} E_{L1} \frac{\sigma \varepsilon F_R \eta_f (T_{Lin}^4 - T_0^4)}{C_{L\min} E_{L1}}) \quad (20)$$

$$\eta = 1 - (Q_H / Q_L) = 1 - \{ [(C_{H\min} E_{H1} T_{Hin} - ((C_{wf}^2 - (C_{H\min} E_{H1} (C_{wf} - C_{L\min} E_{L1})) T_{Hin} C_{wf}^2 - (C_{wf} - C_{H\min} E_{H1})) + (C_{H\min} E_{H1} C_{wf} T_{Hin} + C_{L\min} E_{L1} (C_{wf} - C_{H\min} E_{H1}) T_{Lin}) C_{wf} C_{L\min} E_{L1} T_{Lin})] \} / \{ [(C_{wf} - C_{H\min} E_{H1}) (C_{wf} - C_{L\min} E_{L1}) (C_{wf} - C_{L\min} E_{L1}) \left(\frac{\sigma \varepsilon F_R \eta_f (T_{Lin}^4 - T_0^4)}{(C_{L\min} E_{L1})} + T_{Lin} \right)] \} - \{ [(C_{L\min} E_{L1} \frac{\sigma \varepsilon F_R \eta_f (T_{Lin}^4 - T_0^4)}{(C_{L\min} E_{L1})})] \} \quad (21)$$

3. POWER MAXIMIZATION

3.1. Initial design

In accordance with Ust et al. (2006), Wang et al. (2021b, 2022), and Romano & Ribiero (2021), an initial design has been performed with $\sigma = 5.67 \times 10^{-11} \text{ kW}/(\text{m}^2 \cdot \text{K}^4)$, $\eta_f = 0.9$, $\varepsilon = 0.9$, $C_{wf} = 1.5 \text{ kW}/\text{K}$, $C_L = C_H = 1.2 \text{ kW}/\text{K}$, $K_1 = K_2 = 0.2 \text{ kW}/(\text{m}^2 \cdot \text{K})$, $T_{Hin} = 1150 \text{ K}$, $T_{Lin} = 400 \text{ K}$, $T_0 = 200 \text{ K}$, $F_H = 12.24 \text{ m}^2$, $F_L = 12.24 \text{ m}^2$, and $F_R = 122.4 \text{ m}^2$. The POW of the initial design is $P = 122.94$.

3.2. The maximum and double-maximum POWs

A change in the area of the HEXs will also change and, thus enabling the POW to be maximized. Assuming that the sum of the area of the three HEXs is constant:

$$F_H + F_L + F_R = F_T \quad (22)$$

and defining the three area distribution ratios as:

$$f_i = F_i / F_T \quad (i = H, L, R) \quad (23)$$

$$\sum f_i = 1, \quad 0 < f_i < 1 \quad (i = H, L, R) \quad (24)$$

one can perform the POW maximization with respect to the area ratios. The obtained maximum POW is P_{\max} .

Figure 2 reflects P versus f_H and f_L with $F_T = 153.8 \text{ m}^2$, $C_{wf} = 1.5 \text{ kW}/\text{K}$, $K_1 = K_2 = 0.2 \text{ kW}/(\text{m}^2 \cdot \text{K})$, $T_{Hin} = 1150 \text{ K}$, $T_{Lin} = 400 \text{ K}$, $C_L = C_H = 1.2 \text{ kW}/\text{K}$, and $T_0 = 200 \text{ K}$. P_{\max} (the peak of the curve in Fig. 3) is obtained with HEXs' area allocations f_H and f_L as optimization variables and the fixed F_T , with the corresponding optimal area allocations of the HEXs and radiator panel being f_{Hopt} , f_{Lopt} and f_{Ropt} , respectively. P_{\max} is 128.26 kW , with P_{\max} increasing by about 4.33% compared to the POW (P) of the initial design.

The double-maximum POW ($P_{\max,2}$) is further obtained by optimizing the inlet temperature of the cooling fluid (T_{Lin}) based on f_{Hopt} , f_{Lopt} and f_{Ropt} . Figure 3 reflects the maximum POW (P_{\max}) versus T_{Lin} . In the calculation, almost all of the parameters are the same as those for Figure 2 except T_{Lin} , which is variable. $P_{\max,2}$ (the peak of the curve in Fig. 3) is 130.65 ; with $P_{\max,2}$ increasing by about 1.86% compared to maximum POW (P_{\max}), and $P_{\max,2}$ increasing by about 6.27% compared to the POW (P) of the initial design.

Here the study will perform some parameter analyses regarding the maximum POW and double-maximum POW. Figures 4 and 5 reflect the effects of the thermal capacity rate (C_{wf}) of the WF and heat transfer coefficients of the HEXs (K_1 and K_2) on the relationship between P_{\max} and the corresponding TEF (η_{opt}), the relationship between P_{\max} and the inlet temperature of the cooling fluid (T_{Lin}), the relationship between P_{\max} and f_{Hopt} (f_{Ropt}), as well as the relationship between P_{\max} and the corresponding pressure ratio (π).

Figure 4 reflects $P_{\max} - T_{Lin}$, $P_{\max} - \eta_{opt}$, $P_{\max} - f_{Hopt}$, $P_{\max} - f_{Ropt}$ and $P_{\max} - \pi$ under different C_{wf} values. When $K_1 = K_2 = 0.2 \text{ kW}/(\text{m}^2 \cdot \text{K})$, increasing C_{wf} also increases the TEF [$(\eta_{opt}) P_{\max,2}$], radiator area allocation [$(f_{Ropt}) P_{\max,2}$], and pressure ratio [$(\pi_{opt}) P_{\max,2}$] at double-maximum POW ($P_{\max,2}$) while decreasing $P_{\max,2}$, the hot side of the HEX area allocation [$(f_{Hopt}) P_{\max,2}$], and the inlet temperature of the cooling fluid [$(T_{Lin}) P_{\max,2}$] at $P_{\max,2}$. C_{wf} values of 1.5, 2.0, and 2.5 result in respective $P_{\max,2}$ values of 130.65 kW , 126.33 kW , and 123.042

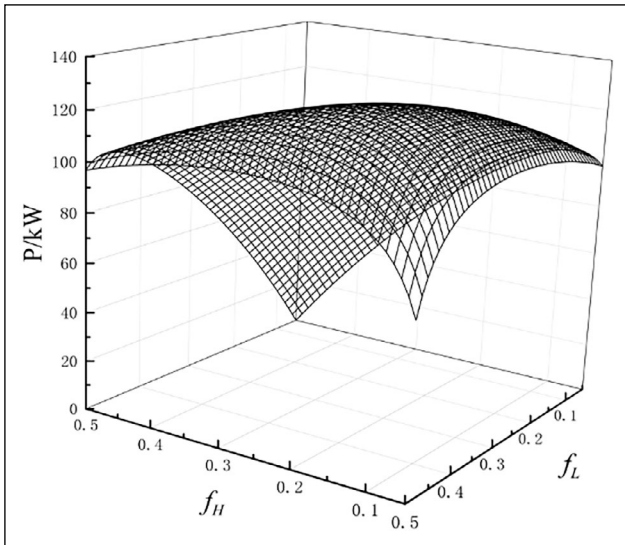


Figure 2. The relations of P versus f_H and f_L .

kW; respective $(T_{Lin}) P_{max,2}$ values of 428 K, 419 K, and 413 K; respective values of 0.468, 0.473, and 0.476, respective $(\eta_{opt}) P_{max,2}$ values of 9.10, 9.41, and 9.59; respective $(f_{Hopt}) P_{max,2}$ values of 0.171, 0.156, and 0.151; and respective $(f_{Ropt}) P_{max,2}$ values of 0.658, 0.68, and 0.698. Increasing C_{wf} from 1.5 to 2.5 decreases $P_{max,2}$ by about 5.82% and $(T_{Lin}) P_{max,2}$ by about 3.50%, increases $(\eta_{opt}) P_{max,2}$ by about 1.71%, decreases $(f_{Hopt}) P_{max,2}$ by about 11.70%, and increases $(f_{Ropt}) P_{max,2}$ by about 5.71% as well as $(\pi_{opt}) P_{max,2}$ by about 5.49%.

The optimal pressure ratio $(\pi_{opt}) P_{max,2}$ corresponding to $P_{max,2}$ should be pointed out to have one-to-one correspondence to the optimal inlet temperature of the cooling fluid $[(T_{Lin}) P_{max,2}]$; namely, only one independent variable is found between the inlet temperature of the cooling fluid (T_{Lin}) and the pressure ratio (π) .

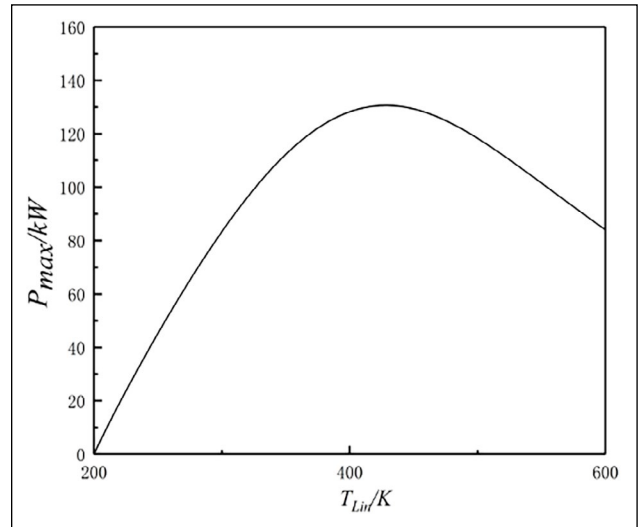


Figure 3. The relations of P_{max} versus T_{Lin} .

Figure 5 reflects the $P_{max}-T_{Lin}$, $P_{max}-\eta_{opt}$, $P_{max}-f_{Hopt}$, $P_{max}-f_{Ropt}$ and $P_{max}-\pi$ values under different $K_1=K_2$ and. When $C_{wf}=1.5$, increases to K_1 and K_2 will increase $P_{max,2}$, $(T_{Lin}) P_{max,2}$, and $(f_{Ropt}) P_{max,2}$ while decreasing $(f_{Hopt}) P_{max,2}$, and $(\eta_{opt}) P_{max,2}$. When K_1 and K_2 are 0.1, 0.2, and 0.3, $P_{max,2}$ has respective values of 111.94kW, 130.65kW, and 139.75kW; $(T_{Lin}) P_{max,2}$ has respective values of 426 K, 428 K, and 429.8 K; $(\eta_{opt}) P_{max,2}$ has respective values of 0.469, 0.468, and 0.467; $(\pi_{opt}) P_{max,2}$ has respective values of 9.15, 9.10, and 9.08; $(f_{Hopt}) P_{max,2}$ has respective values of 0.213, 0.171, and 0.147; and $(f_{Ropt}) P_{max,2}$ has respective values of 0.573, 0.658, and 0.706. Increasing K_1 and K_2 from 0.1 to 0.3 increases $P_{max,2}$ by about 24.84% and $(T_{Lin}) P_{max,2}$ by about 0.89%, decreases $(\eta_{opt}) P_{max,2}$ by about 0.426% and $(f_{Hopt}) P_{max,2}$ by about 30.99%, increases $(f_{Ropt}) P_{max,2}$ by about 23.21%, and decreases $(\pi_{opt}) P_{max,2}$ by about 0.765%.

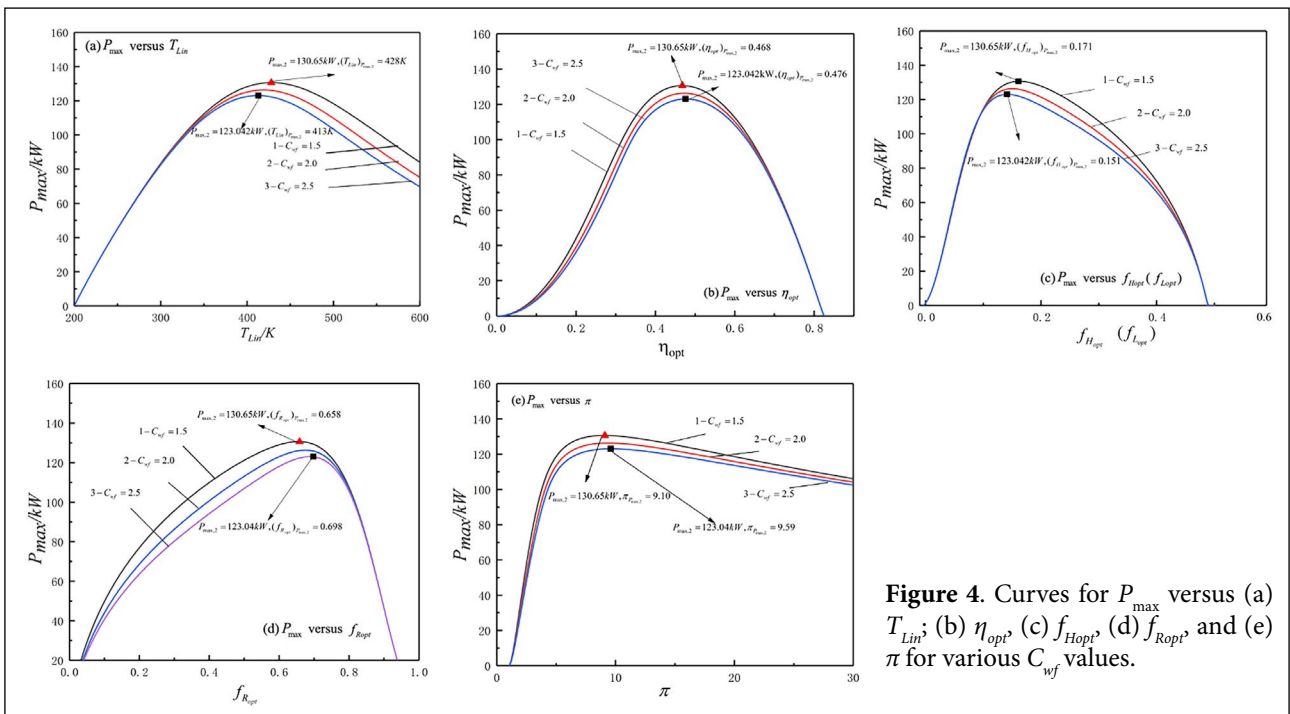


Figure 4. Curves for P_{max} versus (a) T_{Lin} , (b) η_{opt} , (c) f_{Hopt} , (d) f_{Ropt} and (e) π for various C_{wf} values.

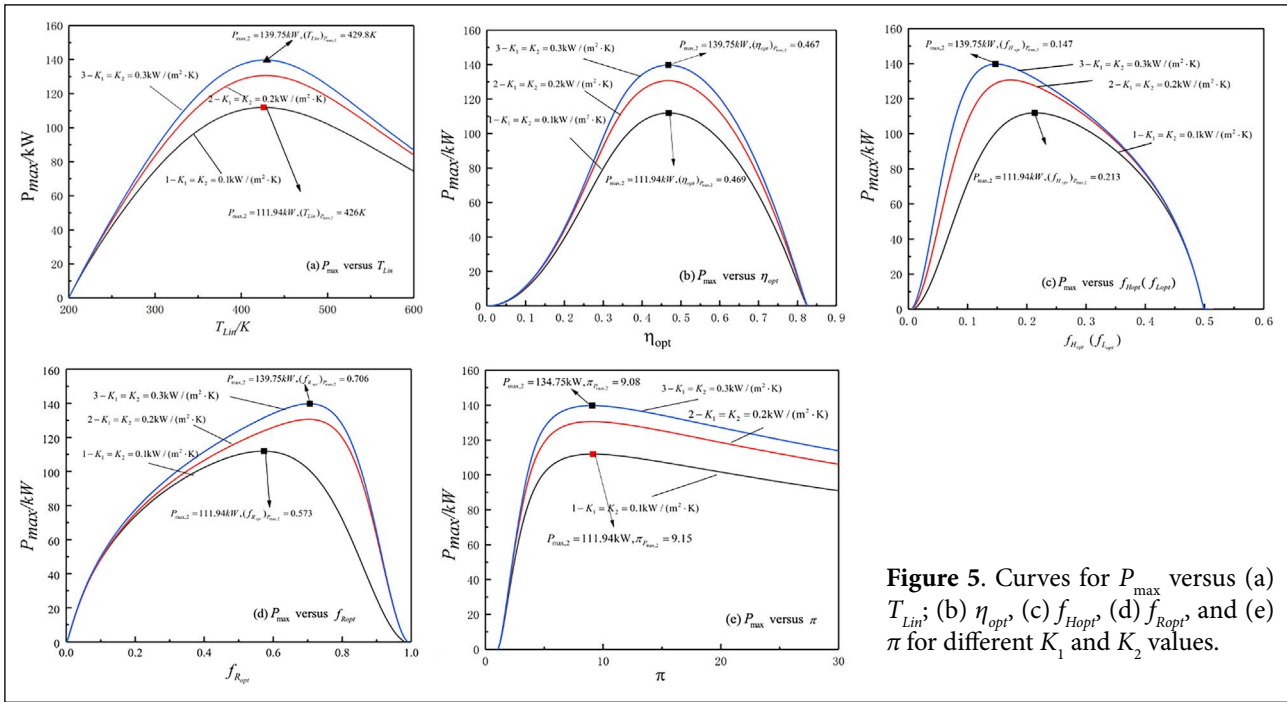


Figure 5. Curves for P_{max} versus (a) T_{Lin} ; (b) η_{opt} ; (c) f_{Hopt} ; (d) f_{Ropt} and (e) π for different K_1 and K_2 values.

3.3. The triple-maximum POW

The triple maximum POW ($P_{max,3}$) has been further obtained by optimizing the thermal capacity rate matching (C_{wf}/C_H) between the HRs and WF based on f_{Hopt} , f_{Lopt} , f_{Ropt} , and $(T_{Lin})_{P_{max,2}}$. When almost all of the parameters are the same as those for Figure 3 except for C_{wf}/C_H , which is variable, the optimization shows the triple maximum POW to be $P_{max,3} = 137.40$ kW, as shown by the peak of Curve 2 in Figure 6. $P_{max,3}$ increases by about 5.17% compared to the double-maximum POW ($P_{max,2}$), by about 7.13% compared to the maximum POW (P_{max}), and by about 11.76% compared to the POW (P) of the initial design.

Now we further study the effects of the thermal capacity ratio (C_L/C_H) of the HRs and K_1 on the triple-maximum POW ($P_{max,3}$). Figures 6 and 7 reflect $P_{max,2} - C_{wf}/C_H$ under different C_L/C_H and K_1 values, respectively. One can see that as C_{wf}/C_H increases, $P_{max,2} - C_{wf}/C_H$ reflects a stable parabolic-like change, and an optimal C_{wf}/C_H [$(C_{wf}/C_H)_{opt}$] is found for the cycle to reach triple-maximum POW ($P_{max,3}$; i.e., the peaks of the curves).

Figure 6 reflects $P_{max,2} - C_{wf}/C_H$ under different C_L/C_H . When $K_1=K_2=0.2$ kW/(m².K), increasing C_L/C_H increases both $P_{max,3}$ and $(C_{wf}/C_H)_{opt}$. C_L/C_H values of 0.6, 1.0, and 1.6 result in respective $P_{max,3}$ values of 116.57, 137.40, and 148.31 kW and corresponding $(C_{wf}/C_H)_{opt}$ values of 0.75, 1.0, and 1.23. When C_L/C_H increases from 0.6 to 1.6, $P_{max,3}$ increases by about 27.23%, while $(C_{wf}/C_H)_{opt}$ increases by about 64%.

Figure 7 reflects the $P_{max,2} - C_{wf}/C_H$ curve for different K_1 values. When $K_2=0.2$ kW/(m².K) and $C_L/C_H=1.6$, increasing K_1 results in $P_{max,3}$ increasing and $(C_{wf}/C_H)_{opt}$ decreasing. For K_1 values of 0.2, 0.3, and 0.4, $P_{max,3}$ has respective values of 148.31, 153.95, and 157.38 kW and corresponding $(C_{wf}/C_H)_{opt}$ values of 1.23, 1.20, and 1.18. When K_1 increases from 0.2 to 0.4, $P_{max,3}$ increases by about 6.12%, while $(C_{wf}/C_H)_{opt}$ decreases by about 4.07%.

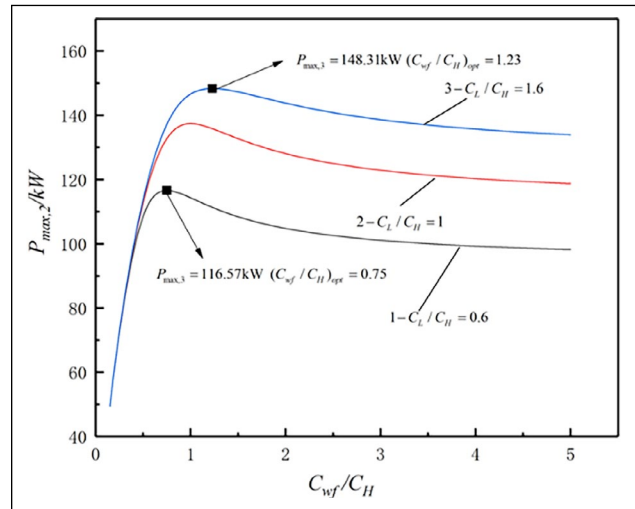


Figure 6. $P_{max,2}$ versus C_{wf}/C_H for different C_L/C_H values.

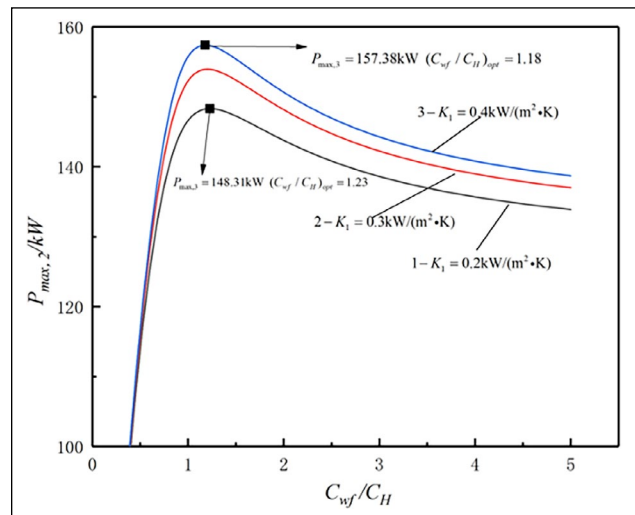


Figure 7. $P_{max,2}$ versus C_{wf}/C_H for different K_1 values.

4. CONCLUSION

Based on Ust et al. (2006), this study has established a variable temperature HR endoreversible closed Brayton cycle for an SPP and derived the relationships between POW (P) and inlet temperature of the cooling fluid in a low temperature heat sink, as well as between the TEF and inlet temperature of the cooling fluid. For a fixed total heat transfer area of two HEXs and one radiator panel, the maximum POW (P_{\max}) of the plant is obtained by optimizing the area distributions (f_{HP} , f_L , and f_R) among the two HEXs and the radiator panel; the double-maximum POW ($P_{\max,2}$) is obtained by optimizing the inlet temperature of the cooling fluid (T_{Lin}), and the triple-maximum POW ($P_{\max,3}$) is further obtained by optimizing the thermal capacity rate matching (C_{wf}/C_H) between the HRs and WF. The optimization effects are obvious. This study has researched the impacts of plant parameters on optimal performance, and the main conclusions are as follow:

1. Optimal f_{Hop} , f_{Lopt} and f_{Ropt} values exist for having the cycle reach P_{\max} . Optimal T_{Lin} and optimal f_{Hop} , f_{Lopt} and f_{Ropt} values exist for having the cycle reach $P_{\max,2}$. The curve $P_{\max,2}-C_{wf}/C_H$ reflects a stable parabolic-like change with an $(C_{wf}/C_H)_{opt}$ value that enables the cycle to reach $P_{\max,3}$.
2. When f_H and $f_L = 0.1$ and $T_{Lin} = 400$ K, the POW of the initial design plan is $P = 122.94$. When f_{HP} , f_L and f_R and T_{Lin} are optimized and $T_{Lin} = 400$ L, the maximum POW is $P_{\max} = 128.26$ kW, with P_{\max} increasing by about 4.33% compared to P . When further optimizing T_{Lin} , the double-maximum POW becomes $P_{\max,2} = 130.65$ kW, with $P_{\max,2}$ increasing by about 1.86% compared to P_{\max} and by about 6.27% compared to P . When further optimizing C_{wf}/C_H , the triple-maximum POW becomes $P_{\max,3} = 137.40$ kW, with $P_{\max,3}$ increasing by about 5.17% compared to $P_{\max,2}$, by about 7.13% compared to P_{\max} , and by about 11.76% compared to P .
3. When f_{HP} , f_L and f_R are optimized, increasing C_{wf} from 1.5 to 2.5 decreases $P_{\max,2}$ by about 5.82% and $(T_{Lin}) P_{\max,2}$ by about 3.50%, increases $(\eta_{opt}) P_{\max,2}$ by about 1.71%, decreases $(f_{Hop}) P_{\max,2}$ by about 11.70%, and increases $(f_{Ropt}) P_{\max,2}$ by about 5.71% and $(\pi_{opt}) P_{\max,2}$ by about 5.49%. Increasing K_1 and K_2 from 0.1 to 0.3 increases $P_{\max,2}$ by about 24.83% and $(T_{Lin}) P_{\max,2}$ by about 0.89%, decreases $(\eta_{opt}) P_{\max,2}$ by about 0.426% and $(f_{Hop}) P_{\max,2}$ by about 30.99%, increases $(f_{Ropt}) P_{\max,2}$ by about 23.21%, and decreases $(\eta_{opt}) P_{\max,2}$ by about 0.765%.
4. When f_{HP} , f_L , f_R , T_{Lin} and C_{wf}/C_H are optimized, increasing C_L/C_H from 0.6 to 1.6 increases $P_{\max,3}$ by about 27.23% and $(C_{wf}/C_H)_{opt}$ by about 64%. Increasing K_1 from 0.2 to 0.4 increases $P_{\max,3}$ by about 6.12% and decreases $(C_{wf}/C_H)_{opt}$ by about 4.07%.
5. Using FTT to optimize the closed Brayton cycle for an SPP has obtained the optimal area distribution and optimal inlet temperature of the cooling fluid. The optimization results provide a theoretical basis for the design of a heat exchanger structure and for the selection of its temperature in a space-based power plant. Therefore, FTT is shown to be an important tool for studying SPPs.

ACKNOWLEDGEMENT

This work has been supported by the National Natural Science Foundation of China (Project Nos. 52171317 and 51779262) and the Graduate Innovative Fund of Wuhan Institute of Technology (Project No. CX2021043). The authors wish to thank the reviewers for their careful, unbiased, and constructive suggestions, which has led to this revised manuscript.

DATA AVAILABILITY STATEMENT

The published publication includes all graphics and data collected or developed during the study.

CONFLICT OF INTEREST

The author declared no potential conflicts of interest with respect to the research, authorship, and/or publication of this article.

ETHICS

There are no ethical issues with the publication of this manuscript.

FINANCIAL DISCLOSURE

The authors declared that this study has received no financial support.

REFERENCES

- Andresen, B. (1983). *Finite-time thermodynamics*. University of Copenhagen.
- Andresen, B., & Salamon, P. (2022). Future perspectives of finite-time thermodynamics. *Entropy*, 24(5), Article 690. [CrossRef]
- Badescu, V. (2022). Maximum work rate extractable from energy fluxes. *Journal of Non-Equilibrium Thermodynamics*, 47(1), 77–93. [CrossRef]
- Bejan, A. (1996). *Entropy generation minimization*. CRC Press.
- Berry, R. S., Salamon, P., & Andresen, B. (2020). How it all began. *Entropy*, 22(8), Article 908. [CrossRef]
- Chen, L. G., & Lorenzini, G. (2022a). Comparative performance for thermoelectric refrigerators with radiative and Newtonian heat transfer laws. *Case Stud. Thermal Engineering*, 34, Article 102069. [CrossRef]
- Chen, L. G., Li, P. L., Xia, S. J., Kong, R., & Ge, Y. L. (2022b). Multi-objective optimization for membrane reactor for steam methane reforming heated by molten salt. *Scientific China: Technological Sciences*, 65(6), 1396–1414. [CrossRef]
- Chen, L. G., Meng, F. K., Ge, Y. L., Feng, H. J., & Xia, S. J. (2020a). Performance optimization of a class of combined thermoelectric heating devices. *Science China: Technological Sciences*, 63(12), 2640–2648. [CrossRef]
- Chen, L. G., Meng, F. K., Ge, Y. L., & Feng, H. J. (2021a). Performance optimization for a multielement thermoelectric refrigerator with another linear heat transfer law. *Journal of Non-Equilibrium Thermodynamics*, 46(2), 149–162. [CrossRef]

- Chen, L. G., Qi, C. Z., Ge, Y. L., & Feng, H. J. (2022a). Thermal Brownian heat engine with external and internal irreversibilities. *Energy*, 255, Article 124582. [CrossRef]
- Chen, L. G., Shi, S. S., Ge, Y. L., & Feng, H. J. (2023a). Performance of a generalized irreversible isothermal chemical pump with diffusive mass transfer law. *Energy*, 263(C), Article 125956. [CrossRef]
- Chen, L. G., Shi, S. S., Feng, H. J., & Ge, Y. L. (2023b). Ecological optimization of an endoreversible three-mass-reservoir chemical pump. *Journal of Non-Equilibrium Thermodynamics*, 48, Article 62. [CrossRef]
- Chen, L. G., Wu, C., & Sun, F. R. (1996). A generalized model of real heat engines and its performance. *Journal of the Energy Institute*, 69(481), 214–222.
- Chen, L. G., Wu, C., & Sun, F. R. (1999). Finite time thermodynamic optimization or entropy generation minimization of energy systems. *Journal of Non-Equilibrium Thermodynamics*, 24(4), 327–359. [CrossRef]
- Chen, L. G., & Xia, S. J. (2022a). Maximizing power output of endoreversible non-isothermal chemical engine via linear irreversible thermodynamics. *Energy*, 255, Article 124526. [CrossRef]
- Chen, L. G., & Xia, S. J. (2022b). Minimizing entransy dissipation for heat transfer processes with $q \propto \Delta(T^n)$ and heat leakage. *Case Studies in Thermal Engineering*, 36, 102183. [CrossRef]
- Chen, L. G., & Xia, S. J. (2022c). Heat engine cycle configurations for maximum work output with generalized models of reservoir thermal capacity and heat resistance. *Journal of Non-Equilibrium Thermodynamics*, 47(4), 329–338. [CrossRef]
- Chen, L. G., & Xia, S. J. (2022d). Maximizing power of irreversible multistage chemical engine with linear mass transfer law using HJB theory. *Energy*, 261, Article 125277. [CrossRef]
- Chen, L. G., & Xia, S. J. (2022e). Maximum work output configuration of finite potential source irreversible isothermal chemical engines with bypass mass leakage and mass resistance. *Energy Reports*, 8, 11440–11445. [CrossRef]
- Chen, L. G., & Xia, S. J. (2022f). Maximum profit output configuration of multi-reservoir resource exchange intermediary. *Entropy*, 24(10), Article 1451. [CrossRef]
- Chen, L. G., & Xia, S. J. (2023a). Power output and efficiency optimization of endoreversible non-isothermal chemical engine via Lewis analogy. *Scientific China: Technological Sciences*, 66, Article 45.
- Chen, L. G., & Xia, S. J. (2023b). Power-optimization of multistage non-isothermal chemical engine system via Onsager equations, Hamilton-Jacobi-Bellman theory and dynamic programming. *Scientific China: Technological Sciences*, 66, 841–852. [CrossRef]
- Chen, L. G., & Xia, S. J. (2023c). Maximum work configuration of finite potential source endoreversible non-isothermal chemical engines. *Journal of Non-Equilibrium Thermodynamics*, 48, 41–53. [CrossRef]
- Chen, Y. R. (2011). Maximum profit configurations of commercial engines. *Entropy*, 13(6), 1137–1151. [CrossRef]
- Curzon, F. L., & Ahlborn, B. (1975). Efficiency of a Carnot engine at maximum power output. *American Journal of Physics*, 43(1), 22–24. [CrossRef]
- de Moura, E. F., Henriques, I. B., Guilherme, B., & Ribeiro, G. B. (2022b). Thermodynamic-dynamic coupling of a Stirling engine for space exploration. *Thermal Sciences and Engineering Progress*, 32, Article 101320. [CrossRef]
- de Moura, E. F., Henriques, I. B., & Ribeiro, G. B. (2022a). Finite-time thermodynamics and exergy analysis of a Stirling engine for space power generation. *Thermal Sciences and Engineering Progress*, 27, Article 101078. [CrossRef]
- Ding, Z. M., Qiu, S. S., Chen, L. G., & Wang, W. H. (2021). Modeling and performance optimization of double-resonance electronic cooling device with three electron reservoirs. *Journal of Non-Equilibrium Thermodynamics*, 46(3), 273–289. [CrossRef]
- Ebrahimi, R. (2021). A new comparative study on performance of engine cycles under maximum thermal efficiency condition. *Energy Reports*, 7, 8858–8867. [CrossRef]
- El-Genk, M. S., & Tournier, J. M. (2009). Performance analyses of VHTR plants with direct and indirect closed Brayton cycles and different working fluids. *Progress in Nuclear Energy*, 51(3), 556–572. [CrossRef]
- Feidt, M. (2017). *Finite physical dimensions optimal thermodynamics: 1. Fundamentals*. ISTE Press and Elsevier. [CrossRef]
- Feng, H. J., Qin, W. X., Chen, L. G., Cai, C. G., Ge, Y. L., & Xia, S. J. (2020). Power output, thermal efficiency and exergy-based ecological performance optimizations of an irreversible KCS-34 coupled to variable temperature heat reservoirs. *Energy Conversation and Management*, 205, Article 112424. [CrossRef]
- Feng, H. J., Wu, Z. X., Chen, L. G., & Ge, Y. L. (2021). Constructal thermodynamic optimization for dual-pressure organic Rankine cycle in waste heat utilization system. *Energy Conversion and Management*, 227, Article 113585. [CrossRef]
- Ge, Y. L., Chen, L. G., & Feng, H. J. (2021). Ecological optimization of an irreversible diesel cycle. *The European Physical Journal Plus*, 136(2), Article 198. [CrossRef]
- Ge, Y. L., Shi, S. S., Chen, L. G., Zhang, D. F., & Feng, H. J. (2022). Power density analysis and multi-objective optimization for an irreversible dual cycle. *Journal of Non-Equilibrium Thermodynamics*, 47(3), 289–309. [CrossRef]
- Gonca, G., & Sahin, B. (2016). Thermo-ecological performance analyses and optimizations of irreversible gas cycle engines. *Applied Thermal Engineering*, 105, 566–576. [CrossRef]
- Gonca, G. (2017a). Exergetic and ecological performance analyses of a gas turbine system with two intercoolers and two re-heaters. *Energy*, 124, 579–588. [CrossRef]

- Gonca, G. (2017b). Exergetic and thermo-ecological performance analysis of a gas-mercury combined turbine system (GMCTS). *Energy Conversion and Management*, 151, 32–42. [CrossRef]
- Gonca, G. (2018). The effects of turbine design parameters on the thermo-ecologic performance of a regenerated gas turbine running with different fuel kinds. *Applied Thermal Engineering*, 137, 419–429. [CrossRef]
- Gonca, G., & Bařhan, V. (2019). Multi-criteria performance optimization and analysis of a gas-steam combined power system. *Journal of the Brazilian Society of Mechanical Sciences and Engineering*, 41(9), Article 373. [CrossRef]
- Gonca, G., & Genc, I. (2019). Thermoecology-based performance simulation of a gas-mercury-steam power generation system (GMSPGS). *Energy Conversion and Management*, 189, 91–104. [CrossRef]
- Gonca, G., & Guzel, B. (2022). Exergetic and exergo-economical analyses of a gas-steam combined cycle system. *Journal of Non-Equilibrium Thermodynamics*, 47(4), 415–431. [CrossRef]
- Ibrahim, O. M., & Bourisli, R. I. (2021). The maximum power cycle operating between a heat source and heat sink with finite heat capacities. *Journal of Non-Equilibrium Thermodynamics*, 46(4), 383–402. [CrossRef]
- Ibrahim, O. M., Klein, S. A., & Mitchell, J. W. (1991). Optimal heat power cycles for specified boundary conditions. *ASME: Journal of Engineering for Gas Turbines and Power*, 113(4), 514–521. [CrossRef]
- Jin, Q. L., Xia, S. J., & Chen, L. G. (2023). A modified recompression S-CO₂ Brayton cycle and its thermodynamic optimization. *Energy*, 263(E), Article 126015. [CrossRef]
- Li, J., & Chen, L. G. (2021). Exergoeconomic performance optimization of space thermoradiative cell. *European Physical Journal Plus*, 136(6), Article 644. [CrossRef]
- Li, J., & Chen, L. G. (2022). Optimal configuration of finite source heat engine cycle for maximum output work with complex heat transfer law. *Journal of Non-Equilibrium Thermodynamics*, 47(4), 433–441. [CrossRef]
- Li, P. L., Chen, L. G., Xia, S. J., Kong, R., & Ge, Y. L. (2022). Total entropy generation rate minimization configuration of a membrane reactor of methanol synthesis via carbon dioxide hydrogenation. *Scientific China: Technological Sciences*, 65(3), 657–678. [CrossRef]
- Lin, J., Xie, S., Jiang, C. X., Sun, Y. F., Chen, J. C., & Zhao, Y. R. (2022). Maximum power and corresponding efficiency of an irreversible blue heat engine for harnessing waste heat and salinity gradient energy. *Scientific China: Technological Sciences*, 65(3), 646–656. [CrossRef]
- Liu, H. Q., Chi, Z. R., & Zang, S. S. (2020). Optimization of a closed Brayton cycle for space power systems. *Applied Thermal Engineering*, 179, Article 115611. [CrossRef]
- Miao, X. Y., Zhang, H. C., Zhang, D., Zhang, C., & Huang, Z. (2022). Properties of nitrous oxide and helium mixtures for space nuclear recompression Brayton cycle. *Energy Reports*, 8, 2480–2489. [CrossRef]
- Muschik, W., & Hoffmann, K. H. (2020). Modeling, simulation, and reconstruction of 2-reservoir heat-to-power processes in finite-time thermodynamics. *Entropy*, 22(9), Article 997. [CrossRef]
- Park, H., & Kim, M. S. (2016). Performance analysis of sequential Carnot cycles with finite heat sources and heat sinks and its application in organic Rankine cycles. *Energy*, 99, 1–9. [CrossRef]
- Paul, R., & Hoffmann K. H. (2022). Optimizing the piston paths of Stirling cycle cryocoolers. *Journal of Non-Equilibrium Thermodynamics*, 47(2), 195–203. [CrossRef]
- Qi, C. Z., Ding, Z. M., Chen, L. G., Ge, Y. L., & Feng, H. J. (2021a). Modelling of irreversible two-stage combined thermal Brownian refrigerators and their optimal performance. *Journal of Non-Equilibrium Thermodynamics*, 46(2), 175–189. [CrossRef]
- Qi, C. Z., Chen, L. G., Ding, Z. M., Ge, Y. L., & Feng, H. J. (2021b). A generalized irreversible thermal Brownian motor cycle and its optimal performance. *European Physical Journal Plus*, 136(11), Article 1120. [CrossRef]
- Qi, C. Z., Chen, L. G., Ge, Y. L., & Feng, H. J. (2022a). Heat transfer effect on the performance of thermal Brownian refrigerator. *European Physical Journal Plus*, 137(3), Article 349. [CrossRef]
- Qi, C. Z., Chen, L. G., Ge, Y. L., Yang, W. H., & Feng, H. J. (2022b). Thermal Brownian heat pump with external and internal irreversibilities. *European Physical Journal Plus*, 137(9), Article 1079. [CrossRef]
- Qiu, S. S., Ding, Z. M., Chen, L. G., & Ge, Y. L. (2021a). Performance optimization of three-terminal energy selective electron generators. *Scientific China: Technical Sciences*, 64(8), 1641–1652. [CrossRef]
- Qiu, S. S., Ding, Z. M., Chen, L. G., & Ge, Y. L. (2021b). Performance optimization of thermionic refrigerators based on van der Waals heterostructures. *Scientific China: Technological Sciences*, 64(5), 1007–1016. [CrossRef]
- Qiu, X. F., Chen, L. G., Ge, Y. L., & Shi, S. S. (2022). Efficient power characteristic analyses and multi-objective optimization for an irreversible simple closed gas turbine cycle. *Entropy*, 24(11), Article 1531. [CrossRef]
- Romano, L. F. R., & Ribeiro, G. B. (2021). Optimization of a heat pipe-radiator assembly coupled to a recuperated closed Brayton cycle for compact space power plants. *Applied Thermodynamic Engineering*, 196, Article 117355. [CrossRef]
- Toro, C., & Lior, N. (2017). Analysis and comparison of solar-driven Stirling, Brayton and Rankine cycles for space power generation. *Energy*, 120, 549–564. [CrossRef]
- Ust, Y., Sogut, O. S., Sahin, B., & Durmayaz, A. (2006). Ecological coefficient of performance (ECOP) optimization for an irreversible Brayton heat

- engine with variable-temperature thermal reservoirs. *Journal of the Energy Institute*, 79(1), 47–52. [\[CrossRef\]](#)
- Valencia-Ortega, G., Levario-Medina, S., & Barranco-Jiménez, M. A. (2021). The role of internal irreversibilities in the performance and stability of power plant models working at maximum e-ecological function. *Journal of Non-Equilibrium Thermodynamics*, 46(4), 413–429. [\[CrossRef\]](#)
- Wang, C. L., Zhang, R., Guo, K. L., Zhang, D. L., Tian, W. X., Qiu, S. Z., & Su, G. H. (2021a). Dynamic simulation of a space gas-cooled reactor power system with a closed Brayton cycle. *Energy*, 15(4), 916–929. [\[CrossRef\]](#)
- Wang, T., Chen, L. G., Liu, P., Ge, Y. L., & Feng, H. J. (2022). Performance analysis and optimization of an irreversible Carnot heat engine cycle for space power plant. *Energy Reports*, 8, 6593–6601. [\[CrossRef\]](#)
- Wang, T., Ge, Y. L., Chen, L. G., Feng, H. J., & Yu, J. Y. (2021b). Optimal heat exchanger area distribution and low-temperature heat sink temperature for power optimization of an endoreversible space Carnot cycle. *Entropy*, 23(10), Article 1285. [\[CrossRef\]](#)
- Wu, H., Ge, Y. L., Chen, L. G., & Feng, H. J. (2021). Power, efficiency, ecological function and ecological coefficient of performance optimizations of an irreversible Diesel cycle based on finite piston speed. *Energy*, 216, Article 119235. [\[CrossRef\]](#)
- Wu, Z. X., Feng, H. J., Chen, L. G., Tang, W., Shi, J. C., & Ge, Y. L. (2020). Constructal thermodynamic optimization for ocean thermal energy conversion system with dual-pressure organic Rankine cycle. *Energy Conversion and Management*, 210(12), Article 112727. [\[CrossRef\]](#)
- Wu, Z. X., Chen, L. G., Feng, H. J., & Ge, Y. L. (2021). Constructal thermodynamic optimization for a novel Kalina-organic Rankine combined cycle to utilize waste heat. *Energy Reports*, 7, 6095–6106. [\[CrossRef\]](#)
- Xu, H. R., Chen, L. G., Ge, Y. L., & Feng, H. J. (2022). Multi-objective optimization of Stirling heat engine with various heat transfer and mechanical losses. *Energy*, 256, Article 124699. [\[CrossRef\]](#)
- Zhang, H. C., Liu, X. T., Liu, J., & Li, Z. E. (2021). Characteristics and optimization of SCO₂ Brayton cycle system for power sodium-cooled fast reactor on Mars. *Thermal Science*, 25(6B), 4659–4666. [\[CrossRef\]](#)
- Zhang, X., Yang, G. F., Yan, M. Q., Ang, L. K., Ang, Y. S., & Chen, J. C. (2021). Design of an all-day electrical power generator based on thermoradiative devices. *Science China: Technological Sciences*, 64(10), 2166–2173. [\[CrossRef\]](#)



Research Article

Low-computational adaptive MPC algorithmization strategy for overshoots and undershoots in instantaneous water heater stability

Ismael EHTIWESH*

Department of Mechanical Engineering, Sabratha University, Faculty of Engineering, Sabratha, Libya

ARTICLE INFO

Article history

Received: April 3, 2023

Revised: May 9, 2023

Accepted: May 13, 2023

Key words:

Adaptive function; low-computational microcontroller; predictive control; tankless hot-water stability; time delay

ABSTRACT

Tankless gas hot water users' perceived comfort is severely affected by sudden changes deviating from the desired temperature. Water temperature instability due to overshoots and undershoots is the most common issue that appears mainly due to sudden changes in users' water flow demands and response delays inherent to the heating system. Classical controllers for heat cells have difficulties responding to temperature instability in a timely manner because they lack the capacity to anticipate the effects of sudden variations in water flow rate. Previous studies have reported the model predictive controller (MPC) with adaptive function strategy to provide the best response for stabilizing temperature, and its performance is a result of the predictive nature that allows for anticipating and correcting the negative effects on temperature from sudden flow rate variations. The present study aims to employ this strategy to a low-computational algorithm that can be embedded in low-cost hardware with limited computational and memory resources. The study's motivation is to fill the space manufacturers have left in this regard by implementing low-cost optimal-performance microcontrollers for water heaters. The algorithm results show good agreement for the responses in temperature stabilization with experimental data.

Cite this article as: Ehtiwesh I. Low-computational adaptive MPC algorithmization strategy for overshoots and undershoots in instantaneous water heater stability. *Seatific* 2023;3:1:19–24.

1. INTRODUCTION

The use of hot water contributes to about 40% of the energy consumed in residential dwellings (Bourke et al., 2014) and is responsible for an important percentage of domestic energy consumption. Instantaneous gas heating systems are widely used for their advantages of not needing a reservoir and competitive use/consumption ratio. Tankless gas water heaters (TGWHs) have the highest sales and have become an efficient means of heating water with low carbon emissions (Bourke et al., 2014). Their advantages compared to storage heaters are their smaller size, continuous hot water flow, and longer estimated useful life (Yuill et al., 2010). However, they require more power to provide the proper flow capacity, which makes their control quite complex. Furthermore, users'

perceived comfort is severely affected by sudden changes in water temperature deviating from the desired temperature (Costa et al., 2016). Hot water temperature instability due to overshoots and undershoots is generally the most common drawback and mainly results from sudden changes in water flow and response delays inherent to the hot water device's inability to make predictions using classical controllers (Costa et al., 2016). Figure 1 demonstrates the temperature overshoots and undershoots of a 58kW nominal power TGWH with respect to sudden changes in the water flowrate. In particular, this figure uses real data from an experimental laboratory test performed by the manufacturer with the use of a feed-forward proportional–integral–derivative (FFPID) controller for stabilizing the outlet hot water temperature at 60°C. Classical controllers rely on current and previous

*Corresponding author.

*E-mail address: ismael.ehtiwesh@sabu.edu.ly



measurements to regulate the system (Ehtiwesh & Durović, 2009). However, temperature overshoots and undershoots are neither acceptable nor comfortable for users regarding unpredictable changes in the hot water flow rate and have become a safety issue in extreme scenarios.

Henze et al. (2009) addressed the development of a strategy aimed at water temperature control in tankless hot water devices. Their strategy uses a model-based predictive controller to reduce outlet temperature errors. A dynamic heat transfer model for an electric tank water heater was implemented within the predictive controller of the model. The controller was connected to a physical tank water heater prototype and showed effective control of the output temperature. An artificial neural network (ANN) controller was embedded into a low profile microcontroller for a commercial electric instantaneous water heater and resulted in a lower temperature peaks and recovery times compared to the classic PID controller (Laurencio-Molina and Salazar-Garcia 2018). Takács et al.'s (2016) study showed the embedment of a model with predictive controller feedback laws into Python applications and developed a code-generation module for MATLAB's Multi-Parametric Toolbox. The study reported that the Python algorithm can be encoded within just a couple of lines in the MATLAB environment. Wang et al. (2011) proposed a few controller schemes for improving the outlet temperature stabilization of TGWH systems with a fuzzy control system intended as a black box gain scheduler regarding the parameters of a PID controller. Haissig and Woessner (2000) studied an adaptive fuzzy control code that would adapt to changing conditions such as water flow rate and inlet water temperature and automatically adjust the feed-forward curves of the gas valve control. Xu et al. (2008) studied a dynamic neuro-fuzzy control system as a controller in gas water heaters. The controller comprises a fuzzy logic controller in the feedback configuration and two dynamic neural networks in the forward path. Ehtiwesh et al.'s (2021) previous study developed a classical controller (i.e., FFPID) and model predictive controller (MPC) for controlling TGWH systems. The classic design of MPC controllers is more complicated due to the behavior of the dominant nonlinear dynamics, which can lead to performance drops (Aliskan 2018). An adaptive predictive control strategy that provides a new linear model for each time interval under dynamic operating conditions has also been implemented. Adaptive MPCs make more accurate predictions for the next time interval in contrast to classic MPCs that employ a fixed internal model. However, TGWH manufacturers are open to implementing new controllers within low-cost microcontrollers possessing limited computational abilities and memory resources. Therefore, the present study aims to address the strategy of employing a low computational code that can be embedded in low-cost hardware following the developed adaptive MPC strategy.

2. MODELING

The developed model (Ehtiwesh et al., 2021) is based on a real residential and commercial tankless water heater: the Hydro

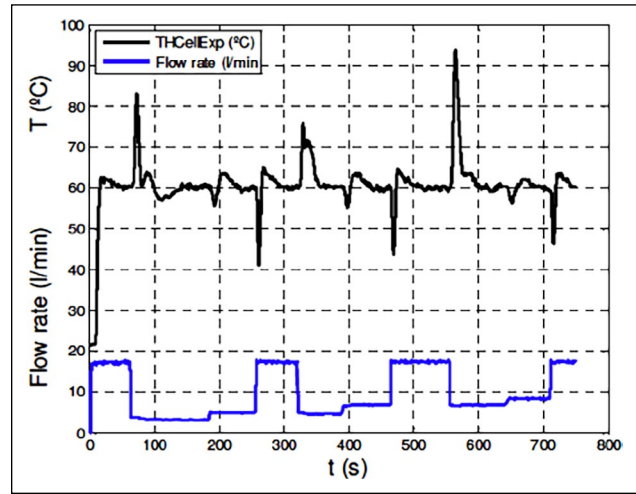


Figure 1. Experimental data of a 58kW TGWHs heat cell (Costa et al., 2016).

TGWH: Tankless gas water heater.

4600 F WTD10-4KME 23 JU, a non-condensing model rated at 22kW of thermal power and a thermal efficiency of 0.86. The system incorporates several sensors such as a carbon monoxide detector, type K thermocouples and RTD Pt100 temperature probes, a pressure sensor, and a water flow meter that enables measuring of the variables utilized in the feedback loop of the control systems. The heat cell contains a gas combustion burner and heat exchanger to heat up the water using water condensation in the flue gases. The system is a semi-empirical nonlinear model with the following energy balance equation regarding the distributed parameter model:

$$C \frac{dT}{dt} = \dot{Q} + \dot{m} c_{p,w} (T_{in} - T) \quad (1)$$

where C is the thermal capacitance defined as a coupling constant based on the energy conservation law:

$$C = (m_w c_{p,w} + m_m c_{p,m}) \quad (2)$$

\dot{Q} is the thermal power utilized in the heat cell, T is the heat cell temperature, \dot{m} is the mass flow rate ($\rho \dot{V}$), \dot{V} is the volumetric flowrate, m_w is mass, and c_p is the heat capacity ρ is water density. With this simplification, Eq. 1 can be rewritten as follows:

$$\frac{dT}{dt} = (\dot{Q} + \rho \dot{V} c_{p,w} (T_{in} - T)) / (m_w c_{p,w} + m_m c_{p,m}) \quad (3)$$

The model inputs are the thermal power (controller output) and the disturbance in the water flowrate, with the produced water temperature being the model output. The delay associated with thermal power delivery is considered to be a constant input time delay. The outlet delay varies with time based on the velocity of the water and the pipe section as presented in Eq. 4, where r_i is the orifice radius and L_i is circuit length inside the heat exchanger. Implicit dead-time compensation is utilized to employ the time delay, which varies with the flowrate as:

$$t_{delay} = \pi r_i^2 L_i / \dot{V} \quad (4)$$

2.1. Case studies

Water temperature instability from overshoots and undershoots is the most common disadvantage of TGWHs

and mainly occur due to sudden changes in users' water flow demand and the response delays inherent to the heating system. Classical controllers for heat cells have difficulties responding to temperature instability in a timely manner because they lack the ability to anticipate the effects of sudden variations in the water flow rate. Ehtiwesh et al.'s (2021) previous study carried out a comparative analysis of model-based predictive controls with and without adaptive function and classical controllers (i.e., FFPIDs) with regard to TGWH controllers. Model predictive control (MPC) is a feedback control scheme that relies on a model, an optimization solver, a receding horizon control, and optimization of a quadratic programming (QP) problem (Li et al., 2015). The future outputs of a decided horizon (prediction horizon) are predicted at each instant. These predicted outputs depend on the preceding output and input and on future control signals. The linear quadratic function is employed as a controller performance criterion in order to obtain a smooth and rapid response with minimal error and limited strain on operation. The quadratic programming problem optimizes the objective (i.e., cost function) as a nonnegative measure. The weights are adjusted to tune the controller, and the constraints are the physical bounds on the manipulated variables (MVs) and the model output parameters, and a discrete linear time-invariant (LTI) state space model is used to predict the response within the prediction horizon. The parameter estimation and subsequent validation are performed with an associated optimization platform using a discrete state space model. The undisclosed parameters have been identified using the experimental virtual test (Quintã et al., 2022). In addition, by reason of the dominant nonlinear dynamics in TGWH behavior, an adaptive predictive control strategy has also been studied (Ehtiwesh et al., 2021). The adaptive strategy provides a novel linear model at each time step regarding changes in dynamic operating conditions. Therefore, adaptive MPC offers more accurate predictions for the new time step. Altogether, the adaptive function resizes and updates the state space system of the model's parts according to flow rate changes and integrates time delays, which are absorbed as discrete states. The adaptive MPC presents superior performance regarding temperature stability in the event of sudden water flow variations.

2.2. Algorithm approach

Undoubtedly, the adaptive MPC strategy outputs the best behavior compared to the other aforementioned strategies that have been studied. Notwithstanding, TGWH manufacturers demand these controller strategies be implementable in low-cost microcontrollers with limited computational and memory resources. Therefore, the present study aims to address the potential for developing a low computational code that can be embedded into low-cost hardware based on the developed state-of-the-art adaptive MPC. The algorithm has been encoded without using pre-made functions and toolboxes in order to be easily encoded within any compiler, with Python possessing the embedded computational capability in minimal hardware devices based on device limitations. Embedding provides

applications with the capability to perform some of the functionality, Python more so than Matlab, C, or C++. This can be utilized for many goals, such as allowing users to tailor the application to their requirements by creating certain scripts within Python. The algorithm encompasses two main parts: the first aims to create the plant model in which the mathematical model is defined, linearized, and discretized and to define the parameters, with uncertain parameters being defined explicitly. The second part involves configuring the MPC controller, which encompasses the following three steps including the adaptive function:

1. Measure values,
2. Solve the constrained optimization problem, and
3. Update the states and the controller output.

The first step (i.e., measure values) calls for the ordinary subroutine to use the information obtained by the plant model to define the values being measured. Three values are required: 1) current time (t_0), which is calculated as a function of the sample time (T_s) and the current iteration; 2) the manipulated variable (u_0), which is the vector containing the predicted thermal power in the previous iteration (i.e., system input) where the new vector will be an initial state in the optimization problem; and 3) the system response (x_0), which is the current state of the system (i.e., outlet temperature). In addition, the TGWH plant needs further information to simulate real dynamics, such as:

- i. *Flow rate.* The differential equation used in the MPC model for calculating the future thermal power is based on the flow rate. The current flow rate value is read by the differential equation and adapts its dynamics like the real system.
- ii. *Delays.* Input and output delays are simulated using the variables' input delay and predicted values.

Due to this study's aim of embedding an MPC controller into low-computational microcontrollers, ensuring a linear model is a preferred strategy. Therefore, the study considers approximating the nonlinear functions in the proximity of the steady state operating point using a first-order Taylor series expansion that neglects the terms after the first partial derivatives. Eq. 3 is linearized around the operation point, namely, (Q_0, \dot{V}_0, dT_0) and converted to a state-space representation (Eq. 5). The inputs are the power (manipulated variable) and the flow rate (measured disturbance), with the temperature deviation ($dT=T-T_{in}$) being the output.

$$\dot{x} = \begin{bmatrix} -\frac{\rho c_{p,w} \dot{V}_0}{c} \\ \frac{1}{c} - \frac{\rho c_{p,w} dT_0}{c} \end{bmatrix} \begin{bmatrix} u_1 \\ u_2 \end{bmatrix}, y=x \quad (5)$$

The constrained optimization problem (Step 2) is solved using the MPC model, where the cost function is the quadratic error between the reference signal (50°C) and the MPC response using the constrained power inputs. The constraints over the action control are that the input power is limited from 0 to 1 (1 implying 100%). The solver calculates the coming sequence of manipulated variables via the control horizon, and the first value of the sequence is directed to the actuator for the following step. During the following time

step, the state values are recalculated and advanced based on sensory information and applied manipulated variables. Optimization is repeated to estimate the optimal future sequence of the manipulated variables using the prediction horizon. The final step aims to prove the predicted input and uses the optimization function “fmincon”, which is an inbuilt function for solving optimization problems by defining the minimum of a constrained nonlinear multivariable function. The function toolbox defined as a nonlinear programming solver (Eq. 6), realizes the minimum of a specified problem (MathWorks, 2021) as:

$$\min_x f(x) \text{ subject to} \quad (6)$$

$$C(x) \leq 0, \text{ ceq}(x)=0, A x \leq b, Aeq x = beq, lb \leq x \leq ub$$

where b and beq are null initializing vectors, A and Aeq are null initializing matrices, $C(x)$ and $ceq(x)$ are functions that return vectors, $f(x)$ is a cost function that returns a scalar, lb and ub are the lower and upper limit constraints vectors whose values are narrowed by the function, and $f(x)$, $C(x)$, and $ceq(x)$ are nonlinear functions. The final step also aims to update the states and the controller's output alongside the incoming iterations in order to prove the predicted inputs by including the system delays. The adaptive function resizes and updates the state space system of the model elements according to the flow rate changes and integrates the time delays that have been absorbed as discrete states. The time delay is calculated using Eq. 4 and absorbed in the discretization LTI state-space model by replacing time delays with poles at the phase shift ($z=0$) and a delay of the sampling period using the same sampling poles at $z=0$. The capability to keep track of delays makes the state space the best suited one for the model and for analyzing the delay effects in control systems. Assuming that the model is described by the subsequent uncertain discrete time-linear system with dead-time:

$$x(k+1) = A x(k) + B u(k-d) + w(k), y(k) = C x(k) \quad (7)$$

where $x(k) \in \mathbb{R}^n$ is the current state, $u(k) \in \mathbb{R}^m$ is the current control input, $w(k) \in \mathbb{R}^n$ is a bounded vector of disturbance, $y(k) \in \mathbb{R}^p$ is a linear combination of the states that identifies the desired output, k denotes the current sampling instant and d represents the nominal dead-time. Mostly, for simple cases, the time invariant linear systems without disturbances ($w(k)=0$) and dead-time ($d=0$) (Santos et al. 2012), an augmented used model is presented in (Astrom and Wittenmark 1997), incorporating the dead-time effect such as a dead-beat dynamics to achieve a “dead-time free” using implicit dead-time compensation as:

$$\Gamma(k+1) = A_\Gamma \Gamma(k) + B_\Gamma u(k), y(k) = C_\Gamma \Gamma(k) \quad (8)$$

With

$$\Gamma(k) = (x(k)' \ u(k-d)' \ u(k-d+1)' \ \dots \ u(k-2)' \ u(k-1)')';$$

$$A_\Gamma = \begin{bmatrix} A & B & 0 & 0 & \dots & 0 \\ 0 & 0 & I & 0 & \dots & 0 \\ 0 & 0 & 0 & I & \dots & 0 \\ \vdots & \vdots & \vdots & \vdots & \ddots & \vdots \\ 0 & 0 & 0 & 0 & \dots & I \\ 0 & 0 & 0 & 0 & \dots & 0 \end{bmatrix}, \quad B_\Gamma = \begin{bmatrix} 0 \\ 0 \\ \vdots \\ 0 \\ I \end{bmatrix}, \quad C'_\Gamma = \begin{bmatrix} C' \\ 0 \\ 0 \\ \vdots \\ 0 \\ 0 \end{bmatrix}$$

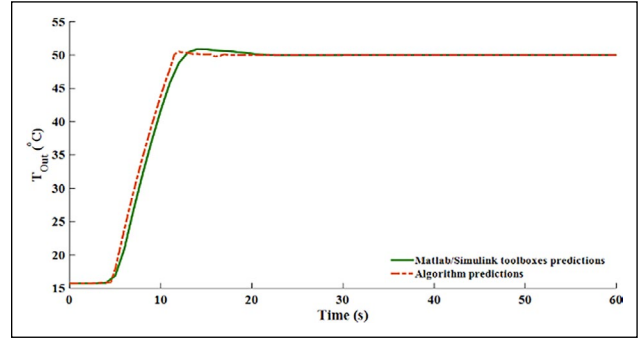


Figure 2. Comparison of the algorithm and MATLAB model predictions at a constant flow rate (10L/m).

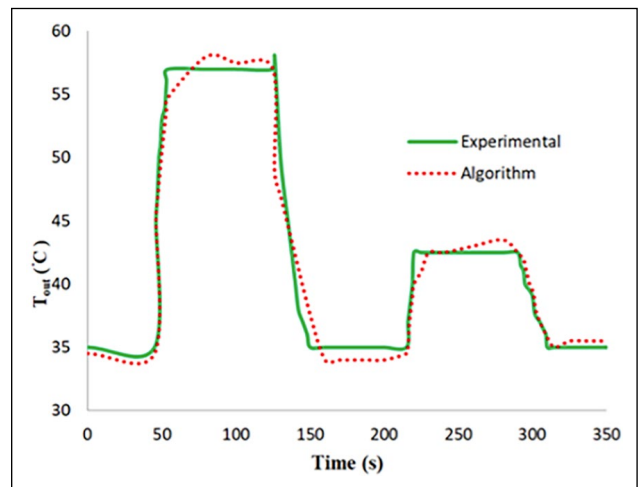


Figure 3. Experimental and algorithm predictions (water temperature) for a sequence of thermal.

The strategy is to store the past control actions in $\Gamma(k)$ $\mathbb{R}^{n+d.m}$ until the time they can actually be considered. Therefore, $\Gamma(k+1)$ depends only on $\Gamma(k)$ and $u(k)$ being able to directly describe the stabilizing elements.

3. RESULTS

The algorithm predictions have been validated using the results from the model developed in Ehtiwesh et al.'s (2021) previous study. The comparison has been implemented at the linearized flow rate of 10 L/m and sample time of 1 sec. The predictions are in extremely close agreement (Fig. 2).

Figure 3 presents a comparison between the experimental results Quinta et al. (2022) presented and the algorithm predictions of the experiment carried out for open-loop tests at constant flowrate with a sequence of fast changes in the applied thermal power (32%, 50%, and 100%). The predictions are in a good agreement, with the steady-state values being essentially coincident, despite small differences being observed during the transient segments. Figure 4 shows the overshoots and undershoots in temperature stability that appear between the 40s-60s mark in the event of sudden variations in water flow around the 34s mark, with a total simulation time of 100s. The flow rate varies sharply from 10 to 3 L/min, and the water temperature causes negligible overshoots and undershoots. Figure 5

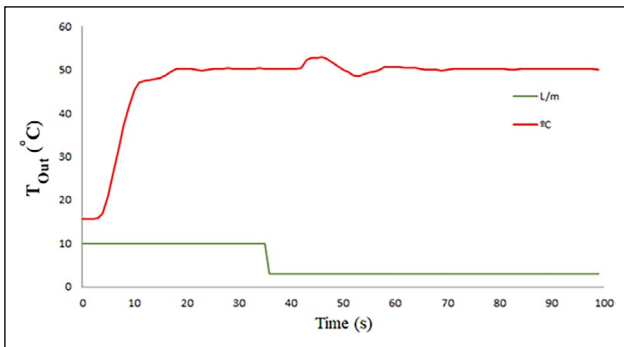


Figure 4. The algorithm predictions for a cold start at $T_s=250\text{ms}$.

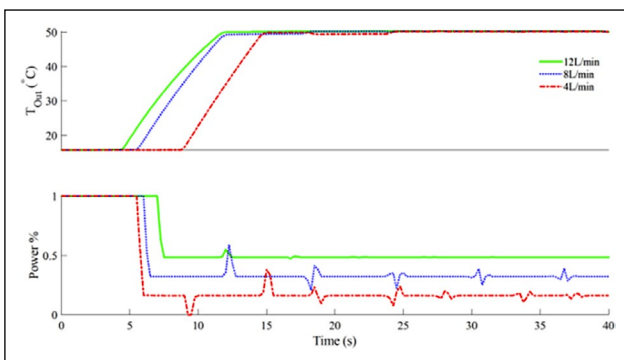


Figure 5. The algorithm predictions for a cold start at different flow rates and $T_s=250\text{ms}$.

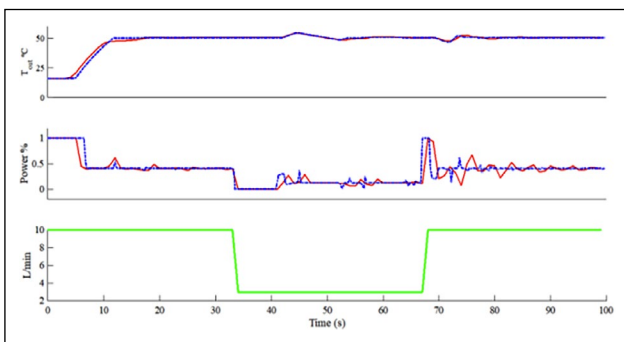


Figure 6. The algorithm predictions for a cold start at variable flow rates and different sampling intervals.

presents the simulation at various flow rates, with the manipulated variable of power being maximized in the initial stage before being switched to a steady-state value.

The power behavior shows an almost step-like transition from the upper value of the power to the steady-state value in all cases, resulting in faster temperature stabilization without overshoots or oscillations. Figure 6 presents the simulation at variable flow rates for sampling times of 250ms and 1000ms. The water flow rate changes sharply from 10L/min to 3L/min and back to 10 L/min, and the water temperature again shows negligible overshoots and undershoots.

The differences in the quality is presented in the controller signals (i.e., power). A tradeoff occurs between that frequency and T_s , with the frequency of the control signal being greater at $T_s=250\text{ms}$ compared to $T_s=1000\text{ms}$. The reason for the zero

signals between 33s-41s is due to the model having input and output delays where the internal delay is neglected. In fact, this behavior is the most difficult to overcome. The delay is approximately 10 seconds. This behavior matches the incline in the temperature output at the 42s mark.

6. CONCLUSION

Water temperature instability takes place mainly because of the nonlinearities and time-varying delays associated with TGWH systems. The MPC controller with adaptive function displayed excellent performance regarding temperature stabilization for sudden changes in flow rate. However, its employment required high computational resources and memory space and therefore needed expensive hardware. Because of this, the current study has developed a low-computational algorithm with the ability to be embedded in low-cost microcontrollers. The results of the findings demonstrate good agreement with the previously developed MATLAB/Simulink model and other experimental data. In conclusion, an adaptive model predictive control strategy can be a good solution for fulfilling the objective of reducing the time sampling to the 250ms rate that generally used by manufacturers with regard to improving water temperature instability due to overshoots and undershoots in TGWH devices.

DATA AVAILABILITY STATEMENT

The published publication includes all graphics and data collected or developed during the study.

CONFLICT OF INTEREST

The author declared no potential conflicts of interest with respect to the research, authorship, and/or publication of this article.

ETHICS

There are no ethical issues with the publication of this manuscript.

FINANCIAL DISCLOSURE

The authors declared that this study has received no financial support.

REFERENCES

- Aliskan, I. (2018). Adaptive model predictive control for wiener nonlinear systems. *Iranian Journal of Science and Technology Transactions of Electrical Engineering*, 43, 361–377. [CrossRef]
- Astrom, K. J., & Wittenmark, B. (1997). *Computer controlled systems: Theory and design* (3rd ed.). Prentice Hall.
- Bourke, G., Bansal, P., & Raine, R. (2014). Performance of gas tankless (instantaneous) water heaters under various international standards. *Applied Energy*, 131, 468–478. [CrossRef]
- Costa, V., Ferreira, J., & Guilherme, D. (2016). Modeling and simulation of tankless gas water heaters to reduce temperature overshoots and undershoots.

- 12th International Conference on Heat Transfer, Fluid Mechanics and Thermodynamics (HEFAT 2016), 1404–1409.
- Ehtiwesh, I. A. S., & Durović, Ž. (2009). Comparative analysis of different control strategies for electro-hydraulic servo systems. *World Academy of Science, Engineering and Technology*, 32(8), 906–909. [CrossRef]
- Ehtiwesh, I. A. S., Quintã, A. F., & Ferreira, J. A. F. (2021). Predictive control strategies for optimizing temperature stability in instantaneous hot water systems. *Science and Technology for the Built Environment*, 27(5), 679–690. [CrossRef]
- Haissig, C. M., & Woessner, M. (2000). Adaptive fuzzy algorithm for domestic hot water temperature control of a combi-boiler. *HVAC&R Research*, 6(2), 117–134. [CrossRef]
- Henze, G. P., Yuill, D. P., & Coward, A. H. (2009). Development of a model predictive controller for tankless water heaters. *HVAC & R Research*, 15(1), 3–23. [CrossRef]
- Laurencio-Molina, J.C. & Salazar-Garcia, C., 2018. Design of an artificial neural network controller for a tankless water heater by using a low-profile embedded system. In J. L. Crespo-Mariño (Eds.), *2018 IEEE International work conference on bioinspired intelligence, IWOBI 2018 – Proceedings* (pp. 1–8). IEEE. [CrossRef]
- Li, P., Vrabie, D., Li, D., Sorin, C., Bengea, S., O'Neill, Z. D., & Mijanovic, S. (2015). Simulation and experimental demonstration of model predictive control in a building HVAC system. *Science and Technology for the Built Environment*, 21(6), 721–732. [CrossRef]
- MathWorks. (2021). fmincon function. Available from: [https://www.mathworks.com/help/optim/ug/fmincon.html#:~:text=example-,x%3Dfmincon\(fun%2Cx0%2CA%2Cb%2C,lb%2Cx%2Cub.&text=If%20x\(i\)%20is%20unbounded,ub\(i\)%3DInf](https://www.mathworks.com/help/optim/ug/fmincon.html#:~:text=example-,x%3Dfmincon(fun%2Cx0%2CA%2Cb%2C,lb%2Cx%2Cub.&text=If%20x(i)%20is%20unbounded,ub(i)%3DInf).
- Quintã, A. F., Ehtiwesh, I. A. S., Martins, N., & Ferreira, J. A. F. (2022). Gain scheduling model predictive controller design for tankless gas water heaters with time-varying delay. *Applied Thermal Engineering*, 213, Article 118669. [CrossRef]
- Quinta, A. F., Oliveira, J. D., Ferreira, J. A. F., Costa, V. A. F., & Martins, N. (2022). Virtual test bench for the design of control strategies for water heaters. *Journal of Thermal Science and Engineering Applications*, 14(5), 1–11. [CrossRef]
- Santos, T. L. M., Limon, D., Normey-Rico, J. E., & Alamo, T. (2012). On the explicit dead-time compensation for robust model predictive control. *Journal of Process Control*, 22(1), 236–246. [CrossRef]
- Takács, B., Števek, J., Valo, R., & Kvasnica, M. (2016). Python code generation for explicit MPC in MPT. In: *2016 European control conference (ECC)* (pp. 1328–1333). IEEE. [CrossRef]
- Wang, L., Zang, H., & Ning, Y. (2011). The gas water heater control system design based on fuzzy control. *2011 International conference on electric information and control engineering, ICEICE 2011 - Proceedings* (pp. 840–843). IEEE. [CrossRef]
- Xu, K., Qiu, X., Li, X., & Xu, Y. (2008). A dynamic neuro-fuzzy controller for gas-fired water heater. In M. Guo (Ed.), *Proceedings - 4th International Conference on Natural Computation* (pp. 240–244). IEEE. [CrossRef]
- Yuill, D. P., Coward, A. H., & Henze, G. P. (2010). Performance comparison of control methods for tankless water heaters. *HVAC & R Research*, 16(5), 677–690. [CrossRef]



Research Article

Thermodynamic aspects of gas generator for application in military aircraft: Some considerations

Bhupesh A PARATE* 

Armament Research Development Establishment (ARDE), DRDO, Pune, India

ARTICLE INFO

Article history

Received: March 21, 2023

Revised: May 5, 2023

Accepted: May 13, 2023

Key words:

Booster; closed vessel; data acquisition; gas generator; propellant and thermodynamic analysis

ABSTRACT

The importance of this research is that it mainly describes the various interesting areas of the thermodynamic aspects of a gas generator for application in aircraft. The gas generators are widely used for both civil and military applications. Thermodynamics is the branch of science that deals with energy being transformed into work and vice versa. The demand for gas generator and its applications continuously increases in the areas of aerospace and aeronautical technologies. Gas generating device involves creation of a high temperature and pressurised combustion of gas by burning propellant in cartridge. These devices are filled with energetic materials (EMs) and used to perform a critical operation in an emergency under adverse conditions by releasing energy very quickly in milliseconds. A data acquisition system (DAS) is used to verify the gas generator's performance parameters such as peak pressure (P_{max}) and time to maximum pressure (TP_{max}) generated in the closed vessel (CV). A double-base propellant consisting of fuel, oxidizer and other ingredients are used as the medium for gas generation. The main goal of this research paper is to establish various relationships and determine the various thermodynamic properties of a gas generator for application in aircraft. The experimental findings from this research show the specific heat of propellant is 0.3488 cal/g/°C, the calorimetric value to equal 925 cal/g, the force constant to be 1052 J/g, the co-volume to be 0.989 m³/kmol and the flame temperature to be 2944 K. The thermodynamic analysis of a gas generator for military applications plays a significant role in the design and development phase.

Cite this article as: Parate BA. Thermodynamic aspects of gas generator for application in military aircraft: Some considerations. Seatific 2023;3:1:25–32.

1. INTRODUCTION

Thermodynamics is a branch of science that pertains to certain laws of nature that are always obeyed and never observed to be violated. Thermodynamics relate to a classical and microscopic science. This study concerns to heat and work transfer, and the different energy interactions that bring out changes in the macroscopic properties of substances. These changes are observable and quantifiable. However, work and heat are path functions based on the processes that are adopted and their cumulative sum gives

a non-zero number. The operational systems based on the thermodynamic cycle are used in a gas generator by burning a propellant. The operations of the gas generator depend on the combustion rate of the propellant, its heat and energy and the amount of generated gas that can be transformed into useful work.

This paper discusses the various aspects of thermodynamics related to a gas generator. Gas generators are mainly responsible for generating gases to operate different crucial mechanical system pertaining to aircraft. Basically,

*Corresponding author.

*E-mail address: baparate@gmail.com



they are used in special applications such as seat ejection, catapults, parachute deployment, harnesses, signaling, short-term power supplies jet engine starting and launch tubes. Gas generators are designed to produce hot combustion gases and therefore have much slower burn rates by a factor of 5 to 6 and much lower combustion temperatures between 800K to 1600K. This allows these propellants to be used with un-insulated metals in applications such as launch tubes.

The novelty of this research article is how it determines the various thermodynamic properties of a gas generator when burning the propellant under the given conditions.

1.1. Defining the research problem

Gas generators are broadly used for military, space and civil applications to perform different roles such as thrusters, signaling, flares, seat ejections, cable cutting, bomb release, stage operation, flare and chaff. They are comprised of a propellant and a pyrotechnic component. The propellant works as the main source of energy for performing the various tasks after applying appropriate stimulus. Due to the propellants being ignited inside a cartridge case, an enormous amount of combusted products is generated. The propellant's behavior and thermodynamic aspects under given circumstances are very important for that particular application. The gas generator under study here is subjected to various testing and evaluation methods in the development phase. The gas generator described in this paper is used to save a life of the pilot in an emergency situation. This type of testing is performed using the gas generator to save the life of a pilot for various aircraft platforms. The thermodynamics of a gas generator involves science related to the transfer of energy and its results on the substances' physical properties. This is based on translating the observations of common experiences into thermodynamic laws and these laws preside over the principles of energy conversion.

2. METHODOLOGY

2.1. Thermodynamic cycle

As far as the gas generator is concerned, fuel in the form of a propellant is already stored in the system. No oxygen is available for the gas generator as in the case of an internal combustion (IC) engine. The pictorial representation of the gas generators pressure vs. volume and temperature vs. entropy curves are illustrated in Figures 1 and 2 respectively (Shekar 2018). However, were one to consider the gas generator as an internal combustion (IC) engine, the process involves no intake stage. This is shown by the dotted line 1-2 in the figures. As the propellant is ignited, heat starts being added and equilibrium in pressure is attained. The heat addition is assumed to occur at a constant pressure and is shown by the line 2-3 in the figures. In many cases, the heat addition can occur at varying pressures. The combustion increases pressure initially and this transient phase can be treated as a compression stroke. The process is not isentropic and can not be represented properly by a single

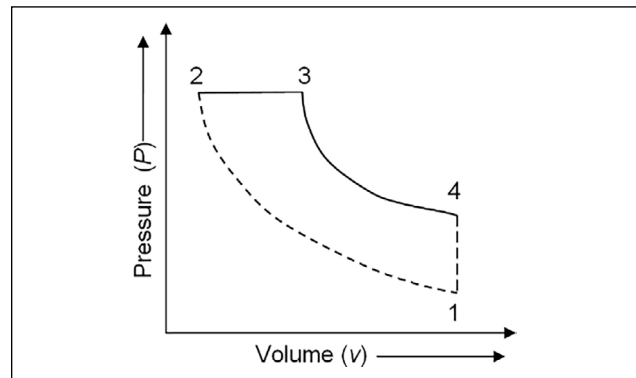


Figure 1. Pressure vs. volume.

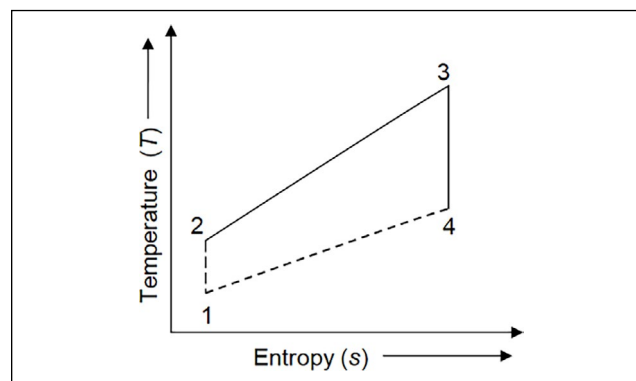


Figure 2. Temperature vs. entropy.

thermodynamic plane. This is shown as expansion stroke by the line 3-4 in the figures. However, the rise in pressure and temperature in the gas generator occurs in milliseconds (ms). Simultaneously, the combustion gases are expelled as a combination of both the expansion and heat ejection stages. Thus, the gas generator has only two valid processes on the thermodynamic plane. Another significant variation is that no cycle occurs once the propellant is initiated. After the propellant is completely burned the system returns to original state.

This indicates that the gas generator operates as a single stroke regarding thermodynamic cycle as the operation has no periodicity. A continuous generation of work occurs until the propellant (fuel) is fully consumed.

The gas generator device consists of a pyrotechnic component, the propellant and a means of initiation (Cumming, 2009). Using proper means of initiation, huge volume of gases can be generated due to the rapid chemical reactions that occur from burning the propellant. The gas generator consists of different ingredients such as oxidizing and reducing agents. Subjecting the propellant to testing involves evaluating different performance parameters such as heat of combustion, combustion temperature, specific volume, propellant force and burn rate in the test vessel. This article will outline the closed vessel (CV) firing of a gas generator and determine the various thermodynamic properties (Han, 2017). Martiosyan et al. (2009) have explained the design aspects and performance of nanoenergetic gas generator.

3. THERMODYNAMIC PROPERTIES

After evaluating the gas, the various thermodynamic properties of the gas generator are then discussed as follows.

3.1. Ratio of Specific heat (γ)

The specific heat of the gaseous product of combustion is basically a measure of temperature rise for a given heat input per unit mass of a given material. The given mass of material with a high specific heat results in a low temperature rise for a constant heat input. The reverse is true for materials with a low specific heat. Alternatively, a constant mass of a material with a high specific heat requires more heat input for a given rise in temperature. The difference in specific heats between specific heat at constant pressure and specific heat at constant volume is equal to the gas constant of the gas whose ratio is expressed by the Greek letter Gamma (γ) for ideal gases. This is also called the heat capacity ratio and adiabatic index and is basically an isentropic expansion factor. Thermodynamically, it also equals enthalpy (h) and the internal energy of the ideal gas (u). The value of γ is related to the degree of freedom available in the molecule (f) and is defined as $[1+(2/f)]$. However, the value of γ is reduced by the combustion gases containing traces of fuel. The reduction is dependent on the molecular weight of the combustion gases and their relative compressibility. The value of γ is taken as 1.2 for double-base propellant. The value of γ gets lower as temperature and pressure rise.

3.2. Mass generation rate (m_g)

This represents the rate at which the propellant is converted into gaseous form by combustion. It is given by the density of the propellant multiplied by the rate of volume consumption of the propellant. The rate of volume consumption is given by the product of the burning area (A) of the propellant and its burn rate (r) which is the consumption rate of the propellant grain or of the whole propellant mass at a constant pressure (P) per unit time. The volume of a grain consumed per unit time is the product of rate of regression (r) and the burning surface area (A). The rate of mass discharge is a function of pressure with higher pressures having higher discharge rates. This is the explosive mass consumed over a given unit of time. The expression for the mass generation rate due to propellant consumption is given below:

$$m_g = dm/dt = \rho \times A \times r \quad (1)$$

Using Vieille's equation for the mass burning rate

$$\frac{dm}{dt} = p^a \times k \times p \quad (2)$$

where k is a constant that consider the values of ρ , A and α .

The burning rate (r) plays an important role in the formulation of the propellant as it indicates the propellant's functional performance. The burn rate of the propellant is calculated from small slabs. In general, the burn rate is expressed either in mm/s or cm/s based on surface area (A) and pressure (P). This is expressed by the relation $r = \beta P^\alpha$ where α =pressure index and β =burning rate coefficient.

Furthermore, this is also based on the propellant composition (fuel and oxidizer content of the propellant) and conditions prevailing inside the combustion chamber. The burn rate affects the gas pressure and gas velocity. This affects the rate of heat transfer from the hot gas into the propellant. If the initial propellant temperature is high, the burn rate also increases. The propellant having already gained the heat tends to burn faster due to the temperature gradient that drives the burning rate, the bulk temperature. Smaller the grain sizes for a particular propellant increase the total surface area per unit weight for burning. Because the propellant density is constant, decreases in grain size will increase in total surface area per unit volume. The surface area per unit volume is called the specific surface of propellant and is measured in cm^{-1} units.

3.3. Combustion heat (Q_v)

Combustion heat of substance is also known as the calorific value or the energy value. This can be defined as the amount of heat liberated when a given amount of the substance undergoes combustion. Usually, heat of combustion is considered to be a synonym of calorific value, which can be defined as the total amount of energy liberated when a given mass of a substance undergoes complete combustion in the presence of (an adequate quantity of) oxygen under standard conditions for temperature and pressure. The concept of the heat of combustion of a propellant is extremely important considering rocket, missile and power cartridge applications. The propellants used in these areas are often selected based on their calorific values (a value that denotes the heat of combustion of the fuel). The greater the heat of combustion of propellant, the greater the amount of power that can be produced from it inside combustion chamber. Combustion heat is determined as :

$$Q_v = Q_p + RT \times \Delta n \quad (3)$$

where Q_p =heat of combustion at constant pressure (kJ/mol), Q_v =heat produced at constant volume (kJ/mol), R =the gas constant (8.314 J/mol K), Δn =moles difference between reactant and products of one kg gas, and T is temperature (K).

3.4. Specific volume (v)

Specific volume is a property of materials, defined as the number of cubic meters occupied by one kilogram of a particular substance. Specific volume is determined as

$$v = 22.4 \sum n_i (g) \quad (4)$$

This is measured in (litere/kg) and $n_i(g)$ is the amount of substance for i^{th} gas products of one kg of combustion gas.

3.5. Peak pressure (P_{max})

Using the first-order approximation, the peak pressure generated inside the cartridge is obtained by assuming instantaneous propellant burning as:

$$P_{max} = \frac{m_p R T_f}{(V-b)} = \sum \frac{m_{pi} R_i T_{fi}}{(V-b_i)} \quad (5)$$

where m_p is mass of combustion product gases, P_{max} is peak pressure, R is the universal gas constant, R_i is the gas constant of i^{th} propellant product gases, T_f is adiabatic flame temperature of the i^{th} propellant, b is co-volume of the i^{th} propellant product gases, and V is volume

The value of R is 8.31343 J/mole/K

At any given instance, the m_p generated by the propellant burning relates to the grain geometry of the propellant and can be expressed as a polynomial with powers of λ and dimensionless length, which characterizes the geometry of the propellant defined as a web.

$$m_p = m_{po} \sum_j^n k_j \lambda^i \quad (6)$$

where m_{po} is the initial mass of unburned propellant

The above relation is also known as a form function. The coefficients k_j are determined according to the propellant grain geometry. At each time frame, the combustion gases inside chamber are assumed to be in thermodynamic equilibrium with the pressure related to the equation of state for non-ideal gases.

3.6. Force constant (F)

This is one of the essential parameters of the propellant related to maximum work carried out by the propellant unit mass and is part of the utilizable energy in performing the work. The work done is expressed as product of distance covered and force. This energy is much lower than the heat from the explosion. Usually an important relationship exists between the propellant mass and maximum pressure. It is called impetus or the force constant and is denoted by F .

$$F = \frac{P_{max} (V-b)}{m_p} \quad (7)$$

where F also equals T_f

The term n , is the number of moles of a gas per unit mass and is directly proportional to the gas volume (V) at standard temperature and pressure (STP). V can be substituted for n , and Q for T_f because the two are mutually proportional. In the expression

$$F = \text{Power} = T_f \times \alpha \times Q \times V \quad (8)$$

QV is known as the characteristic product of the propellant.

The closed vessel (CV) technique is generally used to determine various parameters such as co-volume and the force constant by burning the propellant at a 0.2 g/cc loading density. Maximum pressure and burning rate can be also determined. The propellant testing in a CV is more economical compared to the actual dynamic firing, as it only requires about 200 to 300 gram of propellant versus the several kilograms. Using F , the maximum energy (E) available from the propellant is estimated as

$$E = \frac{F C}{(\gamma-1)} \quad (9)$$

3.8. Thermodynamic relations

As per the first law of thermodynamics, the state of the gas in the system can be determined as (Nag, 2018)

$$Q = \Delta U + W \quad (10)$$

Here Q is the energy supplied to the system and ΔU is the change in internal energy, W is the work done by the system is expressed as:

$$W = \int F \cdot dx \quad (11)$$

The right-hand side is the dot product of the two vectors and gives a scalar quantity.

Eq. 7 can also be rewritten as:

$$W = \int F dx \quad (12)$$

Using material mechanics

$$F = P \times A \quad (13)$$

where, F is the resultant force that is expressed as the product of average pressure P acting on the cross-sectional area A of the body.

Substituting this in Eq 12, gives

$$W = \int P \times A \times dx \quad (14)$$

where dx is the length displacement which means volume can be expressed as $dv = A \times dx$. Putting this in Eq 14, gives

$$W = \int P \times dv \quad (15)$$

Here the gas compression is assumed to be adiabatic frictionless compression with no leakage. The combustion chamber possesses very little room for oxygen as it is filled with the propellant. The chamber is where the propellant combusts and has volume V_c which is given by

$$V_c = \frac{\pi d^2}{4} \quad (16)$$

According to the ideal gas law, the pressure P can be expressed as:

$$P = \frac{m_g \times R \times T}{V} \quad (17)$$

where, m_g is the mass of the gas, V is the specific volume of the gas, P is the gas pressure, R is the gas constant and T is the absolute gas temperature. Putting Eq 14 into Eq 12 gives

$$W = \int m_g \times R \times T \frac{dV}{V} \quad (18)$$

which shows that the work done by the gas on the projectile is a function of temperature and gas volume.

4. GAS GENERATOR DESCRIPTION

All safety norms for the gas generator are strictly observed while filling so as to avoid any accidental initiation. This is achieved by selecting a proper explosive train for the initiator, booster, and propellant and is established by extensive trials carried out in the field. The most important test is the sensitivity test. It is carried out for each explosive item. The order of sensitivity decreases from initiator

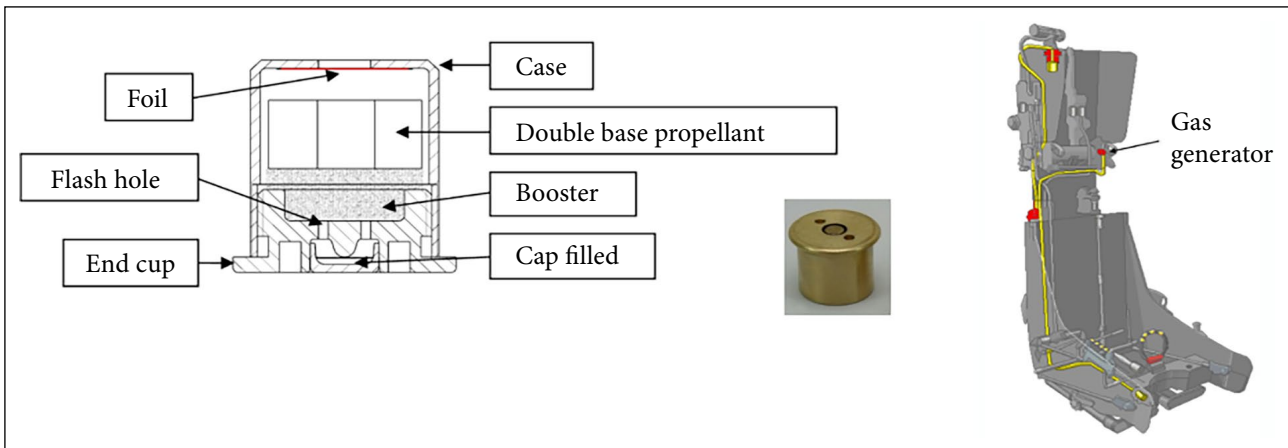


Figure 3. Schematic construction detail of the gas generator, its photo, and the seat of a fighter aircraft illustrating the location of the gas generator.

to booster and propellant. The amount of mass used in an explosive train increases from initiator, booster and propellant. The output of the explosive component increases from the initiator to booster and propellant. The initiator is the most sensitive and the propellant is the least sensitive. To bridge the gap between these two extremities, a booster is used in the explosive train. The highest order of safety is maintained while handling, storing and transporting these gas generators in this way. The cartridge is assembled with a case and foil assembly, and end cap. The cartridge case is designed so as to accommodate the propellant and booster. The necessary arrangements are made for initiating the gas generator. The case is made of brass and closed with copper foil with the other end being closed with an end cap. The foil ruptures as the high pressure and temperature of the gas act on it. The end cap is made of brass. The base of the end cap has a centrally located cap chamber at one end where the initiator is affixed. Arrangements are made for two flash holes in the cap chamber. The end cap is threaded and assembled with the cartridge case using thread sealant for proper hermetic sealing. The design aspect for the brass cartridge case using the bilinear kinematic hardening model is explained by Parate et al (2019). The schematic construction of the gas generator, its image and the seat of the fighter aircraft illustrating the location of gas generator are shown in Figure 3. The firing pin strikes the cap and generates the flash. This initiates the booster. The booster further ignites the propellant. The propellant gas so generated is used for operating the harness mechanism. This cartridge is responsible for the functioning of the harness system of the seat ejection.

5. INGREDIENTS AND MATERIALS

5.1. Double-base propellant for gas generator

This study has chosen a propellant with a tubular shape, single-axial perforation without inhabitation, and neutral type burning due to this propellant being able to burn from inside to out and outside to in so that the burning surface area remains constant. The propellant used in harness purpose must be non-hygroscopic and compatible with the casing material in which it is to be loaded. Brass has been selected for the case material as it meets the obturation requirements. Based on the above requirements, a double-base propellant has been chosen consisting of nitro-glycerine (NG) and nitro-cellulose (NC) with other ingredients added to improve the properties. The percentage of the chemical contents and physical properties of the double-base propellant as used for this application are given in Table 1. The photo of the double-base propellant is given in Figure 4.

Diethyl phthalate (DEP) has the role of an inert plasticizer (non-energetic). The carbamate works as a stabilizer so as to increase the shelf life of the propellant and reduce the degradation of the NC. The candela wax acts as wear reducing agent. The propellant's chemical content in percentage dictates the total amount of thermal energy released by burning. The gas generator using the propellant has polymeric macro-molecules with oxidizer and fuel. The double-base propellant is a homogenous mixture of NG, NC and other additives. Upon ignition this propellant produces smokeless combustible products. These combustible

Table 1. Chemical content and the physical properties of double-base propellant (HEMRL, Propellant Specification 2018)

Chemical contents (percentages)		Dimensions of propellant grain	
NC (12 % N content)	59±1.5%	OD	14.1±0.2 mm (Nominal)
NG	32±0.5%	Web	5.10±0.15mm
DEP	6±0.5%	Length	6.5 mm (Nominal)
Carbamite	2±0.2%	Density	1.57 g/cc
Candela wax	1%	Shape	Tubular with single-axial perforation

NC: Nitro-cellulose; OD: Outer diameter; NG: Nitro-glycerine; DEP: Diethyl phthalate



Figure 4. Photo of the double-base propellant.

products are namely nitrogen oxides, water vapor and condensable gases. This propellant may react to provide a detonation velocity between 6-7 km/s when confined under specific circumstances. However, with proper compounding, it will undergo the deflagration phenomenon. Most of the propellant undergoes deflagration which is the main requirement for operating the harness mechanism.

6. EXPERIMENTAL PART OF THE CLOSED VESSEL (CV)

6.1. Pressure-time (P-t) profile of the gas generator

The CV is cylindrical in shape where the cartridge is loaded. This is to allow various performance parameters to be evaluated in the laboratory. The experimental firing procedure consists of the CV body, a gauge adapter, the cartridge, the firing mechanism, a copper washer and the closing plug. The firing mechanism is placed at one end and the closing plug at the opposite end. A copper washer is placed on the closing plug to avoid the combustion products from leaking after the propellant is burned. A Yokogawa scope corder and charge amplifier are used to

record pressure. A gauge adapter with pressure sensor is fitted to the vessel body. The selected pressure sensor has a small size, fast response, durability, hermetically sealed construction, sensitivity to 0.39 pC/psi , a measurement range up to 15000 psi and a rise time of $\leq 1 \mu\text{s}$. The vessel has been designed and fabricated for realizing the performance parameters (Parate et al 2019). The CV schematic is shown in Figure 5. The striker for the firing mechanism strikes the cap and indents it. This action crushes the sensitive composition between the cap and anvil in the base of the gas generator. The flash passes through the two flash holes to ignite booster and propellant. The pressure-time ($P-t$) profile produced after firing the cartridge in the CV is shown in Figure 6. The peak (i.e. maximum) pressure generated in the CV is 3.84 MPa and the corresponding time is 258.43 milliseconds. The methodology is similar for evaluating the performance parameters of the cartridge in the CV (Parate et al 2021).

6.2. Energy balance equation

As the propellant burns inside the CV, its chemical energy is converted into gas energy resulting in high pressure and high temperature of the combustion products. During the burning, two assumptions are used (Parate et al 2018).

- The system is adiabatic (no heat transfer- due to the rapid burning process) where the propellant ignition takes place and
- The exothermic reaction within the CV is due to the decomposition

According to the first assumption, the solid (propellant+booster) \rightarrow Gas+Energy

Using the first law of thermodynamics;

$$dQ=dW+dU \quad (19)$$

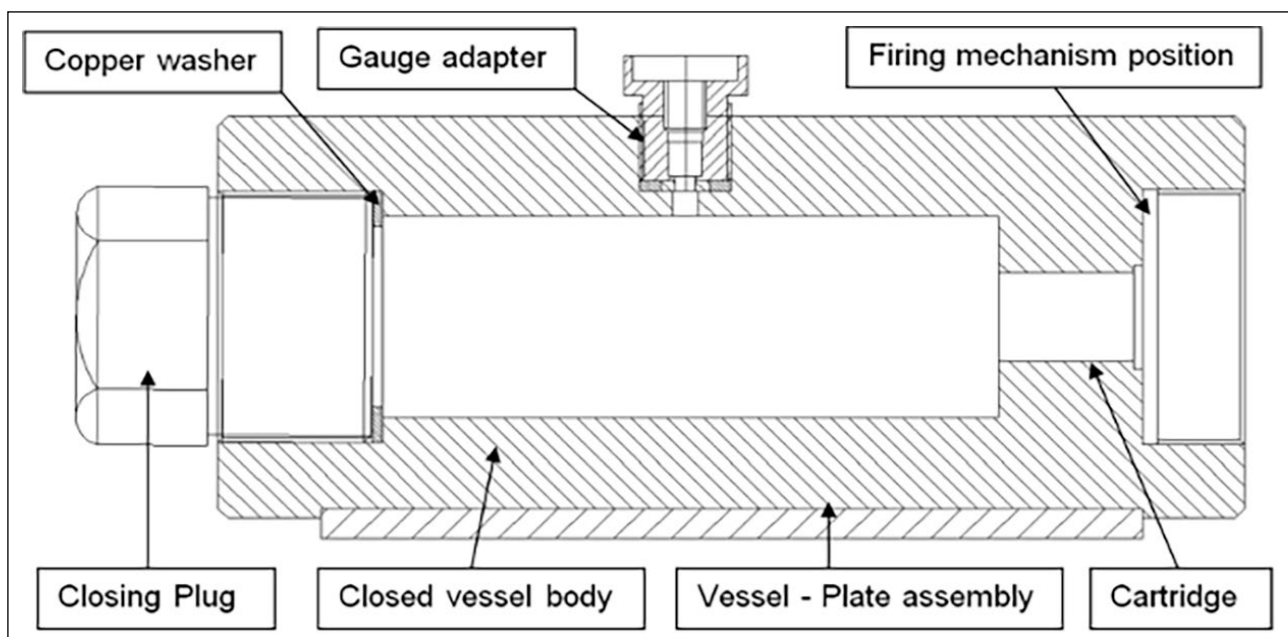


Figure 5. Engineering schematic of the CV.

CV: Closed vessel.

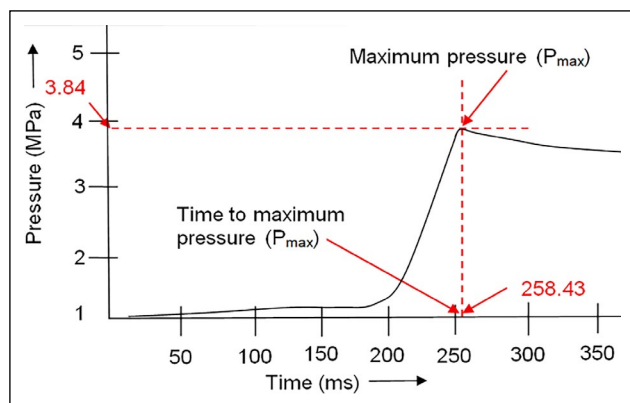


Figure 6. *P-t* profile in the CV.

CV: Closed vessel.

where dQ , dU , and dW are the heat supplied to the system, the internal energy and the work performed. As the vessel experiences no heat transfer and no deformation, $dU=0$. However, in real practice heat loss will always occur from the vessel to the surroundings. This can be observed from the *P-t* profile as shown in Figure 6. Ideally the profile should be a straight line after attaining peak pressure. However, a pressure drop occurs after reaching maximum pressure. No system exists in the universe where heat loss doesn't occur. Heat loss can be minimized for maximum utilization of work.

7. RESULTS AND DISCUSSION

The performance evaluation of the gas generator is carried out in a specially designed test vessel (i.e. CV). The gas generator develops pressures between 2.7 to 5.3 MPa and a TP_{max} 216 within 332 ms in the CV under hot (45°C) and cold (-26°C) conditions and a volume of 150 cc. The cartridges filled with 1.5 g of propellant and 0.4 g booster for the CV firing. They are then conditioned for a minimum of six hours before firing. The performance characters (i.e. P_{max} and TP_{max}) of the gas generator have been experimentally evaluated in a suitable test vessel designed and fabricated for that application (de Oliveira et al. 2005; Parate et al. 2021). This is explained in Section 5. The various thermodynamic parameters of the gas generator such as co-volume, flame temperature, force constant, calorific value, and maximum pressure have been obtained experimentally by burning the propellant inside the closed vessel within laboratory facilities are enumerated in Table 2.

The burn rate and calorimetric value of the propellant is determined using strand burner and bomb calorimeter instruments. The other parameters of flame temperature and force constant are obtained by burning the propellant in a CV at loading density of 0.2 g/cc. A differential scanning calorimeter (DSC) is used to determine the specific heat. The specific heat of the propellant gas has been determined as 0.3488 cal/g/°C depending on the propellant composition. This paper has addressed all the goals and an objective has been met in a full-scale test demonstration of a gas generator for aircraft application.

Table 2. Thermodynamic properties of the gas generator

Thermodynamic properties	Values
Mean molecular weight	23.27 g/mole
No. of moles of gas	0.04542 mole/g
Combustion heat of propellant	531.32 cal/g
Ratio of Specific heat (Gamma)	1.2448
Flame temperature	2944 K
Internal energy of product gases	830 cal/g
Specific heat	0.3488 cal/g/°C
Gas volume	962.75 cc
Co-volume	0.989 m ³ /kmol
Force constant	1052 J/g
Calorimetric value	925 cal/g
Specific heat of the propellant gas	0.3488 cal/g/°C
Maximum pressure at 0.2 loading density	260 MPa

6. CONCLUSION

The work that is present in this paper summarized the different thermodynamic aspects for evaluating the various properties of a gas generator for aircraft application. The major parameters of the gas generator are dependent on volumetric loading, pressure time profile, propellant grain configuration, and chemical contents. This paper also explains the performance characteristics of a gas generator in a CV. These data will help ballistic studies, serviceability, safety and propellant life before induction into actual use in the development phase. All calculations have generally been made with through applicability of the ideal gas law and in terms of temperature and pressure. When predicting and assessing the results, the various assumptions needed to be kept in mind. This type of a gas generator has to meet various design qualification tests during development phase before getting inducted into service. The author has brought out the essence of recently published papers of interest from open available sources.

ACKNOWLEDGEMENTS

The author is obliged to Director ARDE for his kind consent towards bringing out this work. The author also thanks Dr. R S Damse for extending the facility and providing the data on thermodynamic properties. The author is also grateful to anonymous referee for their enlightening comments.

DATA AVAILABILITY STATEMENT

The published publication includes all graphics and data collected or developed during the study.

CONFLICT OF INTEREST

The author declared no potential conflicts of interest with respect to the research, authorship, and/or publication of this article.

ETHICS

There are no ethical issues with the publication of this manuscript.

FINANCIAL DISCLOSURE

The authors declared that this study has received no financial support.

REFERENCES

- Cumming, Adam S. (2009). New trends in advanced high energy materials. *Journal of Aerospace Technology and Management*, 1(2), 161–166. [\[CrossRef\]](#)
- de Oliveira, J. L. S. P., de, Filho A. A. M. F., Platt, G. M., & Peixoto, F. C. (2005). Estimation of ballistic parameters of gun propellants through closed vessel experiment modelling. *Thermal Engineering*, 4, 50–55. [\[CrossRef\]](#)
- High Energy Material Research Laboratory. (2018). *HEMRL SPECN No. HEMRL/GP/PS/410 double base propellant specification*. High Energy Material Research Laboratory.
- Han, Z. Y., Zhang, Y. P., Du, Z. M., Li, Z. Y., Yao, Q. & Yang, Y. Z. (2017). The formula design and performance study of gas generators based on 5-aminotetrazole. *Journal of Energetic Materials*, 36(1), 61–68. [\[CrossRef\]](#)
- Martirosyan, K.S., Wang, L., Vicent, A., & Luss, D. (2009). Nanoenergetic gas generators: Design and performance. *Propellants, Explosives, Pyrotechnics*, 34, 532–538. [\[CrossRef\]](#)
- Nag, P. K. (2018). *Engineering thermodynamics*. (6th ed.). McGraw Hill.
- Parate, B. A., Chandel, S & Shekhar H. (2019). Cartridge case design and its analysis by bilinear, kinematic hardening model. *Advances in Military Technology*, 14(2), 231–244.
- Parate, B. A., Chandel, S., & Shekhar, H. (2019). Design analysis of closed vessel for power cartridge testing. *Problems of Mechatronics Armament, Aviation, Safety Engineering*, 101(35), 25–48. [\[CrossRef\]](#)
- Parate, B. A., Chandel, S., & Shekhar, H. (2018). An experimental and numerical approach-characterisation of power cartridge for water-jet application. *Defence Technology*, 14(6), 683–690. [\[CrossRef\]](#)
- Parate, B. A., Chandel, S., & Shekhar, H. (2021). Performance evaluation of power cartridge in closed vessel for water-jet application. *International Journal of Energetic Material*, 7(1), 1–12.
- Parate, B. A., Deodhar, K. D., & Dixit, V. K. (2021). Qualification testing, evaluation and test methods of gas generator for IEDs applications, *Defence Science Journal*, 71(4), 462–469. [\[CrossRef\]](#)
- Shekhar, H. (2018). *Rocketary with solid propellants*. Studium Press.



Research Article

First and second law assessment of a solar tower power plant for electrical power production and error analysis

Mohd PARVEZ^{*1}, Syed Mohammed MAHMOOD², Osama KHAN²

¹Department of Mechanical Engineering, Al-Falah University, Haryana, India

²Department of Mechanical Engineering, Jamia Millia Islamia, New Delhi, India

ARTICLE INFO

Article history

Received: March 20, 2023

Revised: May 19, 2023

Accepted: May 24, 2023

Key words:

Heliostat field, steam cycle, waste heat recovery, exergy destruction, organic Rankine cycle

ABSTRACT

The primary objective of this study is to investigate the solar-powered combined-cycles system for converting the available solar energy to its truest potential and for generating electrical power. This combined-cycles system consists of a solar power tower, steam turbine cycle, and organic Rankine cycle. The study focuses on recovering the waste heat that is obtained from the exit of a steam turbine and using it to operate the Rankine cycle with refrigerants R-113, R-11, and R-1233zd. The analysis also predicts the effects of solar irradiance for a mass flow rate of molten salt and steam, turbine inlet pressure, and turbine inlet temperature on first and second law efficiencies in the combined-cycles system. The novel concept of uncertainty analysis is also introduced in this work in order to provide precise accurate results and remove all errors, which are found to be in the desired range of 3.81%. The results also show that as the direct normal irradiation (DNI) increases from 600 W/m² to 1000 W/m², first law efficiency is obtained in the range of 32.31% to 37.99% and second law efficiency from 24.14% to 25.51% after employing the organic Rankine cycle (ORC) system. Further, the results indicate the maximum exergy destruction that occurs in the central receiver to be around 42%, in the heliostat to be 31%, in the steam generator to be 10%, and in the heat exchanger to be 3.6%.

Cite this article as: Parvez M, Mahmood SM, Khan O. First and second law assessment of a solar tower power plant for electrical power production and error analysis. *Seatific* 2023;3:1:33–42.

1. INTRODUCTION

In the modern era, communities often opt for a sustainable approach to power generation that involves a responsible procedure for utilizing energy resources at bare minimum cost while simultaneously posing lower detrimental environmental effects. The front runners for conventional fuels are fossilized coal, petro-diesel products, and compressed natural gas, which have been utilized for decades in energy generation across the globe but are acknowledged as being finite, and side effects such as global warming and climate change are associated with their applications in the power industry (Parvez, 2017; Vujanović et al., 2019; Kumar, 2020; Assad & Rosen, 2021). To meet

these challenges, an urgent need exists for developing cost-effective energy alternatives. Based on the above energy perspective, concentrating on solar thermal setups seems to be an attractive perspective and feasible enough to fulfil and simultaneously achieve cleaner economical power generation with a lower global environmental impact (Hussaini et al., 2020; Ayaz et al., 2021; Akram et al., 2023).

Over the past few years, a large number of studies have been devoted to developing various technologies to provide a viable and feasible solution for harnessing the potential of thermal radiation. One of these technologies was seen in the development of a central receiver system that primarily deploys a substantial number of heliostat field solar collectors

*Corresponding author.

*E-mail address: mparvezalig@rediffmail.com



integrated with solar receivers and placed at the zenith of a solar tower (Collado & Guallar, 2019; Ahmad et al., 2022; D'Souza et al., 2023). This integrated system employs a working fluid primarily in molten salt or Duratherm oil, thereby deploying first-of-their kind grid-connected commercial solar power plants (Zolfagharnasab et al., 2020; Caraballo et al., 2021).

In the past, multiple studies have established steam turbines as the prime component for utilizing the maximum amount of energy compared to other equipment, predominantly due to the majority of heat being carried away in the form of flue gases. Generally, these gases have comparatively higher temperatures than atmospheric conditions; as a result, heat transfer leads to substantial energy losses and further leads to lower efficiency rates (Omar et al., 2019; Corumlu & Oztur, 2021; Varis & Ozkilic, 2023).

Successful models have been developed to curb energy losses while simultaneously utilizing this waste energy. Among these models, the conventional organic Rankine cycle (ORC) system has been found to be quite effective in successfully recovering waste heat sources. ORCs provide an improved method for successfully transforming the waste heat energy accessible at the exit of the steam turbine into electrical power. This system works with an organic, high molecular mass working fluid that possesses the characteristics of having a liquid-vapor phase change (i.e., boiling point) that occurs at temperatures below the water-steam phase transformation temperature (Haq, 2021; Zheng et al., 2022; Li et al., 2023). ORCs do not consume additional energy and reduce environmental pollution factors such as CO₂ and SO₂. In recent years, many researchers have considered thermodynamic assessments in order to utilize solar energy as a major source for power production integrated with ORC to enhance the performance of the entire system (Singh & Mishra, 2019; Lourenco, 2023).

Georges et al. (2013) designed a small-scale ORC integrated with an engine solar power plant that used techniques to optimize and regulate the policies that should be employed for larger systems. Their study focused on simulated replicas of the ORC engine while simultaneously considering its basic limitation that restricts a wider range of operating temperatures and technical maturity of the components. These prospective simulations allowed the efficiency of the ORC engine to be able to shoot up to 12% when the evaporating and condensing temperatures lie respectively between 140°C and 358°C. Li (2014) investigated a simple ORC technology operated by a low-grade heat source for converting heat to power. The basic principle behind ORC is quite analogous to a simple steam Rankine cycle. The organic working fluid is pumped into the heat exchanger where it can be vaporized. Furthermore, Li equated the results with the conventional steam Rankine cycle, showing ORC to have numerous benefits. Kerme and Orfi (2015) explained a different system for enabling thermodynamic modeling for conventional ORCs primarily operated by parabolic trough solar collectors for testing eight different kinds of working fluids. They also independently investigated the most influential parameters such as turbine inlet temperature on turbine size, expansion ratio, outlet volume flow rate, irreversibility ratio, and total exergy destruction. Consequently, the results

obtained from their study showed that the maximum exergy destruction occurred in the solar collector with about 74.9% of the total exergy destroyed, and the next 18.2% of the total destroyed exergy occurring in the condenser. Loni et al. (2017) carried out an exergy analysis of an ORC that receives radiated thermal energy from the tubular cavity receiver of a solar dish collector. The analysis performed in their study was checked with several parameters such as receiver exergy rate, receiver exergy factor, thermal exergy efficiency, and electrical exergy efficiency.

Studies on exergy analysis for minimizing losses in power plants have provided valuable insights into the energy losses that occur within a system. By employing exergy analysis techniques, researchers can gain a comprehensive understanding of the thermodynamic inefficiencies present in power plant equipment. This knowledge allows one to identify the specific areas where improvements can be made in order to optimize energy conversion processes and reduce unnecessary energy dissipation. By focusing on exergy analysis, researchers can develop innovative strategies and technologies to limit losses, leading to increased operational efficiency, reduced environmental impacts, and improved economic viability for power plants. Such studies play a vital role in enhancing the overall efficiency and sustainability in the power generation sector.

Recently, a majority of researchers have investigated the heat recovery ORC cycle operated with regard to various working fluids and using solar energy as the prime source for running the system. Doe et al. (2022) focused on investigating the exergy losses in various components and exploring strategies to improve overall efficiency. They proposed modifications to the system design and operating parameters based on their exergy analysis findings to reduce losses and enhance the energy conversion process. Habibi et al. (2020) investigated a regenerative supercritical Brayton cycle with an organic Rankine cycle attached at the bottom and the cycle driven by a solar power tower applying molten salt as a working refrigerant. The results show the maximum exergy efficiency obtained to be 21.23%; a net power output of 177,321 kW should be achievable when helium is used as a refrigerant, and the highest exergy destruction is provided at 70,576 kW obtained from oxygen. Yağlı et al. (2021) presented an ORC system to improve the entire performance of a gas turbine used in wood production. A steam boiler cycle was integrated with a gas turbine alongside an ORC to produce steam to run the cycle. Their results indicate that the maximum ORC net power production, thermal efficiency, and exergy efficiency were found to respectively be 1,076.76 kW, 21.14%, and 47.00% after employing the ORC using R123 as a working fluid at 230°C and 35 bars of pressure. Chen et al. (2022) recently published a paper on a solar-based hybrid energy system for producing electrical energy, thermal energy, and hydrogen fuel. Their computed results revealed the system to be able to generate 147.8 kWh/day of electrical energy and 595 g/day of hydrogen fuel. The past available literature shows studies to have seldom been conducted on the ORC cycle integrated with the heliostat field's solar collector for power generation in terms of first and second law analyses.

Table 1. Properties of the solar-operated steam Rankine cycle-ORC configuration combined-cycles system (Ahmad et al., 2022; Akram et al., 2023)

System properties values		
Heliostat field	Beam radiation (DNI; mid value)	800 W/m ²
	Overall field efficiency	75%
	Total heliostat aperture area	10,000 m ²
Central receiver	Aperture area	12.5 m ²
	Inlet temperature of molten salt	290°C
	Outlet temperature of molten salt	565°C
	View factor	0.8
	Tube diameter	0.019 m
	Tube thickness	0.00165 m
	Emissivity	0.8
	Reflectivity	0.04
	Wind velocity	5.0 ms ⁻¹
	Passes	20
Steam generator	Internal temperature of water	240°C
	Outlet temperature of steam	550°C
	Ambient temperature	20°C
Organic Rankine cycle	Working fluid used in ORC	R-113, R-11, R-1233zd
	Mass flow rate of waste heat source	1 kg/s
	ORC turbine inlet pressure (bar)	15-35 (range)
	ORC turbine outlet pressure (bar)	0.5
	ORC turbine isentropic efficiency	80%
	ORC pump isentropic efficiency	75%
Thermo-physical properties of molten salt	Temperature range of molten salt	220°C-574°C
	Viscosity of molten salt	25 MPa-s
	Density of molten salt	863 Kg/m ³
	Thermal conductivity of molten salt	0.134 W. K ⁻¹ .m ⁻¹
	Specific heat of molten salt	10 kJ.K ⁻¹ .kg ⁻¹
	Freezing temperature of molten salt	238°C

ORC: Organic Rankine cycle; DNI: Direct normal irradiation

The current study’s primary objective is to evaluate the first and second law analyses of ORC driven with input energy from the waste heat available at the exit of the steam turbine that receives energy from a heliostat field’s solar collector. The study further includes the various numerical calculations that form the basis of the graphs plotted to understand and thus comment on the relationships among various properties. The article conducts a detailed study of first and second law analyses on ORC using the refrigerants R-113, R-11, and R-1233zd and applies a proper uncertainty analysis in order to eliminate any adherent errors so as to enhance the accuracy of this analysis. Table 1 shows the properties of the solar-operated steam Rankine cycle-ORC configuration combined-cycles system.

2. SYSTEM DESCRIPTION

The planned solar-operated system contains a steam Rankine cycle (RC) and an organic cycle Rankine (ORC) operating with the aid of solar energy to generate electricity. Figure 1 shows the outline of the entire system. With regard to the solar components, they are comprised of a set of heliostats that collect and concentrate sunlight onto the

receiver, which captures the focused sunlight and transfers the heat energy to the working fluid (molten salt). This heat transportation system is comprised of primary pipes, pumps, and valves and facilitates the heat transfer to the power conversion systems. The power transformation system is comprised of a steam generator, turbine generator, organic Rankine system and supplies different types of apparatuses that convert the thermal energy into electric power and further supplies it to the utility grid.

The molten salt enters at high temperature into a steam generator, where it transfers the thermal energy, thereby generating steam that is in turn expanded to generate electric power in a steam turbine. The waste heat of the steam obtained at the exit of the steam turbine moves into the heat exchanger, where it then transfers its remaining heat for recovery by running the ORC system, after which the saturated liquid is pumped to the steam generator of the RC cycle. Furthermore, the steam exits from the heat exchanger where the heated organic vapor enters the refrigerant turbine and produces power as it expands. Furthermore, this thermal energy is transferred into the atmosphere within the condenser, allowing lowered temperature refrigerant into the heat exchanger to complete the cycle.

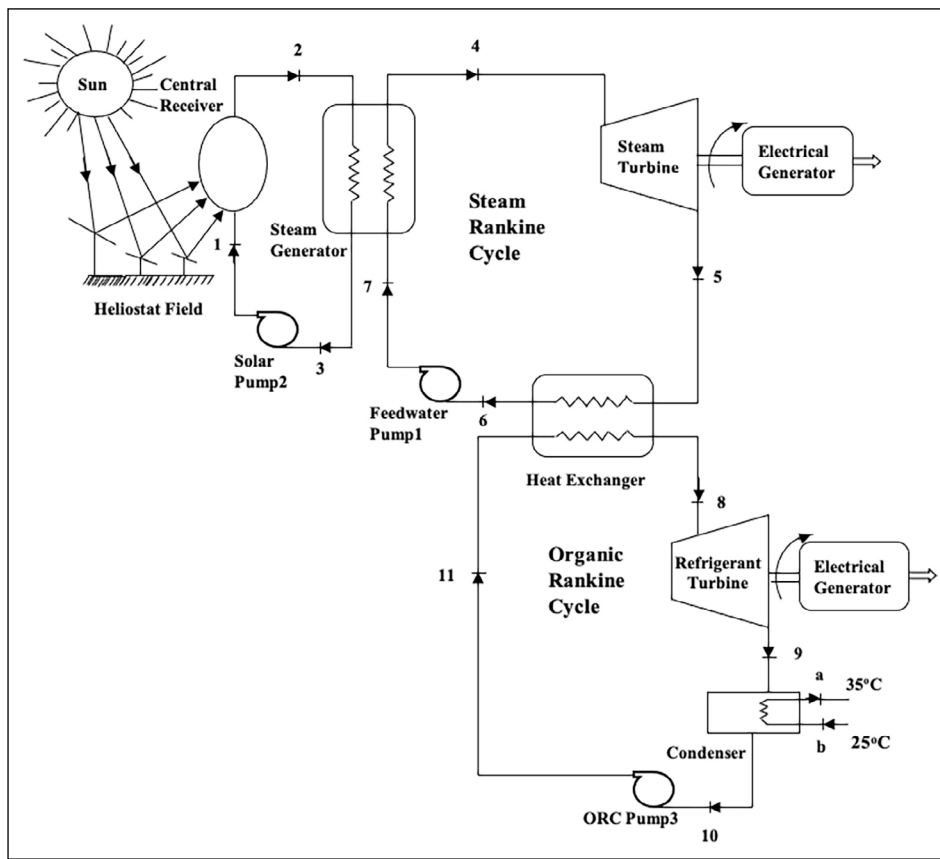


Figure 1. Solar tower power plant.

ORC: organic Rankine cycle.

3. UNCERTAINTY ANALYSIS

The primary reason for carrying out an error and uncertainty analysis in any research is that human errors are very common, and even machines may have some small errors in the calculation of a property that also needs to be taken into consideration and calibrated likewise. Table 2 displays all the equipment used for measuring various properties in the system along with its errors.

The total percentage of uncertainty (TPU) has been determined in this experiment by applying the equation (Holman, 2012) provided below:

$$TPU = [(U_1)^2 + (U_2)^2 + (U_3)^2 + (U_4)^2 + (U_5)^2 + (U_6)^2]^{0.5} \quad (1)$$

As a result, the total uncertainty associated with the system comes close to 3.81% for which the analysis of a complete setup is suitable, satisfactory, and in line with previous research (Holman, 2012; Seraj, 2022).

4. THERMODYNAMIC MODELING FOR A COMBINED-CYCLES SYSTEM FOR ELECTRICAL POWER PRODUCTION

This study mainly focuses on the primary model of a cascade system that is based on the integration of two varying models with one another. Analysis of the first and second laws has been carried out for mass, energy, and exergy balances, which will enable pinpointing the exact location

within the model where components may have maximum thermodynamic inefficiencies. The study has formulated some basic assumptions and explained them as follows:

- The complete model is an integration of different components aligned together to work as a single model and is further presumed to work at a steady-state condition with constant solar insulation.
- During the entire analysis, the ambient conditions in which the model operated assume standard and constant values of temperature T_0 and pressure p_0 at 20.3°C and 1.01325 bar.
- Subsequent pressure drops and thermal losses in the atmosphere have not been taken into consideration for the majority of the model's apparatuses.
- Sudden variations or alterations in the potential and kinetic-based energies have not been considered within the study's formulations.
- The chemical exergy associated with the materials has not been taken into consideration.

4.1. Heliostat (H)

The heliostat field is an integration of several stacked-up heliostats that represent and focus the majority of the sun's rays onto the centralized dedicated receiver. The rate at which a major portion of solar thermal input is being received may be written as:

Table 2. Measurement accuracies and experimental uncertainties associated with sensors and parameters

Sensor no	Sensors and parameters	Designated symbol	Accuracies and uncertainties measurement
1	T-type thermocouples	U_1	± 0.3 C
2	Flow meter	U_2	± 4 ml
3	Pressure transducer	U_3	± 1.9 m bar
4	Voltage measurement	U_4	± 0.08 V
5	Current measurement	U_5	± 0.1 A
6	Power temperature coefficient	U_6	$-0.3\%/C$

$$\dot{Q}_{solar} = A_{field} q \quad (2)$$

where q is the amount of solar radiation received per unit area and A_{field} is the calculated area of the heliostat field. This is linked to the field of opening (A_{app}) in terms of the concentration ratio and is written as follows:

$$C = \frac{A_{field}}{A_{app}} \quad (3)$$

The central receiver receives half of the thermal energy obtained from the heliostat, with the remainder being lost to the atmosphere and expressed as:

$$\dot{Q}_{solar} = \dot{Q}_{CR} + \dot{Q}_{lost, heliostat} \quad (4)$$

The heliostat's energy efficiency is written as:

$$\eta_{energy, heliostat} = \frac{\dot{Q}_{CR}}{\dot{Q}_{solar}} \quad (5)$$

The thermal energy from the central recipient that is consequently drained into the atmosphere by the molten salt with the remainder being lost is expressed as follows:

$$\dot{Q}_{CR} = \dot{Q}_{moltensalt} + \dot{Q}_{lost, CR} = \dot{m}_{moltensalt} (h_2 - h_1) + \dot{Q}_{lost, CR} \quad (6)$$

$$\eta_{energy, CR} = \frac{\dot{m}_{moltensalt}}{\dot{Q}_{CR}} \quad (7)$$

The exergy destruction in the central receiver is written as:

$$\Delta \dot{E}_{CR} = \dot{m}_{moltensalt} [(h_2 - h_1) - T_0 (s_2 - s_1)] \quad (8)$$

4.2. Steam generator (SG)

Using the energy balance approach to a steam generator results in:

$$\dot{m}_{moltensalt} (h_2 - h_3) = \dot{m}_{st} (h_4 - h_5) \quad (9)$$

The exergy destruction in the heat steam generator is expressed as:

$$\Delta \dot{E}_{SG} = T_0 [\dot{m}_{moltensalt} (s_2 - s_3) + \dot{m}_{st} (s_4 - s_7)] \quad (10)$$

4.3. Steam turbine (ST)

Applying the first law of thermodynamics to the steam turbine results in:

$$\dot{W}_T = \dot{m}_{st} (h_4 - h_5) \quad (11)$$

The exergy destruction in the steam turbine is expressed as:

$$\Delta \dot{E}_{st} = \dot{m}_{st} [(h_4 - h_5) - T_0 (s_4 - s_5)] - \dot{W}_T \quad (12)$$

4.4. Heat exchanger (HE)

The energy balance regarding the heat exchanger is expressed as:

$$\dot{m}_{st} (h_5 - h_6) = \dot{m}_{ref} (h_8 - h_{11}) \quad (13)$$

The exergy destruction in the heat exchanger is written as:

$$\Delta \dot{E}_{HE} = T_0 [\dot{m}_{st} (s_5 - s_6) + \dot{m}_{ref} (s_8 - s_{11})] \quad (14)$$

4.5. Feedwater pump1 (FWP1)

The energy balance regarding the feedwater pump1 is expressed as:

$$\dot{W}_{FWP1, wt} = \dot{m}_{wt} (h_7 - h_6) \quad (15)$$

The exergy destruction in the feedwater pump is written as:

$$\Delta \dot{E}_{FWP1} = T_0 [\dot{m}_{wt} (s_7 - s_6)] \quad (16)$$

4.6. Solar pump2 (SP₂)

The energy balance regarding the solar pump is expressed as:

$$\dot{W}_{SP2} = \dot{m}_{solarfluid} (h_3 - h_1) \quad (17)$$

The exergy destruction in the solar pump is written as:

$$\Delta \dot{E}_{SP2} = T_0 [\dot{m}_{solarfluid} (s_3 - s_1)] \quad (18)$$

4.7. Refrigerant turbine (RT)

The energy balance regarding the refrigerant turbine is expressed as:

$$\dot{W}_{T, RT} = \dot{m}_{vapour} (h_8 - h_9) \quad (19)$$

The exergy destruction in the refrigerant turbine is written as:

$$\Delta \dot{E}_{RT} = \dot{m}_{RT} [(h_8 - h_9) - T_0 (s_8 - s_9)] - \dot{W}_{T, RT} \quad (20)$$

4.8. Condenser (C)

The energy balance regarding the condenser is expressed as:

$$\dot{m}_{vapour} (h_9 - h_{10}) = \dot{m}_{water} (h_a - h_b) \quad (21)$$

The exergy destruction in the condenser is written as:

$$\Delta \dot{E}_C = T_0 [\dot{m}_{vapour} (s_9 - s_{10}) + \dot{m}_{water} (s_a - s_b)] \quad (22)$$

4.9. ORC pump3 (ORC P3)

The ORC pump's energy balance is expressed as follows:

$$\dot{W}_{ORC, P3} = \dot{m}_{ref} (h_{11} - h_{10}) \quad (23)$$

The depletion of exergy in the solar pump is calculated as follows:

$$\Delta \dot{E}_{ORC, P3} = T_0 [\dot{m}_{ref} (s_{10} - s_{11})] \quad (24)$$

4.10. First law efficiencies

First law efficiencies is the ratio of useful energy produced in the entire system to the input energy of the fuel supplied to the entire system, can be written as:

$$\eta_I = \frac{\dot{W}_{ST} + \dot{W}_{RT} - \dot{W}_{SP1} - \dot{W}_{SP2} - \dot{W}_{ORC, P3} - \dot{W}_{C, ORC}}{\dot{Q}_{C, R}} \quad (25)$$

4.11. Second law efficiencies

The product exergy output is known as the exergy input separated into the whole system and calculated as:

$$\eta_{II} = \frac{\dot{W}_{ST} + \dot{W}_{RT} - \dot{W}_{SP1} - \dot{W}_{SP2} - \dot{W}_{ORC, P3} - \dot{W}_{C, ORC}}{\dot{E}_{x, in}} \quad (26)$$

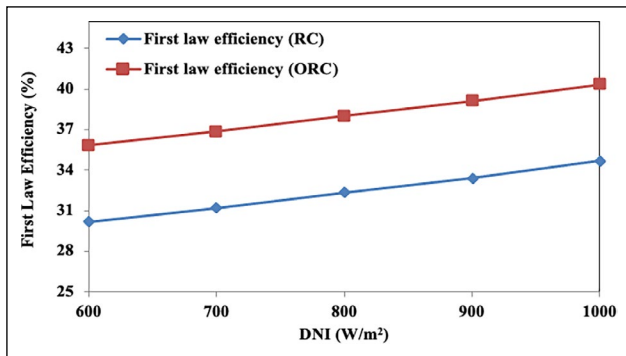


Figure 2. Variations in first law efficiencies with changes in DNI of an RC and ORC solar tower power plant.

DNI: Direct normal irradiation; RC: Rankine cycle; ORC: Organic Rankine cycle.

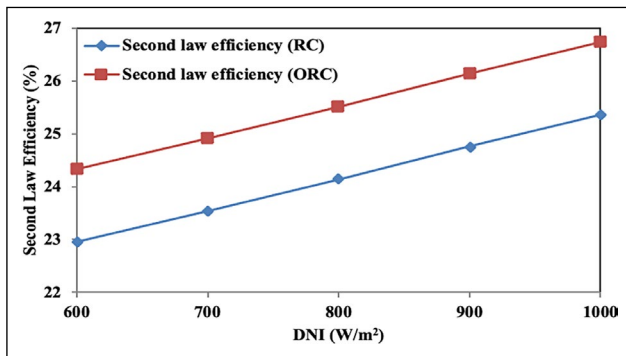


Figure 3. Variation of second law efficiency with the change in DNI of an RC and ORC solar tower power plant.

5. DEFINING RESULTS AND DISCUSSIONS

This section explains the basic framework and evaluates the estimations after employing thermodynamic modeling for the first and second law analyses. Furthermore, this section computes a combined assessment of the effects on the several important parameters that furnish a major effect on the results of solar-powered combined cycles. To complete this study, influential parameters have been analyzed such as the effect of solar irradiance on first and second law efficiencies, the mass flow rate of molten salt and steam, turbine inlet pressure, turbine efficiencies at the inlet, and exergy degradation regarding the first and second laws regarding all major modules within the combined-cycles system. The study has also examined the thermodynamic properties of refrigerants R-113, R-11, and R-1233zd as procured in the ORC cycle, and the results are well-matched under similar conditions (Parvez & Khalid, 2018; Shah et al., 2020).

The effects of first and second law efficiencies alongside changes in the direct normal irradiation (DNI) on a steam Rankine cycle and organic Rankine cycle of a combined-cycles system are summarized in Figures 2 and 3. The efficiency of an entire system is increased by increasing the DNI values from 600 W/m² to 1,000 W/m². This observation results from an extreme sensitivity while considering the dissimilarity of DNI captured from the

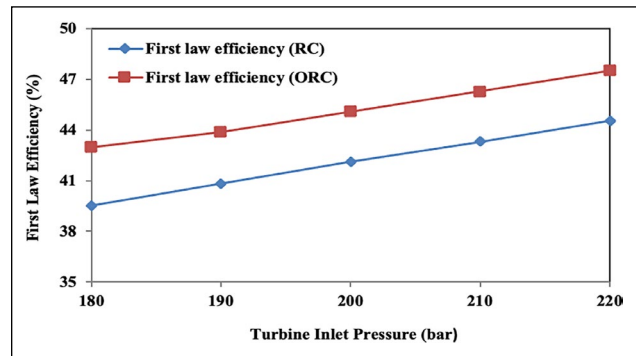


Figure 4. Variations in first law efficiencies with changes in the turbine inlet pressure of the solar tower power plant.

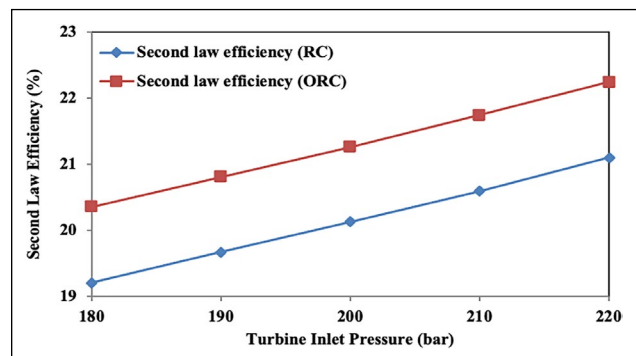


Figure 5. Variations in second law efficiencies with changes in the turbine inlet pressure of the solar tower power plant.

surface temperature of the central receiver. Furthermore, the same increasing trend was noted regarding the first and second law efficiencies of the entire system. The entire cycle efficiency of the second law analysis is also lower than the first law efficiencies as observed for the combined-cycles system. This is due to a major quantity of exergy associated with the thermal energy that has been received being less than its energy content, therefore resulting in lower improvements regarding second law efficiencies for the combined-cycles system for subsequent increases in DNI.

The effect of steam turbine entrance pressure (TIP) on the entire first and then second law efficiencies can be observed in Figures 4 and 5. The computed results indicate that both first and second law efficiencies of the system boosted as TIP increased. The justification for this trend is that an increase in TIP causes an increase in the power outputs in the ORC turbine cycle and in the steam turbine cycle; as a result, the entire first law efficiencies of the model increase. Moreover, the proportion of increment regarding the refrigeration yield of ORC is significantly higher, which ultimately increases the overall power output generated through the steam turbine cycle. However, the behavior of the second law efficiencies increases slightly less when compared with first law efficiencies at the same pressure of the entire system. The primary reason can be stipulated as the exergy related to the heating system being lower than the energy generated through process heat.

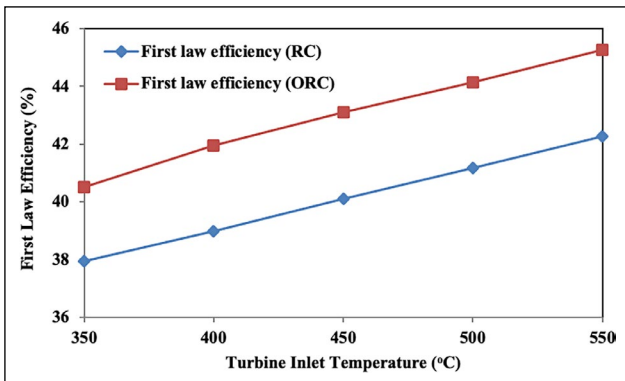


Figure 6. Variations in first law efficiencies with changes in turbine inlet temperature of the solar tower power plant.

RC: Rankine cycle; ORC: Organic Rankine cycle.

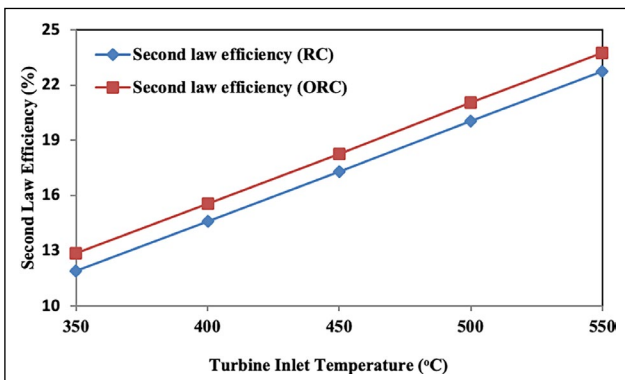


Figure 7. Variations in second law efficiencies with changes in the turbine inlet temperature of the solar tower power plant.

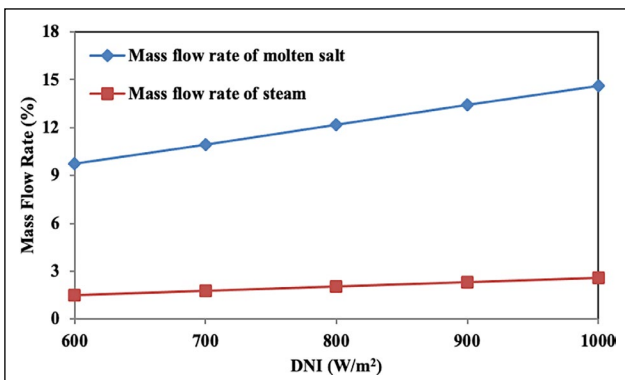


Figure 8. Variations in the mass flow rate of molten salt and steam with changes in DNI for the solar tower power plant.

DNI: Direct normal irradiation.

Figures 6 and 7 display the variations in the first and second law efficiencies of the entire system performance while varying turbine inlet temperature (TIT) for production power. Both first and second law efficiencies of the entire system can be noted to increase appreciably with an increase in TIT of the entire combined-cycles system. This increase was noted as an increase in refrigeration output of ORC and power output from the steam turbine cycle. The findings from the results justify the benefits of integrating ORC with RC, as these show a significant

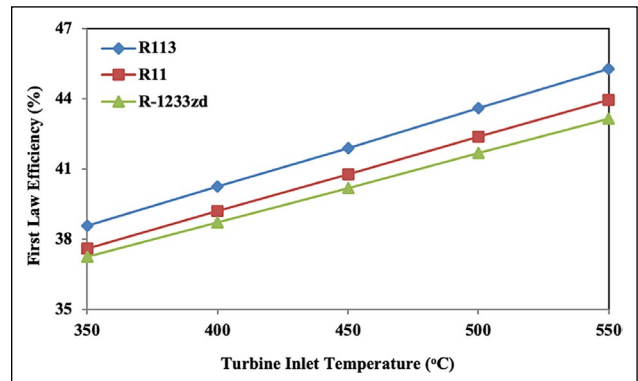


Figure 9. Variations in first law efficiencies for the cycle with changes in turbine inlet temperature at $r_p=25$ bar regarding the different refrigerants for a solar tower power plant.

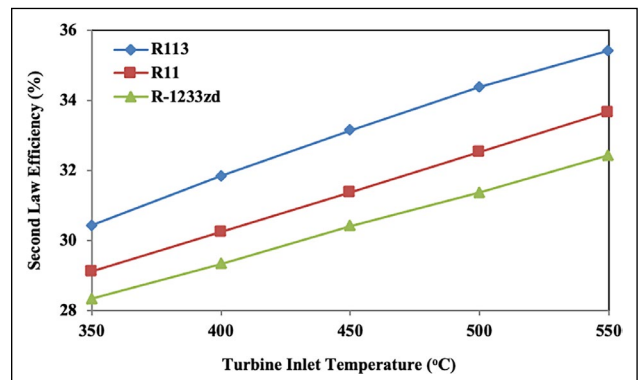


Figure 10. Variations in second law efficiencies of a cycle with changes in turbine inlet temperature at $r_p=25$ bar regarding the different refrigerants of a solar tower power plant.

increment in both first and second law efficiencies of the combined-cycles system, as well as TIT as being an important parameter in the design of a solar-operated organic Rankine cycle system.

The performance regarding the effect from changing the mass flow rate of molten salt and steam generated in the steam generator at different values of DNI is investigated in Figure 8. A model was developed that estimated a rapid gain regarding the mass flow rate of the molten salt, while a simultaneous increase in the mass flow rate of steam was registered when the DNI values increase from 600 W/m² to 1,000 W/m². The reason for the increasing trend of mass flow rate is that increased DNI results in the mass flow rate of molten salt furnishing a high rate of thermal energy to the steam generator. However, the mass flow rate of steam has smaller results compared to the mass flow rate of molten salt in the combined-cycles system.

Figures 9 and 10 display other essential variations detected for the refrigerants R-113, R-11, and R-1233zd in the thermodynamic performance of ORC regarding first and second law efficiencies as TIT increases. As these figures show, the trend is to have higher first and second law efficiencies for all working fluids as TIT increases from 350°C to 550°C. The reason behind this subsequent increase in both first and second law efficiencies is

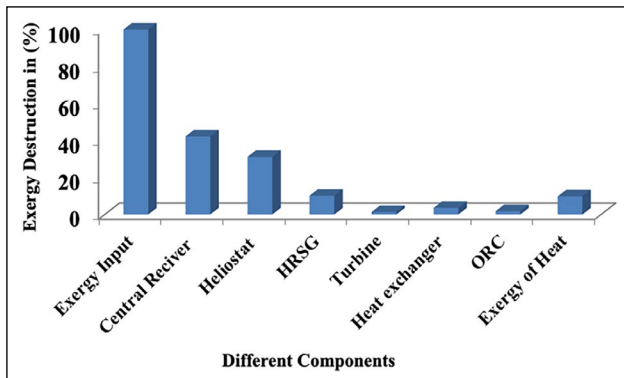


Figure 11. Exergy destruction in each component in the solar tower power plant.

HRSG: Heat recovery steam generator; ORC: Organic Rankine cycle.

primarily due to surplus electric power generation, which is attributed to the bare minimum expansion of the working fluid in the ORC turbine. Conversely, the power produced in the steam turbine is higher than for the above case. Furthermore, a notable increase in the efficiency of R-113 is observed when employed as a heat transfer fluid (refrigerant) in ORC. Concurrently, the fluid appears to possess superior efficiency compared to the R-11 and R-1233zd refrigerants regarding ORC. When comparing the results, R-113 should be noted to have a higher boiling point than both R-11 and R-1233zd, and these results have also been validated by Shah et al. (2020) and Haq (2021).

This section discusses the distribution of exergy destruction for all major components in the system and exergy input to the cycle under consideration (Fig. 11). The central receiver and heliostat have been calculated as having the largest exergy destruction due to the larger temperature differences in the system (42% and 31%, respectively). A substantial quantity of exergy destruction was also noted in the steam generator (around 10%). Among the other components incorporated in the model, an estimated combined exergy destruction of 3% was achieved out of the 100% solar exergy input and has been examined on an individual basis. This exergy destruction analysis provides useful data and also aids designers in generating an order of importance among the components developed for the proposed solar-operated organic Rankine cycle. The results here have also been validated by Ahmad et al. (2022).

6. CONCLUSION

The first and second laws of thermodynamics play a crucial role in analyzing and understanding the performance of power plants and in determining the strategies for limiting losses. Exergy analyses are based on these laws and provide insights into the quality and quantity of energy in a system, thus allowing engineers to identify and minimize losses effectively. The present analysis has established the functional conditions for a

solar-operated steam turbine to recover the waste heat when an organic Rankine cycle (ORC) is integrated at the bottom of a steam Rankine cycle (RC). Keeping the thermodynamics point of view, integrating an RC and an ORC while considering the heat rejected from the steam cycle as waste heat provides much better efficiencies as a result of utilizing the waste heat at the exit for additional power generation. In addition, the current study has introduced a novel concept of uncertainty for obtaining more accurate results with a precision that should remove all human and machine errors. Concluding remarks have been coined from the research as follows:

- A slight gain in first and second law efficiencies was observed after considerably increasing the DNI values under different operating conditions.
- First law efficiencies under the mean operating conditions of DNI occur in the range of 32.31% to 37.99%, and second law efficiencies occur in the range of 24.14% to 25.51% when employing ORC to produce power.
- First law efficiencies are notably increased with increases in turbine inlet pressure, whereas second law efficiencies of a combined-cycles system increase slightly under the same operating conditions.
- First and second law efficiencies are noted to increase slightly as the turbine inlet temperature increases in a combined-cycles system.
- A significant increase in the mass flow rate of molten salt and the mass flow rate of steam was observed as the DNI increased to different values.
- For mean operating conditions, refrigerants used in the ORC cycle show R-113 to rank as the best refrigerant, followed by R-11 in second and R-1233zd in third.
- Of the cycle's 100% exergy input, the greatest exergy destruction was found to be about 42% in the central receiver, 31% in the heliostat, 10% in the steam generator, 3.57% in the heat exchanger, and 1.81% in the ORC.
- Error analysis was applied to remove any uncertainty in the study. The error rate came out to be 3.81%, which is within the desired range.

DATA AVAILABILITY STATEMENT

The published publication includes all graphics and data collected or developed during the study.

CONFLICT OF INTEREST

The author declared no potential conflicts of interest with respect to the research, authorship, and/or publication of this article.

ETHICS

There are no ethical issues with the publication of this manuscript.

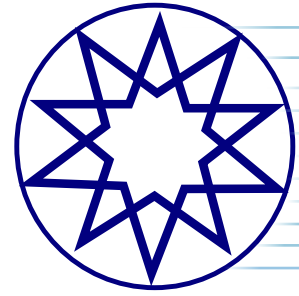
FINANCIAL DISCLOSURE

The authors declared that this study has received no financial support.

REFERENCES

- Ahmad, S., Parvez, M., Khan, T. A., Siddiqui, S. A., & Khan, O. (2022). Performance comparison of solar powered cogeneration and trigeneration systems via energy and exergy analyses. *International Journal of Exergy*, 39(4), 395–409. [\[CrossRef\]](#)
- Akram, W., Parvez, M., & Khan, O. (2023). Parametric analysis of solar-assisted trigeneration system based on energy and exergy analyses. *Journal of Thermal Engineering*, 9(3), 764–775. [\[CrossRef\]](#)
- Assad, M., & Rosen, M. (2021). *Design and performance optimization of renewable energy systems* (1st ed.). Academic Press Elsevier. [\[CrossRef\]](#)
- Caraballo, A., Galán-Casado, S., Caballero, A., & Serena, S. (2021). Molten salts for sensible thermal energy storage: a review and an energy performance analysis. *Energies*, 14, Article 1197. [\[CrossRef\]](#)
- Chen, L., Huang, H., Tang, P., Yao, D., Yang, H., & Roohbakhsh, H. (2022). A combined energy system for generating electrical and thermal energies using concentrating solar system, fuel cell and organic Rankine cycle; energy and exergy assessment. *Energy Sources, Part A: Recovery, Utilization, and Environmental Effects*, Article 2043957. [\[CrossRef\]](#)
- Collado, F. J., & Guallar, J. (2019). Quick design of regular heliostat fields for commercial solar tower power plants. *Energy*, 178, 115–125. [\[CrossRef\]](#)
- D'Souza, D., Montes, M. J., Romero, M., & Gonzalez-Aguilar, J. (2023). Energy and exergy analysis of microchannel central solar receivers for pressurised fluids. *Applied Thermal Engineering*, 219, Article 119638. [\[CrossRef\]](#)
- Georges, E., Declaye, S., Dumont, O., Quoilin, S., & Lemort, V. (2013). Design of a small-scale organic Rankine cycle engine used in a solar power plant. *International Journal of Low-Carbon Technologies*, 8(1), i34–i41. [\[CrossRef\]](#)
- Habibi, H., Zoghi, M., Chitsaz, A., Javaherdeh, K., Ayazpour, M., & Bellos, E. (2020). Working fluid selection for regenerative supercritical Brayton cycle combined with bottoming ORC driven by molten salt solar power tower using energy-exergy analysis. *Sustainable Energy Technologies and Assessments*, 39, Article 100699. [\[CrossRef\]](#)
- Haq, M. Z. (2021) Optimization of organic Rankine cycle (ORC) based waste heat recovery (WHR) system using a novel target-temperature-line approach. *Journal of Energy Resources Technology*, 143(9), Article 092101. [\[CrossRef\]](#)
- Holman, J. P. (2012). *Experimental methods for engineers* (8th ed.). Tata McGraw Hill, Series in Mechanical Engineering.
- Hussaini, Z. A., King, P., & Sansom, C. (2020). Numerical simulation and design of multi-tower concentrated solar power fields. *Sustainability*, 12(6), Article 2402. [\[CrossRef\]](#)
- Kerme, E., & Orfi, J. (2015). Exergy-based thermodynamic analysis of solar driven organic Rankine cycle. *Journal of Thermal Engineering*, 1(5), 192–202. [\[CrossRef\]](#)
- Khan, O., Yadav, A. K., Khan, M. E., & Parvez, M. (2021). Characterization of bioethanol obtained from *Eichhornia Crassipes* plant: Its emission and performance analysis on CI engine. *Energy Sources, Part A: Recovery, Utilization, and Environmental*, 43(14), 1793–1803. [\[CrossRef\]](#)
- Kumar, M. (2020). Social, economic, and environmental impacts of renewable energy resources. *Wind Solar Hybrid Renewable Energy System*. Intech Open. [\[CrossRef\]](#)
- Li, J. (2014). Gradual progress in the organic Rankine cycle and solar thermal power generation. In *Structural optimization and experimental investigation of the organic Rankine cycle for solar thermal power generation*. Springer Theses. [\[CrossRef\]](#)
- Li, Y., Teng, S., & Xi, H. (2023). 3E analyses of a cogeneration system based on compressed air energy storage system, solar collector and organic Rankine cycle. *Case Studies in Thermal Engineering*, 42, Article 102753. [\[CrossRef\]](#)
- Loni, R., Kasaeian, A., Mahian, O., Sahin, A. Z., & Wongwises, S. (2017). Exergy analysis of a solar organic Rankine cycle with square prismatic cavity receiver. *International Journal of Exergy*, 22(2), 103–124. [\[CrossRef\]](#)
- Lourenco, A. B. (2023). Application of the H&S model for the advanced exergy analysis of an organic Rankine cycle. *Revista Ifes Ciência*, 9(1), 1–12. [\[CrossRef\]](#)
- Omar, A., Saghafifar, M., Mohammadi, K., Alashkar, A., & Gadalla, M. (2019). A review of unconventional bottoming cycles for waste heat recovery: Part II – Applications. *Energy Conversion and Management*, 180, 559–583. [\[CrossRef\]](#)
- Parvez, M. (2017). *Steam boiler*. Research Gate.
- Parvez, M., & Khalid, F. (2018). Thermodynamic investigation on sawdust and rice husk biomass integrated gasification for combined power and ejector cooling cycle. *Current Alternative Energy*, 2(1), 19–26. [\[CrossRef\]](#)
- Shah, Z. A., Zheng, Q., Mehdi, G., Malik, A., Ahmad, N., Chanido, M. B., & Waqas, M. (2020). Energy and exergy analysis of regenerative organic Rankine cycle with different organic working fluids. *2020 3rd International Conference on Computing, Mathematics and Engineering Technologies (iCoMET)*. [\[CrossRef\]](#)
- Singh, H., & Mishra, R. S. (2019). Solar thermal collector integrated organic Rankine cycle technology. *Journal of Basic and Applied Engineering Research*, 6(1), 45–48.
- Varis, C., & Ozcir Ozkic, S. (2023). In a biogas power plant from waste heat power generation system using Organic Rankine Cycle and multi-criteria optimization. *Case Studies in Thermal Engineering*, 44, Article 102729. [\[CrossRef\]](#)

- Vujanović, M., Wang, Q., Mohsen, M., Duić, N., & Yan, J. (2019). Sustainable energy technologies and environmental impacts of energy systems. *Applied Energy*, 256, 113919.
- Yaglı, H., Koç, Y., & Kalay, H. (2021). Optimisation and exergy analysis of an organic Rankine cycle (ORC) used as a bottoming cycle in a cogeneration system producing steam and power. *Sustainable Energy Technologies and Assessments*, 44, Article 100985. [\[CrossRef\]](#)
- Zolfagharnasab, M. H., Aghanajafi, C., Kavian, S., Heydarian, N., & Ahmadi, M. H. (2020) Novel analysis of second law and irreversibility for a solar power plant using heliostat field and molten salt. *Energy Science & Engineering*, 8(11), 4136–4153. [\[CrossRef\]](#)



Research Articles

The taper ratio influence on the performance of 3-D cavitating hydrofoils moving under a free surface.....	1
Şakir Bal	
Optimizing the power of a variable-temperature heat reservoir Brayton cycle for a nuclear power plant in space	9
Tan Wang, Lingen Chen, Yanlin Ge, Shuangshuang Shi, Huijun Feng	
Low-computational adaptive MPC algorithmization strategy for overshoots and undershoots in instantaneous water heater stability	19
Ismael Ehtiwesh	
Thermodynamic aspects of gas generator for application in military aircraft: Some considerations.....	25
Bhupesh A Parate	
First and second law assessment of a solar tower power plant for electrical power production and error analysis	33
Mohd Parvez, Syed Mohammed Mahmood, Osama Khan	